MICROSTRUCTURAL STABILITY OF MAGNESIUM ALLOYS DURING HIGH TEMPERATURE DEFORMATION

MICROSTRUCTURAL STABILITY OF MAGNESIUM ALLOYS DURING HIGH TEMPERATURE DEFORMATION

By Zhan Gao, B.Eng.

A Thesis

Submitted to the School of Graduate Studies

in Partial Fulfilment of the Requirements

for the Degree

Master of Applied Science

McMaster University

MASTER OF APPLIED SCIENCE (2009) McMaster University
Materials Science and Engineering Hamilton, Ontario, Canada

TITLE: Microstructural Stability of Magnesium Alloys during High Temperature Deformation

AUTHOR: Zhan Gao, B.Eng.

SUPERVISOR: Dr. David S. Wilkinson

NUMBER OF PAGES: i-x, 1-96

Abstract

Superplastic forming (SPF) represents one feasible method to improve the formability of wrought magnesium alloy sheets at high temperatures. A fine grain structure not only improves the ductility but also increases the optimum strain rate thus, reducing the cost of SPF. Microstructural stability of AZ31 sheets have been characterized following different heat treatments. Second phase particles help to suppress grain growth due to the pinning effect. Thus once the temperature exceeds 450°C particles dissolve leading to abnormal grain growth. Superplastic behavior based on the fine grain structure of AZ31 was therefore evaluated at temperatures ranging from 200°C to 400°C with constant strain rates of 2.7×10^{-4} s^{-1} to 8.8×10^{-3} s^{-1}. The dominant deformation mechanism is grain boundary sliding, accommodated by dislocation creep. Under the current test conditions the initial (12μm grain size) structure is unstable and leads to dynamic recrystallization (DRX). Competition between DRX and grain growth leads to a variation of mechanical response with test conditions. Further grain refinement of AZ31 sheets was investigated through warm rolling tests for both symmetric and asymmetric types at 200°C and 300°C, followed by 200°C annealing. Asymmetric rolling was more effective for grain refinement and achieved better mechanical properties than symmetric rolling.

Acknowledgements

First, I would like to thank my supervisor, Dr. Wilkinson, for his instruction and assistance with my project. I would also like to thank Dr. Sinclair from Materials Engineering Department for his support on warm rolling testing in University of British Columbia. Discussions with Dr. Jidong Kang were also very helpful. I appreciated GM for providing the materials used in this study. The assistance of the following people at McMaster University is appreciated:

- Dr. Bruhis and R. Lemmon for DIC and mechanical testing expertise
- Dr. Petric and Dr. Zeng for FactSage software help
- Dr. Gong, Dr. Britten and Dr. Hu for XRD testing and analysis
- D. Culley and C. Butcher for metallography
- J. Garret and C. Barry for heat treatment
- Dr. Koprich for SEM help
- J. Rodda for chemical analysis

Discussions with Dr. Hu and Dr. Wang and Kendal Dunnett in my preliminary stage of research were also very useful.

The assistance of the following people at UBC is also appreciated:

- Dr. Zou for metallography
- R. Roumina, J. Jain and G. Lefebvre for rolling mill equipment
- S. Gerami, S. Shahandeh, D. Marechal and H. Hazizi for safety issue

Finally, the support and blessing from my family and friends in the past two years were very much appreciated.

Table of Contents

Abstract iii

Acknowledgements iv

Table of Contents v

List of Figures vii

List of Tables x

1. Introduction 1

2. Literature Review 2

2.1 Automotive Magnesium Alloys 2

2.2 Crystal Structure of Magnesium 3

2.3 Slip Systems in Magnesium 4

2.4 Twinning in Magnesium 6

2.5 Superplasticity of Magnesium 6

2.5.1 Superplastic Forming (SPF) 7

2.5.2 Fine-Structure Superplasticity (FSS) 8

2.6 Creep Deformation Mechanisms 10

2.6.1 Grain Boundary Sliding (GBS) 10

2.6.2 Dislocation creep 13

2.6.3 Diffusional creep 14

2.6.4 Effect of grain size 14

2.7 Microstructure stability 17

2.7.1 Recovery 17

2.7.2 Recrystallization 18

2.7.3 Grain growth 23

2.8 Thermomechanical processing 24

3. Research Objectives 29

4. Experimental Procedures 30

4.1 Introduction 30

4.2 Materials 31

4.3 Heat treatment 31

4.4 Tensile Testing 32

4.5 Digital Image Correlation 34
4.6 True stress-strain curve calculation 36
4.7 Strain-rate-sensitivity m measurements 37
4.8 Texture analysis 38
4.9 Warm Rolling 40
4.10 Microstructure Characterization 41

5. Experimental Results 43

5.1 Heat treatment of AZ31 43
5.1.1 Grain growth 43
5.1.2 Second phase particles 44
5.1.3 X-ray phase analysis 46
5.2 Tensile testing of AZ31 48
5.2.1 Elongation-to-failure 48
5.2.2 Strain-rate sensitivity 49
5.2.3 True stress-strain curve 52
5.2.4 Fracture surface observation 54
5.2.5 DRX and grain growth mechanism 58
5.3 Warm rolling testing of AZ31 61
5.3.1 Optical Microstructure 62
5.3.2 Texture analysis 65
5.3.3 Mechanical testing 68

6. Discussion 71

6.1 Microstructure characterization of AZ31 71
6.2 Superplastic behavior characterization of AZ31 74
6.2.1 Superplasticity 74
6.2.2 Deformation mechanism 75
6.2.3 Dynamic recrystallization mechanism 76
6.3 Grain refinement by warm rolling of AZ31 80
6.3.1 Shear Strain measurement in asymmetric rolling 80
6.3.2 Microstructure evolution 81
6.3.3 Mechanical properties characterization 84

7. Summary and Conclusions 86

Bibliography 87

List of Figures

Figure 2.1 Comparison of specific strength and rigidity [3]. 3

Figure 2.2. Planes and directions in h.c.p metals [8]. 4

Figure 2.3 CRSS for basal and non-basal slip at room and elevated temperatures [27]. 4

Figure 2.4 The variation in flow stress and elongation-to-failure as a function of strain rate in AZ31 (d=130μm) [22]. 8

Figure 2.5 The variation in strain rate as a function of the reciprocal grain size at 473K in ZK61 alloys [20]. 9

Figure 2.6 A model based on a GBS process accommodated by slip [46]. 11

Figure 2.7 Contribution of GBS to overall strain ξ at different strain range [19]. 12

Figure 2.8 Experimental data for coarse-grained magnesium alloys of solute diffusion compensated strain rate as a function of threshold stress and shear modulus compensated stress [22]. 15

Figure 2.9 Subgrain structure and serrated grain boundary of AZ31 strained to 40% at 250°C with the constant strain rate of 1×10^{-4} s^{-1} [18]. 17

Figure 2.10 Fine dislocation cell structures within coarser grain and dislocation array of AZ31 strained to 40% at 250°C with the constant strain rate of 1×10^{-4} s^{-1} [18]. 18

Figure 2.11 TEM structure of undeformed AZ31 and the diffraction patterns of the corres- ponding grains [18]. 20

Figure 2.12 TEM structure of DRX specimen and the diffraction pattern of the neighboring subgrains of AZ31 strained to 60% at 250°C with the constant strain rate of 1×10^{-4} s^{-1} [18]. 20

Figure 2.13 The variation of volume fraction of DRX grains with Zener- Hollomon parameter Z [63]. 21

Figure 2.14 The variation of DRX grain size with Zener-Hollomon parameter Z [63]. 21

Figure 2.15 Texture evolution of AZ31B during compression test at 400°C with

constant strain rate of 10^{-4} s^{-1} [69]..... 22
Figure 2.16 Microstructure after annealing [88]..... 24
Figure 2.17 Effect of roll velocity ratio V_R on shear strain [105]. 26
Figure 2.18 Effect of deformation geometry Δ on shear strain [105]. 26
Figure 2.19 Pole figures of AZ31: (a) symmetrically rolled with 30% reduction at 473K (b) asymmetrically rolled with 30% reduction at 473K [110]. 27
Figure 2.20 Elongation to failure as a function of basal plane intensity of AZ31. [110] 27
Figure 4.1 Sketch routine of heat treatment. 32
Figure 4.2 ASTM dimension of tensile test coupon. 32
Figure 4.3 High temperature tensile test equipment. 33
Figure 4.4 Facets during the deformation stage [121]. 34
Figure 4.5 The gauge element in a tensile specimen with principal directions [122]. 36
Figure 4.6 Load-extension curve showing the jump in load following a sudden increase in strain rate [122]..... 38
Figure 4.7 Geometry of volume fraction calculations for certain plane [26]..... 39
Figure 4.8 Conventional rolling mill for thermomechanical testing. 40
Figure 5.1 Optical micrographs of as-received AZ31 and after different heat treatment. 44
Figure 5.2 SEM micrographs of AZ31 and after different heat treatment. 45
Figure 5.3 Chemical compositions of second phase particles. 46
Figure 5.4 Phase analysis of X-Ray diffraction (XRD) technique. 47
Figure 5.5 Elongation-to-failure of tensile tests at different temperatures as a function of strain rate..... 49
Figure 5.6 True flow stress of tensile tests at different temperatures as a function of strain rate with definite true strain value of 0.1. 50
Figure 5.7 Strain-rate-sensitivity *m* of tensile tests at different temperatures as a function of strain rate. 50
Figure 5.8 Load-displacement curves of SRC tests of AZ31 at 200°C. 52

Figure 5.9 Local true stress-strain curves of tensile tests at high temperatures ranging from 200°C to 400°C with different strain rates 54

Figure 5.10 SEM micrographs of fracture surface after superplastic deformation at 300°C with constant strain rate of 4.4×10-4 s^{-1}..... 56

Figure 5.11 SEM micrographs of etched surface microstructure after superplastic deforma- tion at 300°C with constant strain rate of 4.4×10-4 s^{-1}..... 57

Figure 5.12 Optical microstructure near fracture tip and the corresponding grain size distribu- tion at 200°C and 300°C with different constant strain rate. 60

Figure 5.13 Average grain size near fracture tip as a function of strain rate..... 61

Figure 5.14 Sample surfaces after different rolling schedules 62

Figure 5.15 Optical microstructures after warm rolling at 200°C and corresponding heat treatment. 63

Figure 5.16 Optical microstructures of AZ31 after warm rolling at 300°C and corresponding heat treatment. 64

Figure 5.17 Optical microstructure of as-received AZ31 for warm rolling tests. 64

Figure 5.18 Pole figures of AZ31 after different rolling schedules.. 67

Figure 5.19 Pole figure of as-received AZ31 for warm rolling tests. 68

Figure 5.20 True stress-strain curve for tensile test at 200°C with low strain rate value of 4.4×10^{-4} s^{-1}. 69

Figure 5.21 True stress-strain curve for tensile test at 200°C with high strain rate value of 8.8×10^{-3} s^{-1}. 69

Figure 6.1 Volume fractions of different phases after annealing. 73

Figure 6.2 Equilibrium phase diagram of (Mg+Al+%Zn) varied with Mn. 73

Figure 6.3 Volume fractions of fine grains as a function of strain rate. 76

Figure 6.4 Effect of deformation on DRX. 79

Figure 6.5 Average grain size after different rolling schedules and annealing..... 81

Figure 6.6 Intensity of (0002) after different rolling schedules and annealing. ... 83

Figure 6.7 Optical microstructures near fracture tip after tensile tests of AZ31. ..84

List of Tables

Table 2.1 Slip systems in h.c.p metals [8]. 5

Table 4.1 Chemical composition of as-extruded AZ31 31

Table 5.1 Different rolling schedules of AZ31 62

Table 5.2 Mechanical properties of AZ31 after 200°C tensile tests. 70

Table 6.1 Average grain size after different heat treatment. 72

1. Introduction

The application of automotive magnesium can be traced back to 1960's, but then magnesium was replaced by aluminum due to its high cost. Magnesium attracted the attention again in recent years because of the drive for fuel efficiency. Magnesium is the lightest structural materials among metals because of its low density. Its specific tensile strength and rigidity are superior to iron and aluminum. The greatest limitation for the usage of wrought magnesium is its poor formability at room temperature. Because of its hexagonal closed packed (HCP) crystal structure, only two independent basal slip systems can be activated. However, the ductility of magnesium can be greatly improved at high temperature due to the activation of non-basal slip systems. A fine grain structure and random texture will also improve the ductility of magnesium due to the decrease of volume fraction of twinning and the increase number of basal slip systems that can be activated respectively.

The present research work focuses on the understanding of microstructural stability in magnesium alloy AZ31 during high temperature deformation. This thesis is divided into seven chapters including this chapter. A literature review of related background is presented in chapter 2. The objectives of this research are clearly specified in chapter 3. Experimental procedure is described in chapter 4. All the experimental results and discussion are given in chapter 5 and 6 respectively. The summary of the research is contained in the final chapter.

2. Literature Review

In this chapter, a review of related pages will be given to provide some background to this research project. First of all, the usage of magnesium alloys in automobile industry will be introduced. Some basic knowledge of crystal structure and how it affects the deformation of magnesium with the variation of the temperatures will be discussed. Microstructure evolution during high temperature deformation will also be introduced in this part.

2.1 Automotive Magnesium Alloys

Magnesium was first applied in automotive industry shortly after World War II, Volkswagen used it in the original "Beetle" model. Mazda, Toyota, Porsche also used magnesium parts afterwards [1-3]. However, magnesium was later replaced by aluminum due to its higher cost, poorer thermal and corrosion resistance. In recent years, magnesium attracted attention again in the automotive industry because of its significant contribution to fuel economy and environmental conservation [1-4]. The average application of magnesium for each vehicle has increased from 1 to ~4 kilogram over the past 10 years in North America [1]. Even though this value is still relatively low, many more magnesium auto parts are being developed these days. It has been estimated that over 100 kg of magnesium could be used in each vehicle [1]. Because of its low density, the specific tensile strength and rigidity of magnesium are superior to iron and aluminum as shown in figure 2.1 [3].

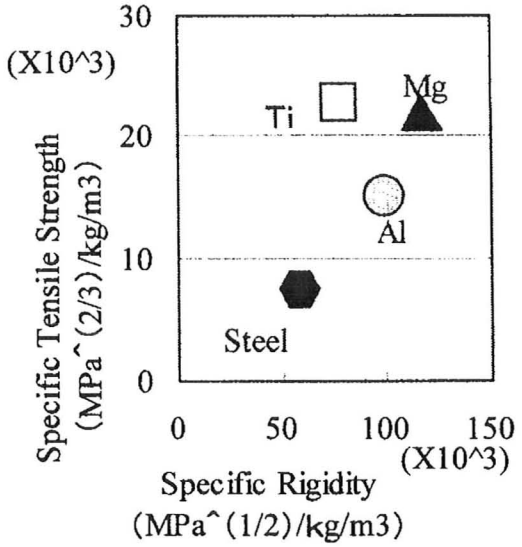

Figure 2.1 Comparison of specific strength and rigidity [3].

2.2 Crystal Structure of Magnesium

The crystal structure for magnesium is hexagonal closed packed (h.c.p), with a c/a ratio of the unit cell of 1.623. The ideal ratio of h.c.p lattice is 1.633 which is very close to that of magnesium [5-24]. The important planes and directions in h.c.p metals are illustrated in figure 2.2. (0001) is the basal plane. {hki0} are called prism planes which are perpendicular to basal planes. $\{1\bar{1}00\}$ planes are prism planes of type I, $\{1\bar{2}10\}$ planes are prism planes of type II. {hkin} (n≠0) are pyramidal planes. When n=1, {hki1} planes are pyramidal planes of type I; n=2, {hki2} are pyramidal planes of type II [5, 8, 25, 26].

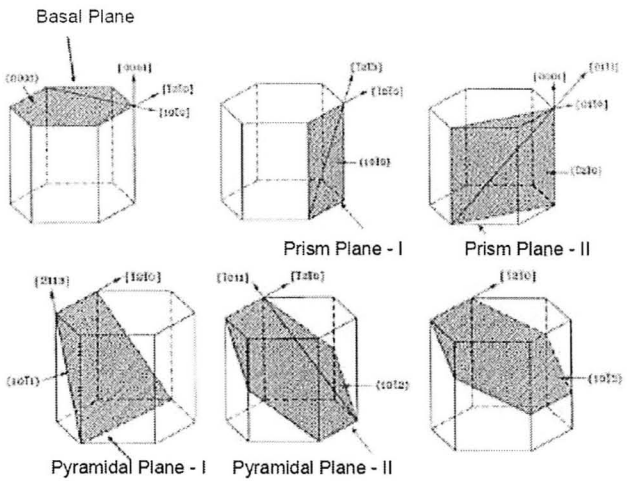

Figure 2.2. Planes and directions in h.c.p metals [8].

2.3 Slip Systems in Magnesium

Slip systems in h.c.p metals are listed in table 2.1. The critical resolved shear stress for basal slip systems and non-basal slip systems is displayed in figure 2.3.

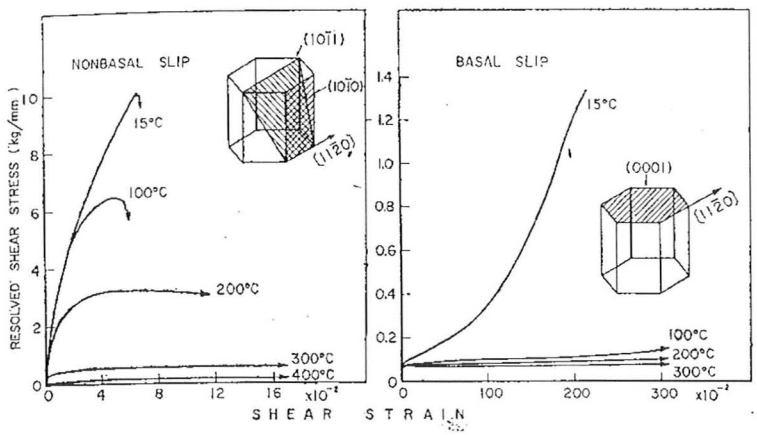

Figure 2.3 CRSS for basal and non-basal slip at room and elevated temperatures [27].

The critical resolved shear stress for non-basal slip systems is much greater than basal slip systems at room temperature, so magnesium can be deformed easily only

within their basal plane at room temperature [12, 14, 16, 18, 20, 25, 27]. From table 2.1, only two independent slip systems exist along slip direction $<11\bar{2}0>$ in basal plane for h.c.p metals. This disobeys Taylor's criteria that at least five independent slip systems are required to be activated for an arbitrary shape change to result. However, when the temperature increases, the critical resolved shear stress for non-basal slip systems will decrease rapidly, thus non-basal slip systems will be activated at elevated temperature. Also, Taylor's criteria will be satisfied for plastic deformation [5-8, 43, 45, 69].

Slip system	*Burgers vector type*	*Slip direction*	*Slip plane*	No. of slip system	
				Total	*Independent*
1	a	$<11\bar{2}0>$	*Basal plane* (0001)	3	2
2	a	$<11\bar{2}0>$	1^{st}*order prism plane* $<10\bar{1}0>$	3	2
3	a	$<11\bar{2}0>$	1^{st}*order pyramidal plane* $<10\bar{1}1>$	6	4
4	$c+a$	$<11\bar{2}3>$	2^{nd}*order pyramidal plane* $<11\bar{2}2>$	3	2
5	c	$<0001>$	1^{st}*order prism plane* $<10\bar{1}0>$	3	2
6	c	$<0001>$	2^{nd}*order prism plane* $<11\bar{2}0>$	3	2

Table 2.1 Slip systems in h.c.p metals [8].

2.4 Twinning in Magnesium

One of the plastic deformation modes in h.c.p metals is twinning, a twin formed during mechanical deformation is called mechanical twinning [28]. Due to the lack of independent slip systems for magnesium during room temperature deformation, mechanical twinning becomes an important deformation mechanism. The dominant twinning mode observed in magnesium is $\{10\bar{1}2\}\langle 10\bar{1}1\rangle$ [5, 29-31]. The formation and growth of the mechanical twinning is also related to the grain size and the texture of polycrystalline materials. The average stress of mechanical twinning for a fine grain size material is higher than the stress for a coarse grain material, because of the greater interaction value between the crystals in a fine grain size case [32].

Even though mechanical twinning can be activated during room temperature deformation for magnesium, this will result in large internal stress, thus leading to reduced ductility [5, 25]. At elevated temperature, mechanical twinning became less important due to the activation of non-basal slip systems as discussed in previous section.

2.5 Superplasticity of Magnesium

Superplasticity is defined as the ability of a polycrystalline material to show very large tensile elongations, usually over 200%, prior to failure. Strain rate sensitivity exponent m generally exhibits high value for superplastic materials during tensile deformation, which is characterized by the following constitutive equation [33]:

$$\sigma = k \dot{\varepsilon}^{m} \tag{2.1}$$

where σ is the true flow stress, $\dot{\varepsilon}$ is the strain rate, k is a constant. In general, most metals and alloys show m value with less than 0.2, while superplastic materials exhibit m value with greater than 0.33. Superplastic behavior is usually achieved at high homologous temperature, typically half of the absolute melting temperature [9-13, 15-24, 33].

2.5.1 Superplastic Forming (SPF)

Application of superlastic forming (SPF) is one feasible method to improve the ductility of magnesium alloys at elevated temperature [9-13, 15-24]. As displayed in figure 2.4, tensile tests were carried out at different high temperatures with different strain rate values of AZ31, average grain size was d=130μm. The strain rate regions exhibiting high m value were in good agreement with the regions where large elongations were attained [22].

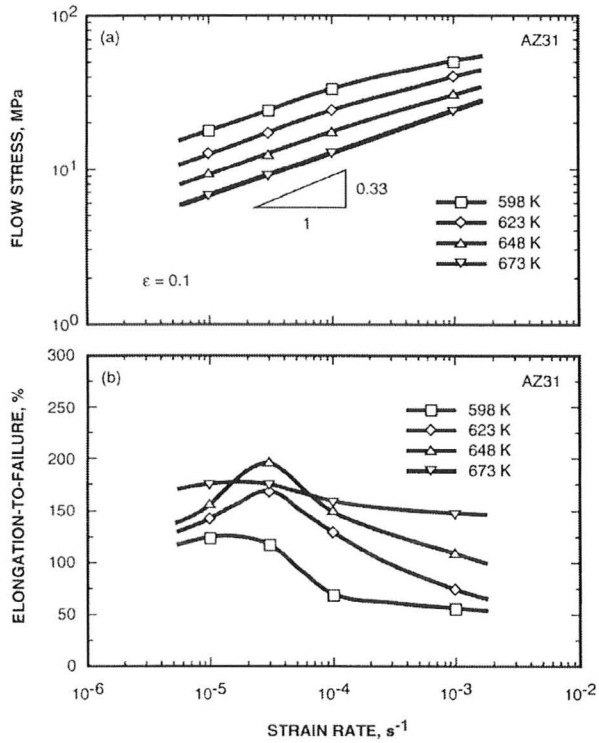

Figure 2.4 The variation in flow stress and elongation-to-failure as a function of strain rate in AZ31 (d=130μm) [22].

2.5.2 Fine-Structure Superplasticity (FSS)

Fine-structure susperplasticity (FSS) is one typical superplastic behavior in polycrystaline solids. Some prerequisites for the development of FSS materials include fine grain size with less than 10μm for metals, presence of second phase particles, high energy between adjacent grain boundaries, etc [9, 11, 13, 21, 33].

The general constitutive rate equation for creep can be described by [34]:

$$\dot{\varepsilon} = A\left(\frac{DGb}{kT}\right)\left(\frac{b}{d}\right)^{p}\left(\frac{\sigma}{G}\right)^{n} \Leftarrow n = \frac{1}{m} \tag{2.2}$$

where $\dot{\varepsilon}$ is the strain rate, d is the grain size, b is Burgers vector, D is the diffusion coefficient, G is the shear modulus, k is Boltzmann's constant, T is the absolute

temperature, n is the stress exponent, m is the strain rate sensitivity, σ is the flow stress, p is grain size exponent, A is constant. Different creep mechanisms can be described by this equation with unique n, p and D value. According to this rate equation, the strain rate $\dot{\varepsilon}$ is inversely proportional to the grain size d to some exponent p. This has also been proved by experimental results as shown in figure 2.5. Fine grain structure can decrease the optimum strain rate value, thus reduce the cost of SPF [20].

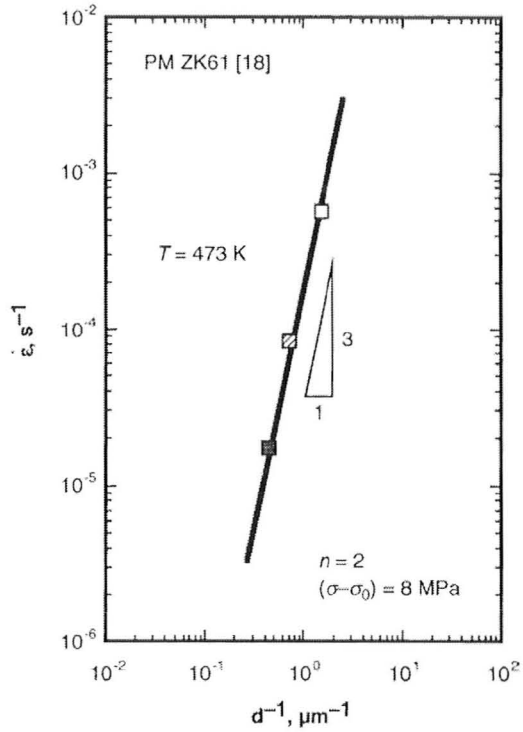

Figure 2.5 The variation in strain rate as a function of the reciprocal grain size at 473K in ZK61 alloys [20].

SPF of wrought magnesium has attracted many investigators' attention and has been put into practical application recently [9, 11-13, 16, 18-23, 33]. Compared with casting technique, SPF can form more complex shaped components of automobile

materials directly from rods and plates, more cost effectively. Also, the mechanical properties of SPF materials are superior to die-casting parts [13].

2.6 Creep Deformation Mechanisms

Creep is a plastic deformation process that occurs at high temperatures, generally above half of the absolute melting point. Three discrete mechanisms can occur at the atomic level during creep deformation: grain boundary sliding accommodated by grain shape changing, dislocation slip and diffusional creep. These three mechanisms can either occur independently of one another to some approximation, or be accommodated by each other [17, 33, 35].

2.6.1 Grain Boundary Sliding (GBS)

Grain boundary sliding is the most commonly considered mechanism for superplastic flow. It is essential to be accompanied by an accommodation mechanism for GBS. Otherwise, premature fracture will occur due to the extensive cavitation, especially near the triple junctions [16, 33, 35-42, 44]. Some dislocation slip processes, grain boundary migration, recrystallization, or diffusional flow might be the accommodation process. Figure 2.6 is the model developed by Fukuyo [46] based on GBS accommodated by slip which involves the sequential steps of glide and climb.

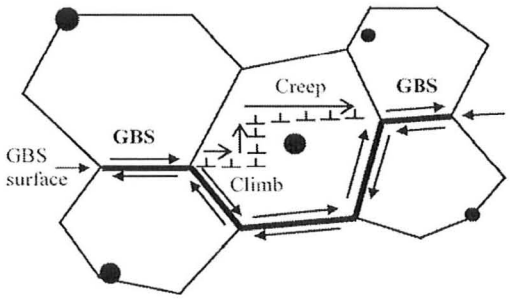

Figure 2.6 A model based on a GBS process accommodated by slip [46].

GBS in fine structure superplastic materials is characterized by typical strain-rate-sensitivity exponents clustered around m=0.5 (n=2). The activation energy is either equal to lattice diffusion energy or grain boundary diffusion energy. Watanabe has derived the constitutive equation for superplasticity in magnesium alloys from equation 2.2 [20]:

$$\dot{\varepsilon} = 1.8\times10^{6}\left(\frac{Gb}{kT}\right)\left(\frac{b}{d}\right)^{2}\left(\frac{\sigma}{G}\right)^{n} D_{eff} \tag{2.3}$$

D_{eff} is the effective diffusion coefficient for superplastic flow in metallic materials, involving the lattice diffusion coefficient D_L and the grain boundary diffusion coefficient D_{gb}. Watanabe also derived the effective diffusion coefficient for superplastic flow in magnesium alloys which is expressed by [20]:

$$D_{eff} = D_{L} + 1.7\times10^{-2}\left(\frac{\pi\delta}{d}\right)D_{gb} \tag{2.4}$$

Langdon [47] has proposed the method to estimate the contribution of GBS to overall strain quantitatively. In high temperature creep, the total strain can be expressed as [36, 47]:

$$\varepsilon = \varepsilon_{gbs} + \varepsilon_{g} + \varepsilon_{dc} \tag{2.5}$$

where ε is the overall strain, ε_{gbs} is the strain due to grain boundary sliding and any accommodated mechanism, ε_g is the strain due to intragranular processes occurring within the grains, ε_{dc} is the strain due to diffusion creep. The contribution of GBS to the overall strain ξ is expressed by [36, 47]:

$$\xi = \frac{\varepsilon_{gbs}}{\varepsilon} \tag{2.6}$$

Bell et al [48] have proposed the equation to calculate ε_{gbs}:

$$\varepsilon_{gbs} = \Phi \frac{\overline{w_1}}{\overline{L_1}} \tag{2.7}$$

where Φ is a constant chosen as 1.5 from creep experiments [47], $\overline{w}$ is the average marker offset measured in the surface perpendicular to the tensile axis, $\overline{L}$ is the mean linear intercept grain size. Tan [19] has estimated the contribution of GBS to overall strain ξ at different strain ranges as depicted in figure 2.7. Tensile test was carried out at 250°C under low strain rate of 1×10^{-4} s^{-1} with AZ31 in this case.

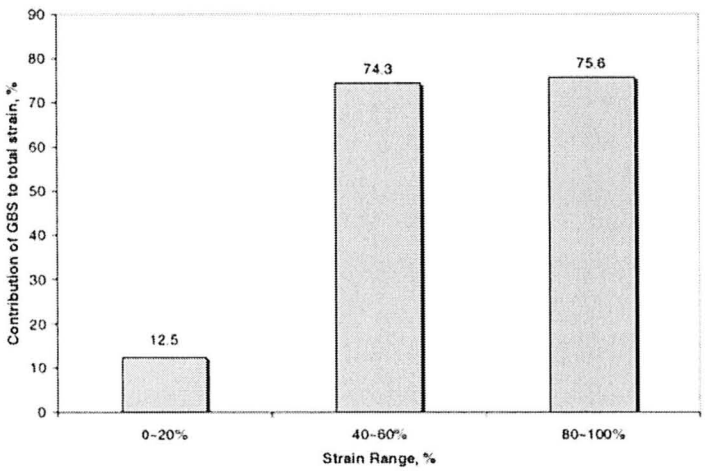

Figure 2.7 Contribution of GBS to overall strain ξ at different strain range [19].

At low levels of strain range 0-20%, the contribution of GBS to overall strain ξ

was only 12.5% which was relatively low. The average grain size was measured as 15-25 μm at this stage, GBS was not fully operative due to such coarse-grained structure. At high levels of strain ranges 40-60% and 80-100%, ξ was increased rapidly to 74.3% and 75.6%. The average grain size was measured as less than 10 μm at both stages, GBS was greatly improved due to accommodated dynamic recrystallization mechanism which resulted in fine grain structure. GBS showed major contribution to overall strain for other fine-grained superplastic alloys as well [49-52].

2.6.2 Dislocation creep

Dislocation creep is defined as dislocation motion in the grain lattice during deformation, which involves both glide-controlled creep and climb-controlled creep.

Glide-controlled creep refers to the process of glide on slip planes. This mechanism occurs mainly because solute atoms impede dislocation motion. [53, 54]. Such kind of alloys are called class I solid solutions. Typical stress exponent n measured in Class I solid solutions are clustered around 3. The creep rate equation can be expressed by [33]:

$$\dot{\varepsilon} = KD_S\sigma^3 \tag{2.8}$$

where D_s is the diffusion coefficient of the solute atom in the alloy.

Climb-controlled creep refers to the process of climb by non-conservative dislocation motion over physical obstacles. It is more difficult than glide-controlled creep mechanism for most metals and alloys. The stress exponent n is usually measured around 4-5. The creep rate equation can be expressed by [55]:

$$\dot{\varepsilon} = KD_L\sigma^n \tag{2.9}$$

where D_L is the lattice diffusion coefficient.

2.6.3 Diffusional creep

Diffusional creep is defined as high temperature deformation due to the transport of matter by diffusion. It usually occurs at high temperatures around 0.9 T_m in fine structure of materials [33]. Diffusional creep can be divided into Nabarro-Herring creep and Coble creep. For the Nabarro-Herring creep, the transport of matter is by lattice diffusion, while for the Coble creep, the transport of matter is by grain boundary diffusion. The Nabarro-Herring creep has less grain size dependence than Coble creep. Also, the activation energy for Nabarro-Herring creep is greater than that for Coble creep [56].

2.6.4 Effect of grain size

Creep deformation mechanisms for coarse-grained alloys and fine-grained alloys are different. The rate equation for creep can also be expressed as [57]:

$$\dot{\varepsilon} = A\left(\frac{b}{d}\right)^{p}\left(\frac{\sigma-\sigma_0}{G}\right)^{n} D_0 \exp\left(-\frac{Q}{RT}\right) \qquad (2.10)$$

where σ_0 is the threshold stress, D_0 is the pre-exponential factor for diffusion, Q is the activation energy, R is the gas constant, T is the absolute temperature. This describes many processes for which no creep occurs below a stress σ_0.

Watanabe [22] has demonstrated that glide-controlled dislocation creep is the deformation mechanism for coarse-grained AZ31 during high temperature tensile tests, with an average grain size of 130 μm. From the experimental results, Watanabe characterized the stress exponent n of 3, grain size exponent p of 0 and activation

energy Q, which is close to the activation energy (143±10 kJ/mol) for solute diffusion of Al in Mg. The constitutive equation for coarse-grained AZ31 was expressed as [22]:

$$\dot{\varepsilon} = 2\times 10^{19}\left(\frac{\sigma-\sigma_0}{G}\right)^3 D_S \tag{2.11}$$

This equation matched well with glide-controlled creep equation 2.8. From the previous experimental data, dislocation creep deformation behavior in some other coarse-grained magnesium alloys has also been investigated. From figure 2.8, Vagarali and Langdon 1982 has also proved the glide-controlled dislocation creep as the dominant deformation mechanism for coarse-grained Mg-0.8Al alloys [58, 59], Saeki and Otsuka 1997 found the same result in Mg-3Al and Mg-5Al, all of those alloys behaved as Class I alloy [38].

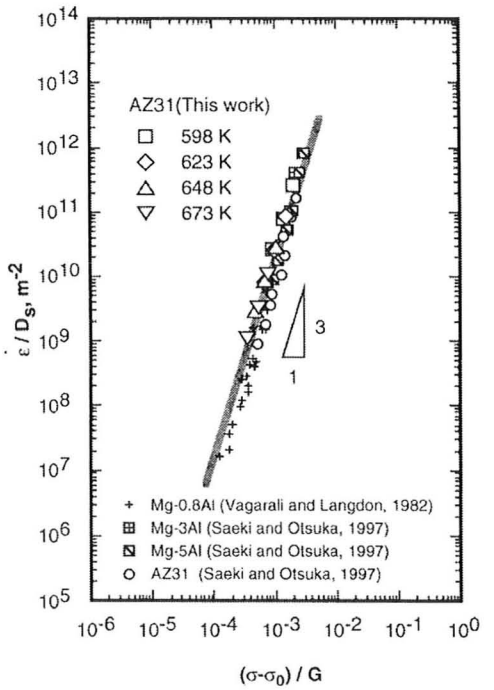

Figure 2.8 Experimental data for coarse-grained magnesium alloys of solute diffusion compensated strain rate as a function of threshold stress and shear modulus compensated stress [22].

Grain boundary sliding (GBS) was generally shown to be the dominant deformation mechanism in fine structure superplastic materials during high temperature tensile tests [14, 19, 23, 33, 35, 42, 44]. Several authors have reported GBS accommodated by dislocation slip in magnesium alloys, which is the most common mode of deformation [39, 41]. Sherby and Wadsworth [35] have shown that the experimental data agree well with the creep equation of GBS accommodated by slip:

$$\dot{\varepsilon} = 2\times10^{9}\left(\frac{b}{d}\right)^{2}\frac{D_L}{b^2}\left(\frac{\sigma}{E}\right)^{2} \tag{2.12}$$

Superplastic behavior was observed in fine structure magnesium alloys. Morhri (2000) has studied the fine-grained Mg-9Al-1Zn alloy which was demonstrated to deform superplastically by GBS during high temperature tensile tests [16]. Wei [23] observed GBS was still the dominant deformation mechanism of rolled AZ91 at high strain rates ranging from 10^{-3} to 1 s^{-1}, which was accommodated by dislocation creep. Panicker [44], Tan [18, 19], and Yorinobu [42] have also observed GBS as the dominant deformation mechanism in fine-grained magnesium alloys during high temperature tensile tests.

Heterogeneous grain structure due to the abnormal grain growth had some negative effect on formability. Bussiba [9] has observed microcracks at the interface of the fine-coarse grain of deformed ZK60, which was due to the different deformation mechanism for coarse grain and fine grain structure as discussed above. This would decrease superplasticity of materials. Thus, abnormal grain growth should be avoided during the deformation.

2.7 Microstructure stability

2.7.1 Recovery

Recovery may occur on annealing after deformation or during deformation at high temperatures, the latter one is also called dynamic recovery. Recovery is the stage prior to recrystallization after deformation, which occurs primarily due to changes in the dislocation distribution within the material. The properties of the materials will be partially restored to the values before deformation through recovery. During recovery, when the dislocation density rises, the driving force and hence the rate of recovery increases [7, 60].

Dynamic recovery plays an important role in the creep and hot working of magnesium alloys, a microstructure of subgrains and low angle boundaries forms. Tan [18] observed microstructure following dynamic recovery of AZ31 under TEM, at the strain value of 40%, as depicted in figure 2.9. Fine subgrains and serrated grain boundary were clearly recognized.

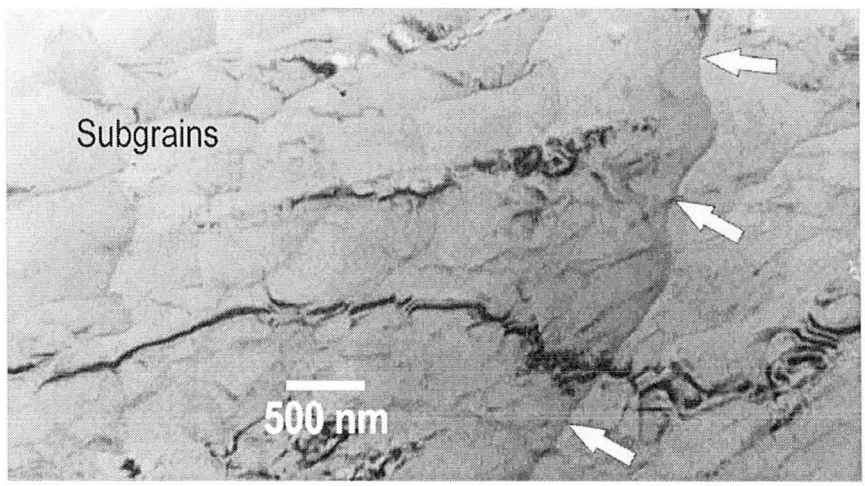

Figure 2.9 Subgrain structure and serrated grain boundary (white arrows) of AZ31 strained to 40% at 250°C with the constant strain rate of 1×10^{-4} s^{-1} [18].

Dislocation structure near the subgrain boundaries and within the subgrains also can be observed as displayed in figure 2.10. Cells of tangled dislocation walls can be observed within the coarser grain, as shown in the left one of figure 2.10. The subgrain structure was converted from these fine dislocation cell during the recovery process.

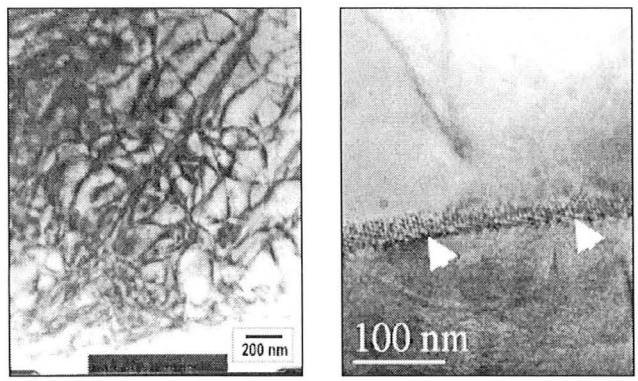

Figure 2.10 Fine dislocation cell structures within coarser grain (left) and dislocation array (right) of AZ31 strained to 40% at 250°C with the constant strain rate of 1×10^{-4} s^{-1} [18].

Myshlyaev [61] showed that the enhanced dynamic recovery played a significant role to improve ductility during elevated temperature torsion test of AZ31. J. Koike (2003) has found dynamic recovery at room temperature during the ECAE-processed AZ31B and non-basal slip systems were activated [62].

2.7.2 Recrystallization

Recrystallization (DRX) refers to a process of further restoration in which new dislocation-free grains formed within the deformed or recovered structure, the original

deformed grains will be consumed by newly nucleated and grown undeformed grains. Recrystallization that occurs during the deformation is called dynamic recrystallization; on the other hand, recrystallization that occurs after the deformation is called static recrystallization. Recrystallization can also be divided into continuous and discontinuous processes. Discontinuous recrystallization has clear nucleation and growth stages and dislocations are removed by eliminating high angle grain boundaries. Continuous recrystallization has no identifiable nucleation and growth stages and dislocations still remain in the recrystallized grains, which is generally considered as a recovery process whereby low angle boundaries transform to high angle boundaries [7, 11, 60, 63-67].

New fine grains nucleate at the old grain boundaries. A necklace structure of recrystallized grains may be formed. Tan [18] has found evidence for the transformation from low angle grain boundaries (<15°) to high angle grain boundaries (>15°) during dynamic recrystallization. Figure 2.11 showed the TEM micrograph of an undeformed specimen and three neighboring grains with corresponding diffraction patterns, which showed small misorientation angles 1~2° between each other. Figure 2.12 showed the TEM micrograph of DRX specimen and two neighboring subgrains with corresponding diffraction patterns, which showed large misorientation angles 28° between subgrains, which is attributed to DRX.

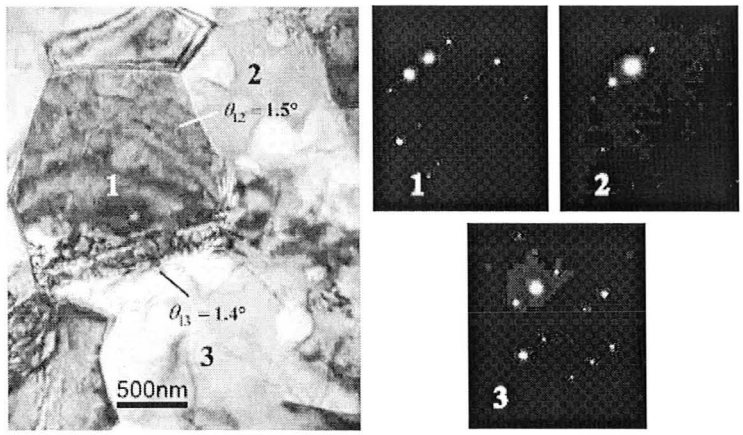

Figure 2.11 TEM structure of undeformed AZ31 and the diffraction patterns of the corresponding grains [18].

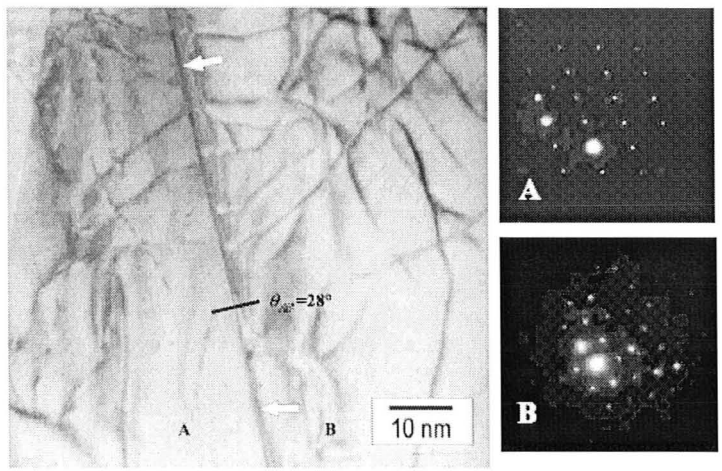

Figure 2.12 TEM structure of DRX specimen and the diffraction pattern of the neighboring subgrains A and B, white arrows indicate the subgrain boundary, of AZ31 strained to 60% at 250°C with the constant strain rate of 1×10^{-4} s^{-1} [18].

Fatemi-Varzaneh et al [63] have studied the effect of thermomechanical parameters on the microstructural evolution of AZ31 during high temperature compression tests, as depicted in figure 2.13 and figure 2.14. Two important parameters strain rate $\dot{\varepsilon}$ and deformation temperature T can be combined using the Zener-Hollomon parameter Z, which is defined as [60]:

$$Z = \dot{\varepsilon} \exp\left(\frac{Q}{RT}\right) \tag{2.13}$$

where Q is the activation energy, R is the constant. It is convenient to use Z value for discussions of hot working processes in which combined effects of temperature and strain rate on DRX can be easily investigated. The volume fraction of DRX grains and DRX grain size was reduced by increasing the Z values. Kaibyshev [68] also found the similar results for magnesium alloys.

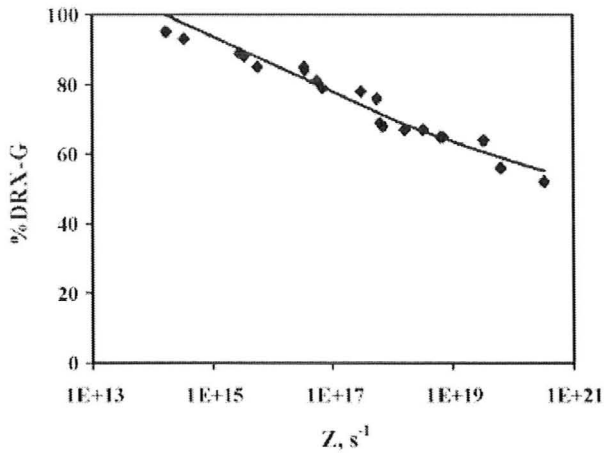

Figure 2.13 The variation of volume fraction of DRX grains with Zener-Hollomon parameter Z [63].

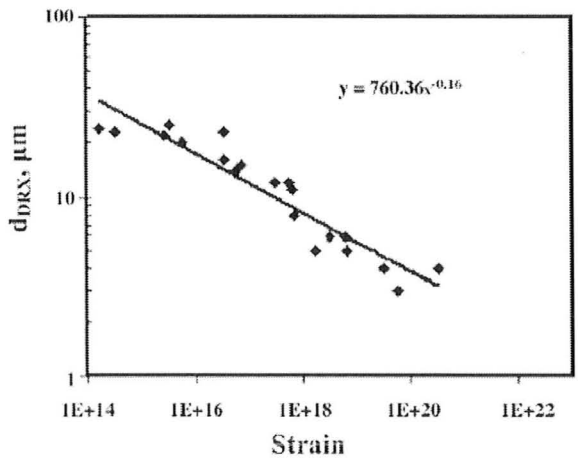

Figure 2.14 The variation of DRX grain size with Zener-Hollomon parameter Z [63].

DRX also has effect on the texture randomization. Al-Samman [69] found that texture randomization is caused by the compression test at the lowest Z value of AZ31B, at a temperature of 400°C with 10^{-4} s^{-1} strain rate. As the deformation strain increased, the basal plane gradually reoriented until reach an almost random texture at ε=-1.6 as displayed in figure 2.15. Al-Samman [69] also revealed the influence of Zener-Hollomon parameter Z on the texture evolution. At higher deformation temperatures, strain rate sensitivity had a stronger effect on texture evolution than lower temperature.

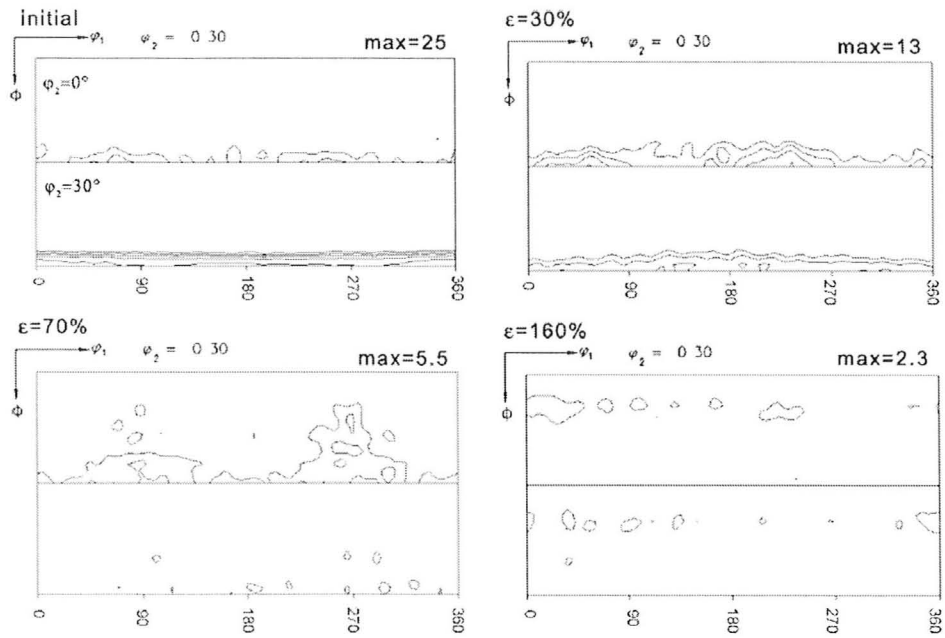

Figure 2.15 Texture evolution of AZ31B during compression test at 400°C with constant strain rate of 10^{-4} s^{-1} [69].

Panicker [66], Yang [67], Tan [18], Galiyev [11], Bussiba [9], Fatemi-Varzaneh [70] have reported strain softening behavior due to the DRX during deformation of magnesium alloys, in which flow stress decreased after the peak value for both tensile

or compression tests. Also, DRX showed effective grain refinement during the deformation of magnesium alloys, which led to the improvement of GBS, thus superplastic behavior might be observed.

2.7.3 Grain growth

Grain growth is a process following recrystallization during further annealing, in which smaller grains are eliminated and larger grains grow. Grain growth can be divided into normal grain growth and abnormal grain growth. In normal grain growth, the microstructure coarsens uniformly. In some cases, only a few large grains grow; this process is called abnormal grain growth or secondary recrystallization [60]. Considering the effect of second phase particles and based on the general equation from Burke and Turnbull [71], the rate of grain growth can be expressed by:

$$\frac{dR}{dt} = M(P - P_Z) = M\left(\frac{\alpha\gamma}{R} - \frac{3F_V\gamma}{2r}\right) \tag{2.14}$$

where M is the grain mobility, P is the driving pressure for grain growth, P_Z is the pinning pressure due to second phase particles, α is the constant, γ is the surface energy, R is the radius of grain curvature, F_V is the volume fraction of particles, r is the radius of particles. Second phase particles may show pinning effect on grain growth [72-87].

Yamamoto [88] has reported the grain growth of AZ31 after different heat treatment. Effect of manganese addition has been investigated as depicted in figure 2.16 AZ31 with almost no Mn addition showed rapid grain growth after annealing at 673K for

one hour, while AZ31 with certain percentage of Mn addition (0.433wt%) remained fine grain sized under the same annealing condition. Mn addition does have some effect on suppressing grain growth, second phase particles showed pinning effect.

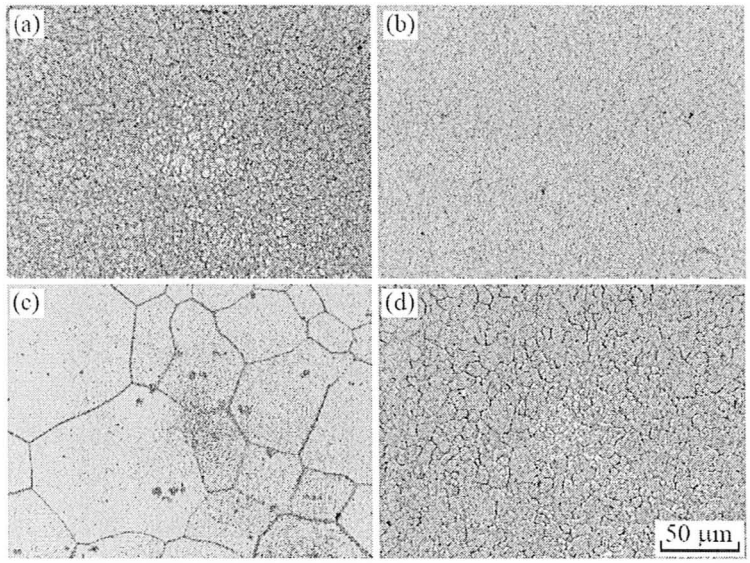

Figure 2.16 Microstructure after annealing at (a) (b) 473K and (c) (d) 673K for one hour, (a) (c) is the AZ31 (0.003% Mn), (b) (d) is the AZ31(Mn) (0.433% Mn). [88].

Several authors have proved the Calcium (Ca) and Strontium (Sr) additions had grain refinement on as-cast microstructure in AZ91 and AZ80 alloys [89-91]. Essadiqi has found Calcium (Ca) addition showed grain refinement during thermomechanical processing in AZ31 alloys, Ca-rich precipitates reduced the grain boundary mobility. Also, some studies on the grain refinement due to second phase particles of both cast and wrought Magnesium alloys have been carried out [92-94].

2.8 Thermomechanical processing

Several methods have been investigated for the grain refinement of magnesium

alloys including warm rolling plus heat treatment, hot extrusion, hot working of magnesium alloy powder, severe plastic deformation, equal channel angular extrusion (ECAE), etc. Warm rolling is the most promising technique for magnesium alloys and it can be put into practical mass production [95-104]. Chang [95] has observed effective grain refinement of AZ31 by conventional rolling.

Asymmetric rolling refers to the conditions wherein velocities or diameters of two work rolls are different [105]. Compared to conventional rolling, asymmetric rolling is more effective on microstructure modification and texture evolution, thus enhancing the ductility and formability of magnesium alloys. Intense shear deformation can be introduced into asymmetric rolling by making the velocities or diameters of two rolls different. Thus, the basal plane of magnesium alloys can be weakened [106]. Roumina [105] has given out some calculations of shear strain through the thickness of AA5754. Effect of roll velocity ratio and deformation geometry on shear strain values are displayed in figure 2.17 and figure 2.18 respectively. Kim [107] has estimated shear deformation in AZ31 sheets through asymmetric rolling using finite element analysis.

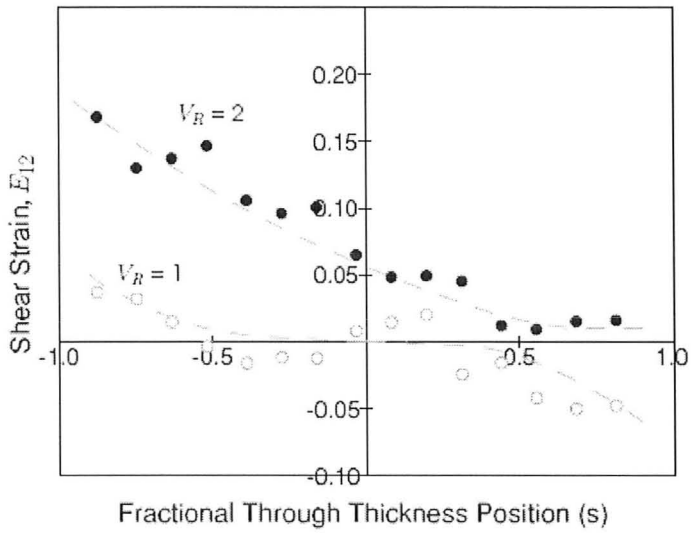

Figure 2.17 Effect of roll velocity ratio V_R on shear strain [105].

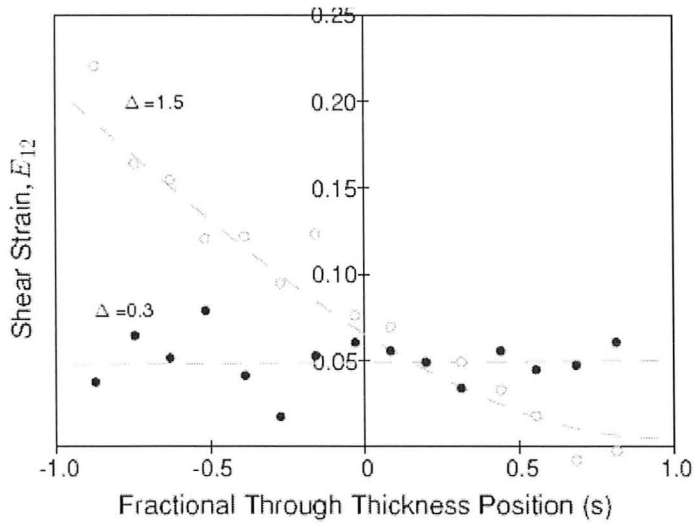

Figure 2.18 Effect of deformation geometry Δ on shear strain with fixed V_R=2 [105].

Texture evolution due to asymmetric rolling has been studied. Kang [127] proved a relatively higher fraction of shear textures contained in asymmetrically rolled aluminum alloy AA6111 sheets than conventionally rolled ones. Kim [110] has compared (0002) and $(10\bar{1}1)$ pole figures of the AZ31 sheets rolled under different conditions as shown in figure 2.19. With the same thickness reduction 30%,

asymmetrically rolled sample showed more random texture than symmetrically rolled sample. This agrees with the observation by Kim [109], who also found that asymmetric rolling induced a texture gradient of AZ31 sheets. The intensity of basal plane decreased from the upper surface through the center to the lower surface, and the ratio of upper to lower roll diameter is 1.5. Kim [110] also found the relationship between texture intensity and ductility as shown in figure 2.20. The tensile elongation increased with decreasing intensity of basal plane (0002).

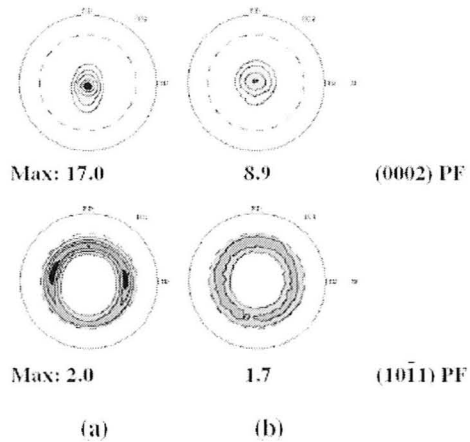

Figure 2.19 The (0002) and (10 $\bar{1}$ 1) pole figures of AZ31: (a) symmetrically rolled with 30% reduction at 473K (b) asymmetrically rolled with 30% reduction at 473K. [110]

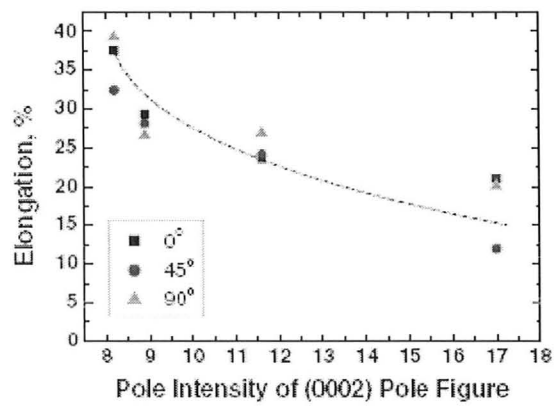

Figure 2.20 Elongation to failure as a function of basal plane intensity of AZ31. [110]

Several authors have also investigated the effect of asymmetric rolling on microstructure evolution and corresponding mechanical properties of magnesium alloys. Huang [108] has studied the effect of differential speed rolling on microstructure and mechanical properties of AZ80. Other magnesium alloys AZ61, AZ91 etc have also been explored to improve formability at different temperature ranges by introducing asymmetric rolling methods [106, 111-114].

3. Research Objectives

The objective of this research is to improve the ductility of magnesium alloys based on fine grain structure, which include the following topics:

1. Microstructural characterization of magnesium alloys after different heat treatment. The objective is to measure the grain growth and particle dissolution as a function of temperature.
2. Superplastic behavior characterization of magnesium alloys based on fine grain structure, at temperature range from 200°C to 400°C under the strain rate range from 2.7×10^{-4} s^{-1} to 8.8×10^{-3} s^{-1}. The objective is to measure the ductility and strain rate sensitivity as a function of temperature and strain rate and to determine the dominant deformation mechanism.
3. Investigate further grain refinement through warm rolling of magnesium alloys. The objective is to decrease the average grain size to less than 10 μm, comparing the effect of symmetric and asymmetric rolling on microstructure modification.
4. Mechanical properties characterization of magnesium alloys after warm rolling processing. The objective is to determine the texture behavior before and after warm rolling.

4. Experimental Procedures

4.1 Introduction

The extruded magnesium AZ31 alloy was used in this research. It is one of the most commonly used wrought magnesium alloys in automobile industry. All materials were produced industrially.

Heat treatment was carried out to characterize the microstructural stability of AZ31 at high temperature. Static grain growth was measured by linear intercept method. Chemical compositions of particles were analyzed by energy dispersive spectrum (EDS). More accurate phase measurement was studied through X-ray diffraction (XRD) method.

Tensile tests were performed at different elevated temperatures with different strain rates to evaluate the superplastic behavior of materials. Ductility is a measure of the degree of plastic deformation before fracture, which can be expressed quantitatively as percent elongation. Strain rate sensitivity m value is an important parameter to evaluate the superplasticity of materials.

Symmetric and asymmetric warm rolling tests were carried out to investigate further grain refinement of materials. Texture analysis was characterized by X-ray diffraction (XRD) method, pole figures of basal plane were plotted. Mechanical properties after warm rolling have been explored, including yield strength, ultimate tensile strength and ductility.

Microstructures were characterized by optical microscopy (OM) and scanning

electron microscopy (SEM), while image processing tools were utilized to make some analysis of microstructure.

4.2 Materials

The wrought magnesium alloy sheet used in this study was as-extruded AZ31, which was extruded at 400°C. The material was produced commercially and supplied to McMaster by GM Corporate Research & Development Centre in Warren, MI. The initial thickness of the material was 1.67mm. The chemical composition of as-extruded AZ31, as determined by inductively coupled plasma (ICP) spectrometry, is shown in Table 4.1. The data in this table was given in weight percent. Except for some primary elements in AZ31, Aluminum (3.03%) and Zinc (0.97%), there is certain percentage of Manganese (0.31%) in this material.

Table 4.1 Chemical composition of as-extruded AZ31.

	Al	Zn	Mn	Fe	Ce	Cu	Zr	Ni
mass %	3.03	0.97	0.31	0.01	0.006	0.003	0.002	0.001

4.3 Heat treatment

Heat treatment was carried out in a furnace, as displayed in figure 4.1. The annealing temperature ranged from 300°C to 550°C. All specimens were annealed in Argon to be protected from oxidation and self ignition [115]. The annealing lasted for

1 hour at different temperatures. All specimens were then cooled by water quenching.

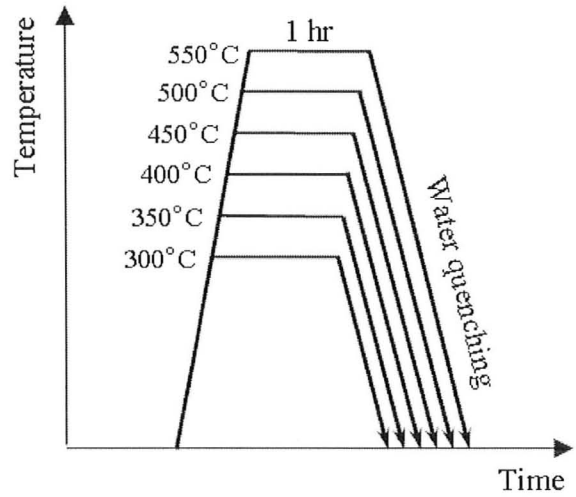

Figure 4.1 Sketch routine of heat treatment.

4.4 Tensile Testing

Tensile specimens were machined according to ASTM standard E-2448 with 19 mm gauge length, 6 mm width as depicted in figure 4.2 [116]. The coupon had a fillet radius of 3 mm, which was different from the standard (1.5mm). The initial thickness of the specimen is 1.67 mm. The tensile direction was the extrusion direction for all the specimens.

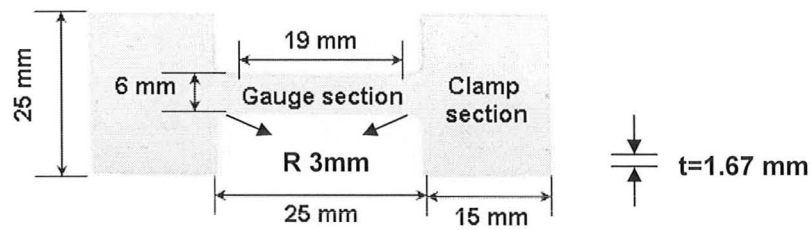

Figure 4.2 ASTM dimension of tensile test coupon.

High temperature tensile tests were performed in MTS Series 810 materials testing machine, equipped with an Instron SFL2702 Environmental Chamber as shown in figure 4.3. The MTS testing machine had two load cell systems, 250 kN and 5000 lbf. The smaller load cell (5000 lbf) is more suitable for magnesium alloys and it can record more accurate data. The Environmental Chamber was installed with a low refractive index window, deformation behavior can be observed through the window and recorded by the camera. Digital image correlation (DIC) system Aramis 6.1 system was used to follow the deformation patterns within gauge section.

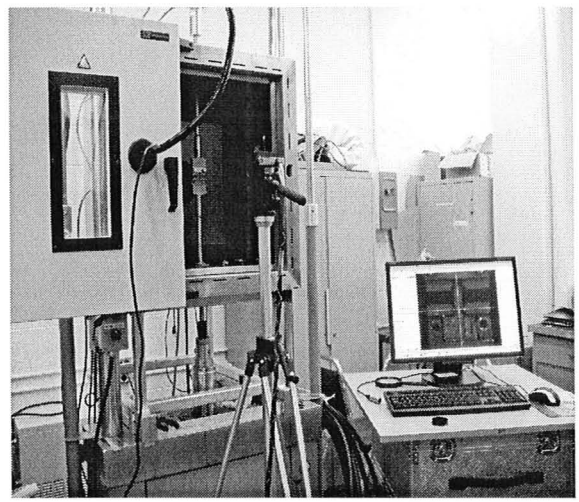

Figure 4.3 High temperature tensile test equipment.

Tensile specimens were stress-relieved at 345°C for 15 minutes after being conventionally machined prior to testing. All tests were conducted by raising the temperature to the set value, followed by 10 minutes holding to ensure the thermal equilibrium. The temperatures for tensile tests were determined to be 200°C, 300°C and 400°C, with constant strain rates ranging from 2.7×10^{-4} s^{-1} to 8.8×10^{-3} s^{-1}. All grips were coated with EKamold® EP Aerosol Boron Nitride Spray to reduce wear

and improve sliding properties during high temperature tensile tests above 200°C.

4.5 Digital Image Correlation

Digital Image Correlation (DIC) is a non-contact optical method to measure the deformation on the surface of an object. DIC tracks a black and white random speckle pattern in small neighborhoods called facets during the deformation, as indicated in red square in figure 4.4. The distance between one facet to the left edge of adjacent facet is referred to the facet step. DIC technique has been used to characterize stress strain values in dual-phase steels [117], characterize strain in deformation bands in aluminum sheets [118], measure local strains in aluminum [119], perform full-field strain measurement in aluminum alloy AA5754 [120], or to compute the true stress-strain curve in AZ31 [15].

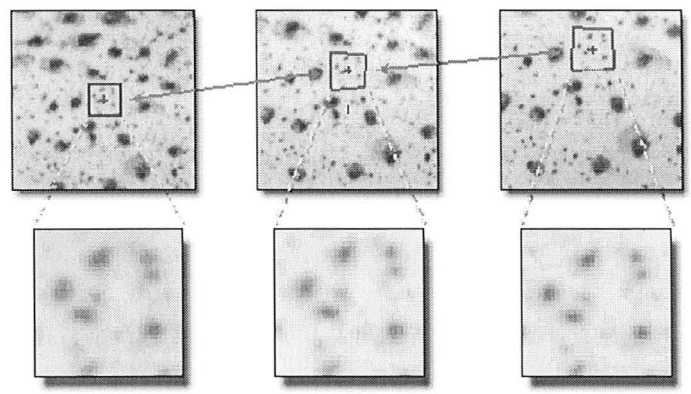

Figure 4.4 Facets during the deformation stage [121].

In this research, two-dimensional (2D) digital image correlation (DIC) was utilized to measure in-plane deformation and displacement fields of plastically deforming magnesium sheet. A set of digital images that store the deformation history recorded

from initial stage up to fracture was input to the correlation algorithm. After the tensile test, those images can be compared in a cumulative series. They can either compare an earlier image with a later one or in an incremental fashion. A linear radiometric transformation is adapted to compensate for differences in brightness between the initial and deformed image, which can be briefly expressed by the following equation [121]:

$$g_1(x,y) = b_1 + b_2 g_2(x_t, y_t) \tag{4.1}$$

where g_1 and g_2 are the initial and deformed images, and x and y are the co-ordinates on the image.

A random speckle pattern was formed on the surface of tensile specimens by spraying black and white high temperature paint. One high resolution LCD camera was contained in Aramis 2D system to record all the images. The frequency of recording images ranged from every 1 second per image to every 30 seconds per image according to different temperatures and strain rates. The upper limit of the Aramis 6.1 system is 500 images for each test. A facet size of 11×9 pixels together with a facet step of 9 pixels was used. In some cases, increasing the facet size and decreasing the facet step will help to improve the calculation. All the images were calibrated using the width of specimens' gauge section 6mm prior to strain measurement. True strain data both parallel and perpendicular to tensile axis, as discussed above ε_1 and ε_2, can be obtained from Aramis system.

4.6 True stress-strain curve calculation

True stress-strain curves can be calculated with the help of Aramis system by recording true strain value in the local area, followed by correlating the frequency of true strain data to the load-displacement data recorded by the MTS software. Figure 4.5 displays the gauge element in a tensile specimen, 1, 2 and 3 are the principal directions along the tensile axis, across the width and through the thickness.

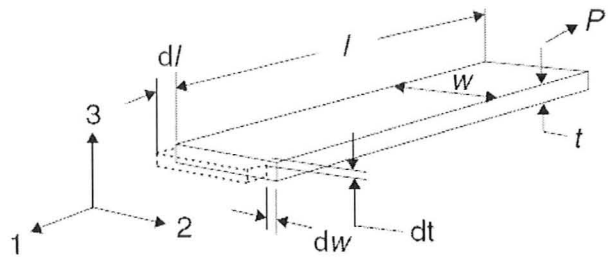

Figure 4.5 The gauge element in a tensile specimen with principal directions [122].

Assume l_0, w_0, t_0 are the initial length, width and thickness respectively, which can be measured by digital caliber before the tensile test. l_i, w_i, t_i are the instantaneous length, width and thickness respectively. The principal true strain values along three directions are given by equations:

$$\varepsilon_1 = \ln\left(\frac{l_i}{l_0}\right), \quad \varepsilon_2 = \ln\left(\frac{w_i}{w_0}\right), \quad \varepsilon_3 = \ln\left(\frac{t_i}{t_0}\right) \tag{4.2}$$

True strain ε_1 and ε_2 can be measured by Aramis system using the recording camera images during the deformation processing. Assuming the plastic deformation occurs at constant volume, ε_3 can be calculated within the gauge region, which is expressed by [122]:

$$\varepsilon_1 + \varepsilon_2 + \varepsilon_3 = 0 \Rightarrow \varepsilon_3 = -(\varepsilon_1 + \varepsilon_2) \tag{4.3}$$

Thus the instantaneous thickness and width of the specimen can be calculated as:

$$t_i = t_0 \exp(\varepsilon_3), \quad w_i = w_0 \exp(\varepsilon_2) \tag{4.4}$$

True stress value is expressed by the following equation using the instantaneous load values F_i from MTS software:

$$\sigma_i = \frac{F_i}{A_i} = \frac{F_i}{w_i \times t_i} \tag{4.5}$$

Also, the ductility of the sample can be determined:

$$\%El = \frac{l_{\max} - l_0}{l_0} \times 100\% = \frac{l_{\max} - 19}{19} \times 100\% \tag{4.6}$$

where l_0 is the gauge length, l_{max} is the maximum extension right before fracture, %El is the elongation-to-failure.

4.7 Strain-rate-sensitivity m measurements

The strain-rate-sensitivity exponent m is an important parameter to measure the superplastic behavior of materials. Strain rate change (SRC) test is the most effective way to measure the strain-rate-sensitivity. SRC test should be performed during the uniform deformation region of the tensile test [116, 122]. As shown in figure 4.6, once the strain rate value jumps suddenly from a lower one $\dot{\varepsilon}_1$ to a higher one $\dot{\varepsilon}_2$ (generally the ratio of higher value to lower value is more than factor 10), a small jump of load, from P_1 to P_2, can be observed in load-extension (displacement) curve.

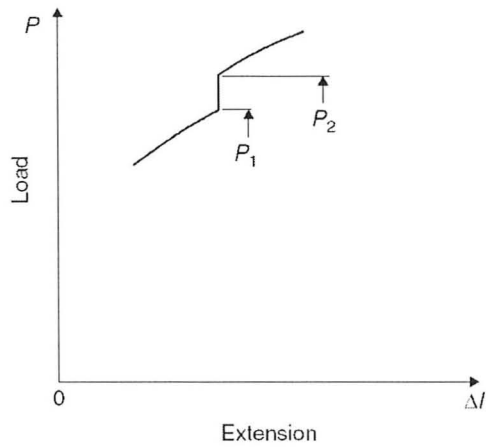

Figure 4.6 Load-extension curve showing the jump in load following a sudden increase in strain rate [122].

Derived from the constitutive equation (2.1), the strain-rate-sensitivity m value can be expressed by:

$$m = \frac{d\log\sigma}{d\log\dot{\varepsilon}} \tag{4.7}$$

Substituting load value P_1 and P_2 into the equation, the equation is expressed as:

$$m = \frac{\log(P_1/P_2)}{\log\left(\dot{\varepsilon}_1/\dot{\varepsilon}_2\right)} \tag{4.8}$$

In this research, strain rate change (SRC) tests were carried out at 200°C to measure the strain rate sensitivity value, with strain rate jumps from 2.7×10^{-4} s^{-1} to 8.8×10^{-4} s^{-1} and 8.8×10^{-4} s^{-1} to 8.8×10^{-3} s^{-1} respectively.

4.8 Texture analysis

Texture analysis was performed using Burker D8 X-ray diffraction goniometer supplied by Burker instruments. A two dimensional CCD detector was used to collect diffraction pattern over a range of 2θ. Copper kα radiation was used for the analysis.

The original data were processed using GADDS software [123], which was then subsequently processed and plotted as basal plane (0002) pole figures using Multex Area software [124] and MTM-FHM software. Texture measurements were performed along the extrusion direction.

Intensity of the basal plane (0002) can be observed from pole figures, the volume fraction (V_f) of the basal plane is the integral of the intensity within a certain angle range which can be expressed by the following equation [26]:

$$V_f = \frac{\int_0^{\beta_c}\int_0^{2\pi} I(\alpha,\beta)\sin(\beta)d\alpha \cdot d\beta}{\int_0^{\frac{\beta}{2}}\int_0^{2\pi} I(\alpha,\beta)\sin(\beta)d\alpha \cdot d\beta} \tag{4.9}$$

where I is the peak intensity, α and β are the diffraction vector, and β_c describes the angle from the pole of interest; 10 degrees was chosen in this research. The geometry was illustrated in figure 4.7.

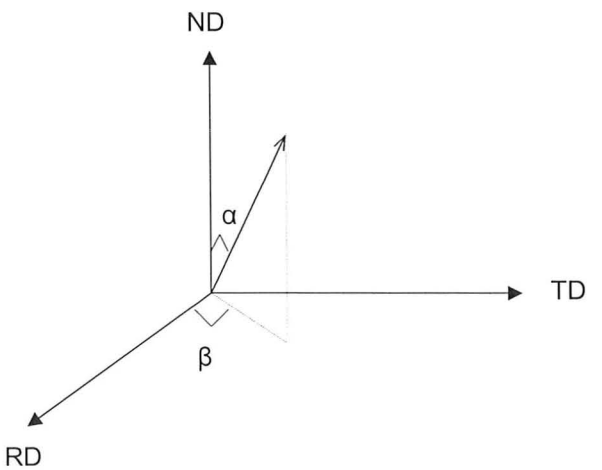

Figure 4.7 Geometry of volume fraction calculations for certain plane [26].

4.9 Warm Rolling

Warm rolling tests of AZ31 sheets were performed using a conventional laboratory rolling mill at UBC, as displayed in figure 4.8. The diameter of both rolls is 152 mm. The velocities of two work rolls can be controlled independently using a single electric motor through a gear box. The top roll was connected to an independent servohydraulic motor which can be driven over a continuous range of velocities. While the velocity of the bottom roll is set as 13.98 rev/min. The velocities of top roll driven hydraulically and bottom roll driven by electric motor can be monitored using the encoders. To achieve asymmetric conditions, the velocity of bottom roll is fixed while the velocity of top roll scaled to reach different speed ratio. In this research, the velocity of top roll was set as 20.97 rev/min and the roll velocity ratio V_R was 1.5 for the asymmetric rolling.

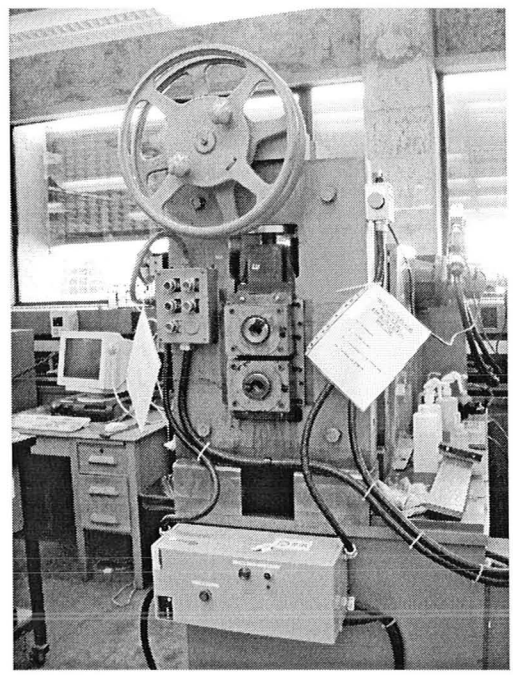

Figure 4.8 Conventional rolling mill for thermomechanical testing.

All rolling specimens were cut into dimension of 3-cm-width ×7-cm-length. The rolling direction was parallel to extrusion direction. Before the test, the roll surface was cleaned and greased using SiC paper and caustic NaOH solution to remove aluminum and magnesium deposited on the rolls. Some aluminum pieces were annealed to 200°C to warm the rolls. Warm rolling was performed at 200°C and 300°C for both symmetric and asymmetric cases. The total reduction in thickness was set as 40% approximately. Different rolling schedules were used to achieve this total reduction at different temperatures. At 200°C, 3-4 passes with approximately 5-10% was conducted; while at 300°C, 8 passes with approximately 10-15% was conducted. All specimens were annealed at 200°C for 1 hour after the rolling tests.

4.10 Microstructure Characterization

Optical microscopy and scanning electron microscopy (SEM JSM-7000F) was utilized to observe microstructure. Samples after different heat treatment and tensile tests were cut by low speed blade sawing to prevent twinning deformation. Sectioned samples were cold mounted using epoxy resin mixed with epoxy hardener. Five steps included four grinding steps: 800 grid SiC, 1200 grid SiC, 2400 grid SiC, 4000 grid SiC paper, and three polishing steps: 9 μm MD-Nap cloth with Struers blue alcohol based lubricant solution and diamond suspension, 3 μm MD-Nap cloth also with Struers blue alcohol based lubricant solution and diamond suspension, 0.05 μm MD-Chem cloth with Al_2O_3 powder based solution, were utilized to obtain scratch-free surfaces with high reflectivity. Samples were then etched in 4.2 g picric

acid + 10 ml acetic acid + 10 ml H_2O + 70 ml ethanol (95%) solution.

Samples were coated with silver paste for SEM observation. The microstructure of AZ31 samples were studied by Scanning Electron Microscopy (SEM) using Secondary Electrons (SE) imaging. Energy Dispersive Spectrometer (EDS) analysis was used to investigate the chemical composition of second phase particles. The energy of the peak position in a spectrum is the critical information used to identify the element, which is formed by characteristic X-rays. In this research, accelerating voltage around 15-20 keV is optimum for AZ31 considering the critical ionization energy for Mg, Al, Mn, Zn elements. More accurate phase analysis was performed by Burker D8 Advanced X-ray diffractometer (XRD).

The average grain size was measured by the ASTM linear intercept method [125]. Clemex image processing was used to obtain grain size distribution and volume fraction of fine grains [126].

5. Experimental Results

This chapter has been divided into three sections. The results from heat treatment of AZ31 are described in section 5.1, microstructure was characterized after different annealing temperatures; section 5.2 describes results from mechanical testing at high temperatures with different strain rates, superplastic behavior was investigated in this section; further grain refinement through both symmetric and asymmetric rolling was explored in the next section, warm rolling results and the corresponding mechanical properties are specified in section 5.3.

5.1 Heat treatment of AZ31

5.1.1 Grain growth

Heat treatment was carried out at temperatures ranging from 300°C to 550°C. Microstructures of AZ31 after different annealing conditions are displayed in figure 5.1, while figure 5.1 (a) shows the as-received material with initial equiaxed microstructure and its average grain size of 11.4 μm. Homogeneous microstructure was observed after annealing below 400°C for 1 hour, which remained almost the same as the as-received material. Inhomogeneous microstructure with a few large grains was observed after annealing at 450°C for 1 hour, which means abnormal grain growth occurred under this condition. After annealing above 500°C for 1 hour, microstructure surface was covered with very big grains, thus rapid grain growth took place.

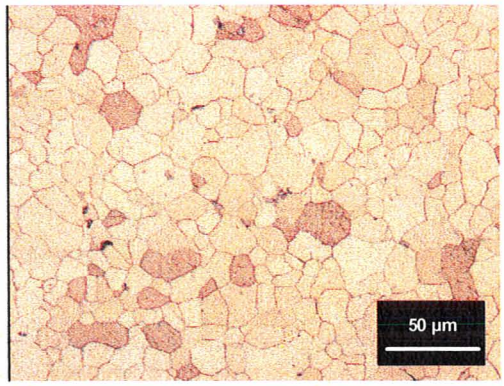

(a) Initial microstructure of AZ31

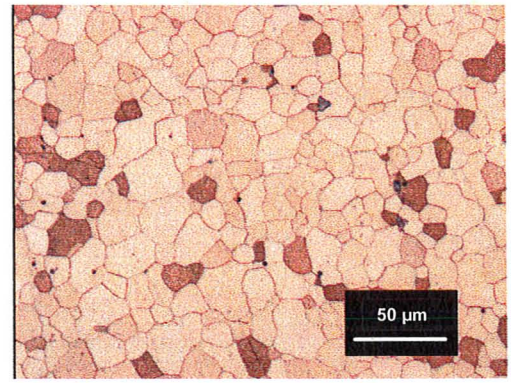

(b) Annealing temperature 400°C

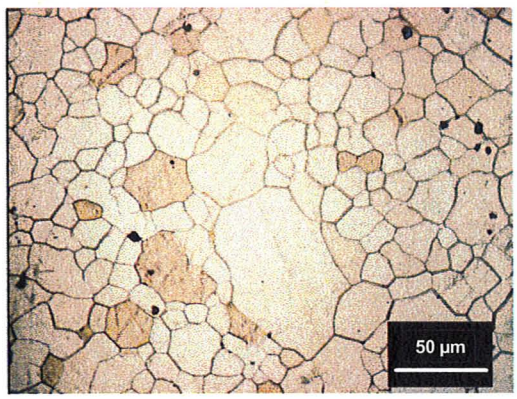

(c) Annealing temperature 450°C

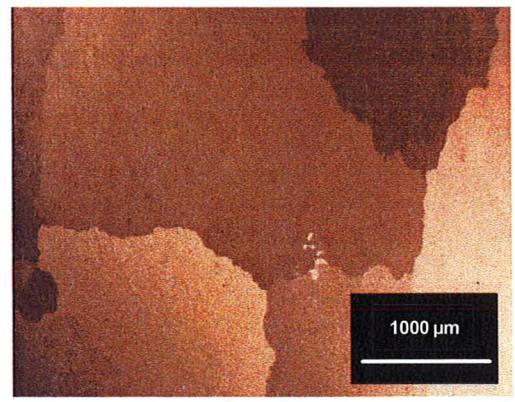

(d) Annealing temperature 500°C

Figure 5.1 Optical micrographs of as-received AZ31 and after different heat treatment.

5.1.2 Second phase particles

Scanning electron microscope was used to characterize second phase particle behavior. Figure 5.2 are the SEM images of AZ31: (a) is the microsctructure after annealing at 400°C for 1 hour, (b) is the microsctructure after annealing at 500°C for 1 hour. Particles were observed both along the grain boundary and within the grain boundary from (a), which revealed the existence of pinning effect. However, no particles are observed along the grain boundary from (b), suggested that those

particles along the grain boundary dissolved at such high temperature. Energy dispersive spectrum (EDS) analysis showed that the chemical composition of the particle along the grain boundary, which was circled in figure 5.2 (a), was Al and Mn (see figure 5.3). Similar results were obtained for other particles either along or within the grain boundaries.

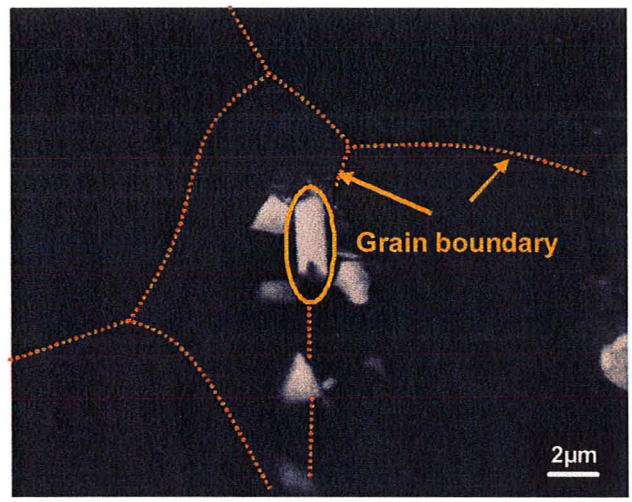

(a) SEM micrograph of AZ31 after annealing at 400°C

(b) SEM micrograph of AZ31 after annealing at 500°C

Figure 5.2 SEM micrographs of AZ31 and after different heat treatment.

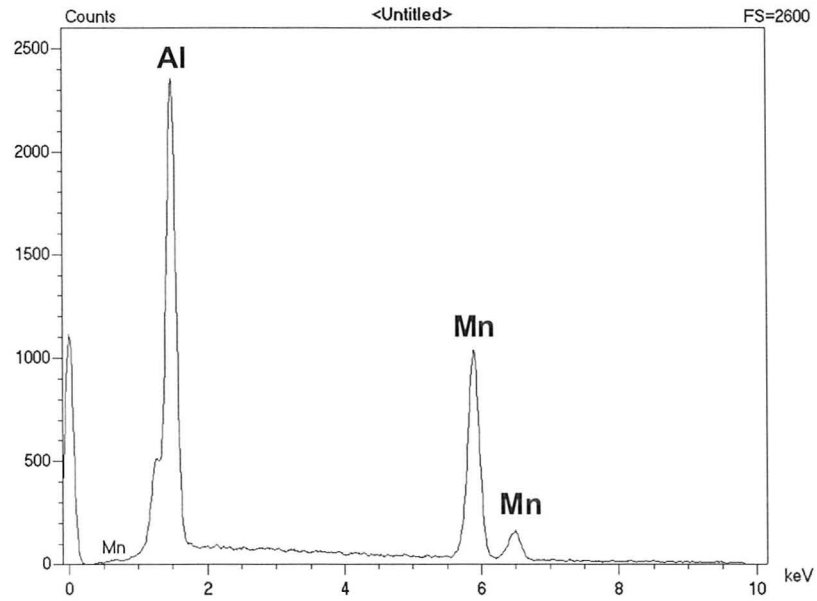

Figure 5.3 Chemical compositions of second phase particles.

5.1.3 X-ray phase analysis

Phase analysis was carried out using X-ray diffraction as presented in figure 5.4. For both samples annealed at (a) 400°C and (b) 500°C for 1 hour, there were two different phases Al_8Mn_5 and $Al_{11}Mn_4$ present. Comparing phase analysis between two cases, the peak value of $Al_{11}Mn_4$ decreased obviously after annealing at 500°C for 1 hour. Thus, second phase particles $Al_{11}Mn_4$ dissolved when annealing temperature increased from 400°C to 500°C.

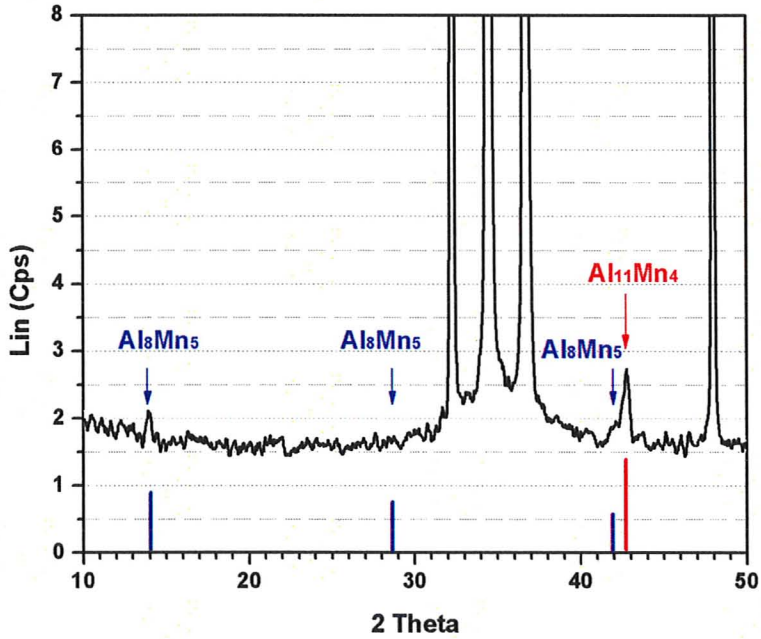

(a) XRD analysis of AZ31 after annealing at 400°C

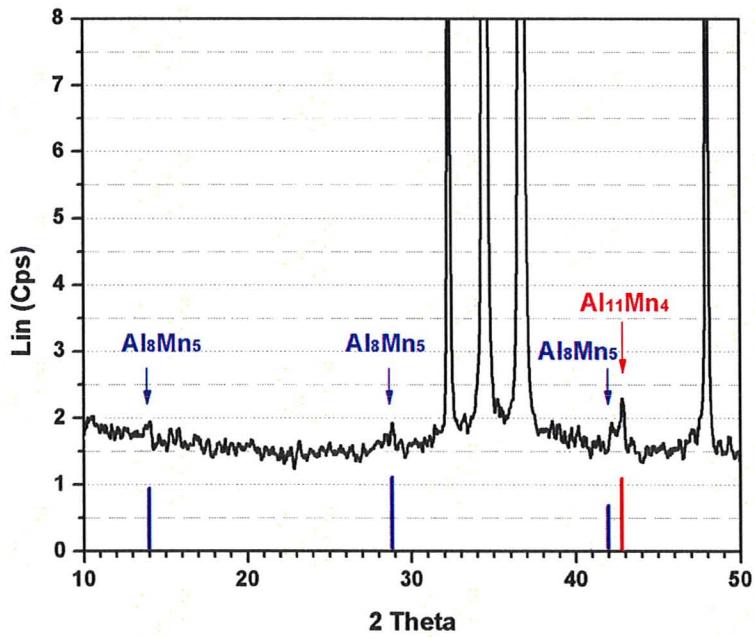

(b) XRD analysis of AZ31 after annealing at 500°C

Figure 5.4 Phase analysis of X-Ray diffraction (XRD) technique.

5.2 Tensile testing of AZ31

As fine grain structure was stable under annealing temperature up to 400°C for 1 hour, the temperature range for tensile tests was set up from 200°C to 400°C, with constant strain rates ranging from 2.7×10^{-4} s^{-1} to 8.8×10^{-3} s^{-1}.

5.2.1 Elongation-to-failure

The elongation-to-failure was measured at different temperatures with strain rates from 2.7×10^{-4} s^{-1} to 8.8×10^{-3} s^{-1}, as shown in Figure 5.5. The elongation-to-failure increased as the temperature increased. At 200°C, the elongation-to-failure value didn't change much when the strain rate value increased. However, at 300°C and 400°C, the elongation-to-failure decreased rapidly after reaching the peak value as the strain rate value increased. The greatest elongation-to-failure value was obtained under the optimum strain rate value of 4.4×10^{-4} s^{-1} at all temperatures, with an elongation of 75% was obtained at 200°C, 226% at 300°C and 339% at 400°C.

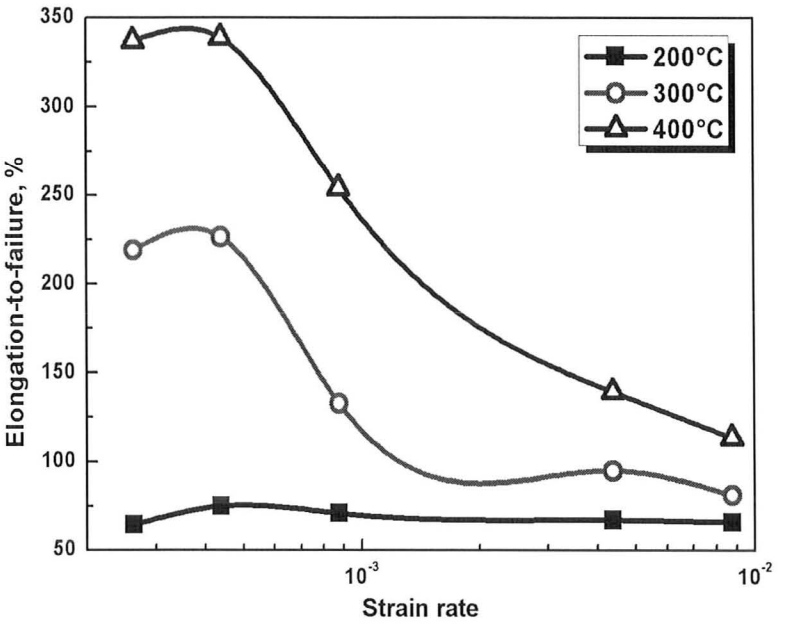

Figure 5.5 Elongation-to-failure of tensile tests at different temperatures as a function of strain rate.

5.2.2 Strain-rate sensitivity

The variation of flow stress of AZ31 was measured after tensile tests at different temperatures as a function of strain rate from 2.7×10^{-4} s^{-1} to 8.8×10^{-3} s^{-1} at a definite true strain value of 0.1, as shown in Figure 5.6. When the temperature increased, the flow stress decreased. The strain-rate-sensitivity m value is the slope of the flow curves according to equation 4.7, as displayed in figure 5.7. The greatest m value was also obtained at the optimum strain rate value of 4.4×10^{-4} s^{-1} at each temperature, 0.36 was obtained at 200°C, 0.57 was obtained at 300°C, and 0.87 was obtained at 400°C.

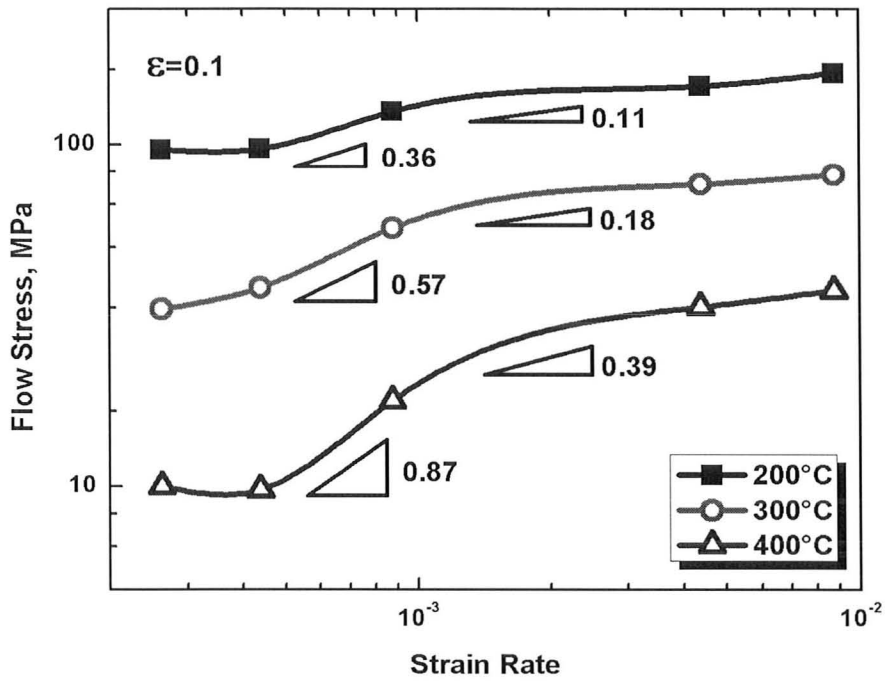

Figure 5.6 True flow stress of tensile tests at different temperatures as a function of strain rate with definite true strain value of 0.1.

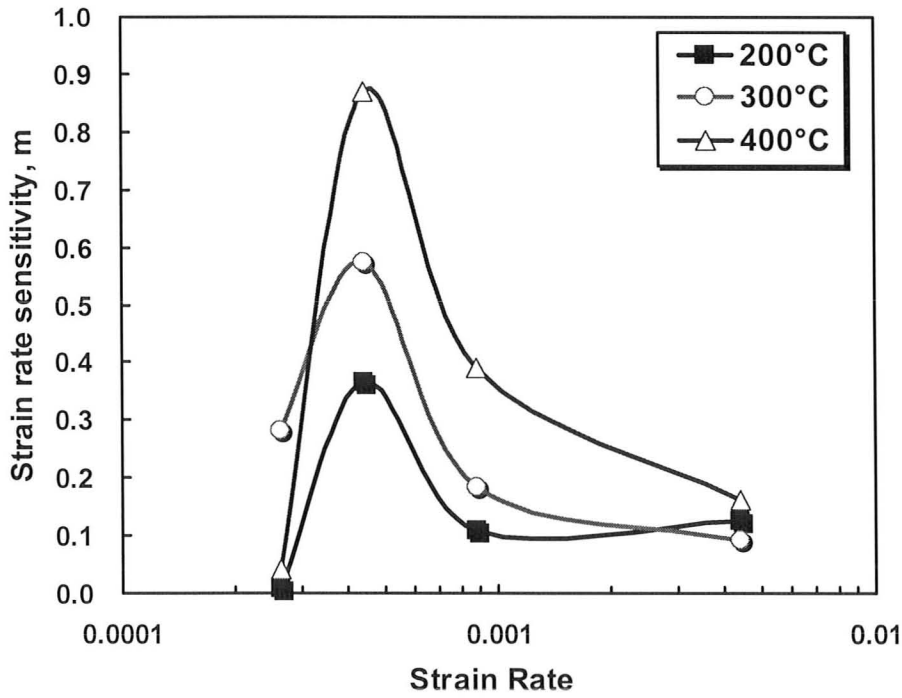

Figure 5.7 Strain-rate-sensitivity m of tensile tests at different temperatures as a function of strain rate.

Load displacement curve of strain rate change (SRC) tests at 200°C are presented in figure 5.8, strain rate jumped from (a) 8.8×10^{-4} s^{-1} to 8.8×10^{-3} s^{-1} and (b) 2.7×10^{-4} s^{-1} to 8.8×10^{-4} s^{-1} respectively. From test (a), strain rate value jumped from 8.8×10^{-4} s^{-1} to 8.8×10^{-3} s^{-1} before the maximum load point and strain-rate-sensitivity value was calculated as 0.08, then jumped from 8.8×10^{-3} s^{-1} back to 8.8×10^{-4} s^{-1} after the maximum load point and strain-rate-sensitivity value was calculated as 0.107 here. Strain-rate-sensitivity value was smaller before maximum loading point which revealed the possibility of microstructure effect. Strain-rate-sensitivity value was calculated as 0.101 from curve (b).This value was very close to *m* value obtained from figure 5.7 under the same strain rate, which was 0.108. Thus, *m* value from SRC tests before maximum loading was very close to the value directly obtained from the slope of true flow stress curve in figure 5.6 at 200°C.

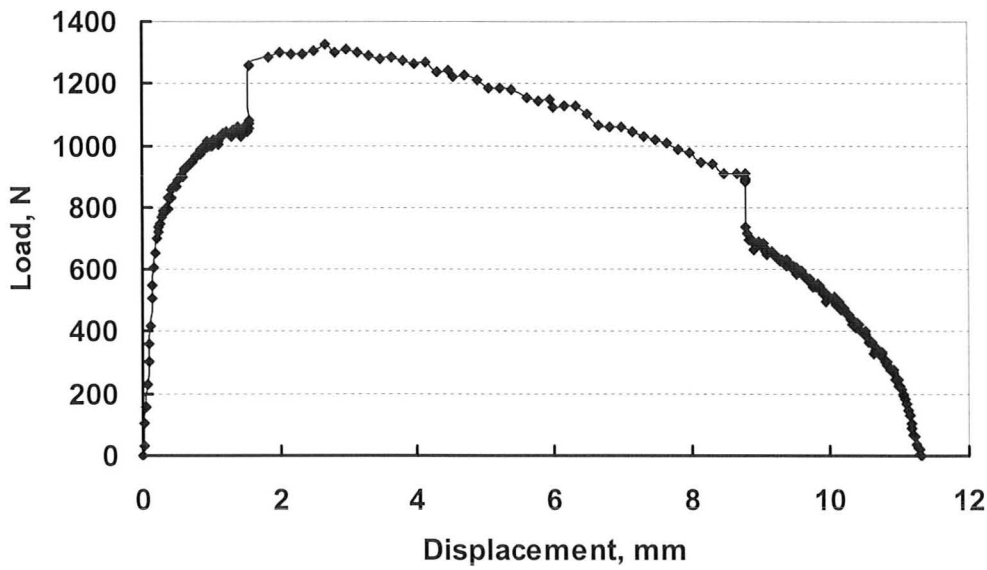

(a) Strain rate jumped from 8.8×10^{-4} s^{-1} to 8.8×10^{-3} s^{-1}

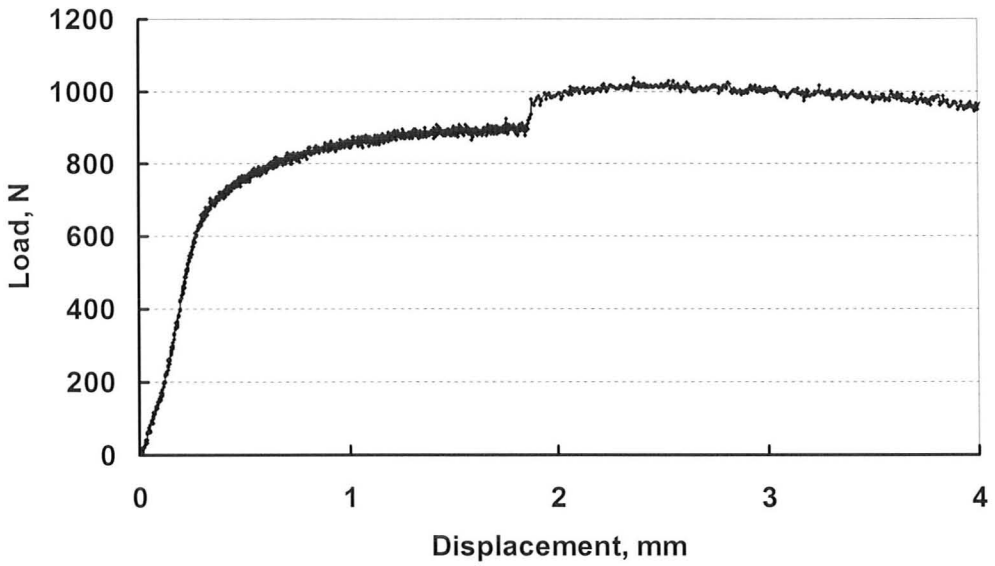

(a) Strain rate jumped from 2.7×10^{-4} s^{-1} to 8.8×10^{-4} s^{-1}

Figure 5.8 Load-displacement curves of SRC tests of AZ31 at 200°C.

5.2.3 True stress-strain curve

True stress-strain curve in local area at different temperatures from 200°C to 400°C with strain rate values from 4.4×10^{-4} s^{-1} to 8.8×10^{-3} s^{-1} was calculated using method from chapter 4.5, as presented in figure 5.9. At 200°C, true flow stress decreased upon loading after ultimate tensile strength (UTS) point at low strain rate of 4.4×10^{-4} s^{-1}, while it increased after UTS point at higher strain rate. At 300°C, true flow stress decreased upon loading after UTS point, then followed by increasing again at low strain rate of 4.4×10^{-4} s^{-1}. At higher strain rate, true flow stress decreased upon loading after UTS point. At 400°C, all true flow stress decreased after UTS point which revealed almost uniform deformation at such high temperature.

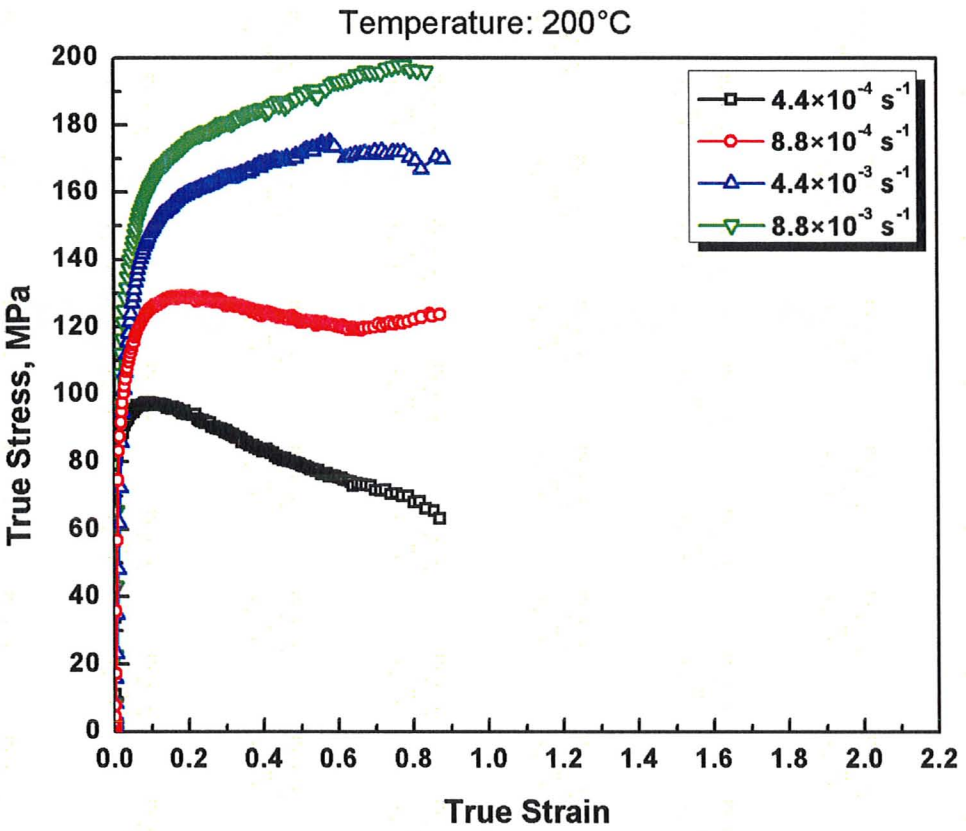
Temperature: 200°C
True Stress, MPa
True Strain
4.4×10-4 s-1
8.8×10-4 s-1
4.4×10-3 s-1
8.8×10-3 s-1
0
20
40
60
80
100
120
140
160
180
200
0.0
0.2
0.4
0.6
0.8
1.0
1.2
1.4
1.6
1.8
2.0
2.2

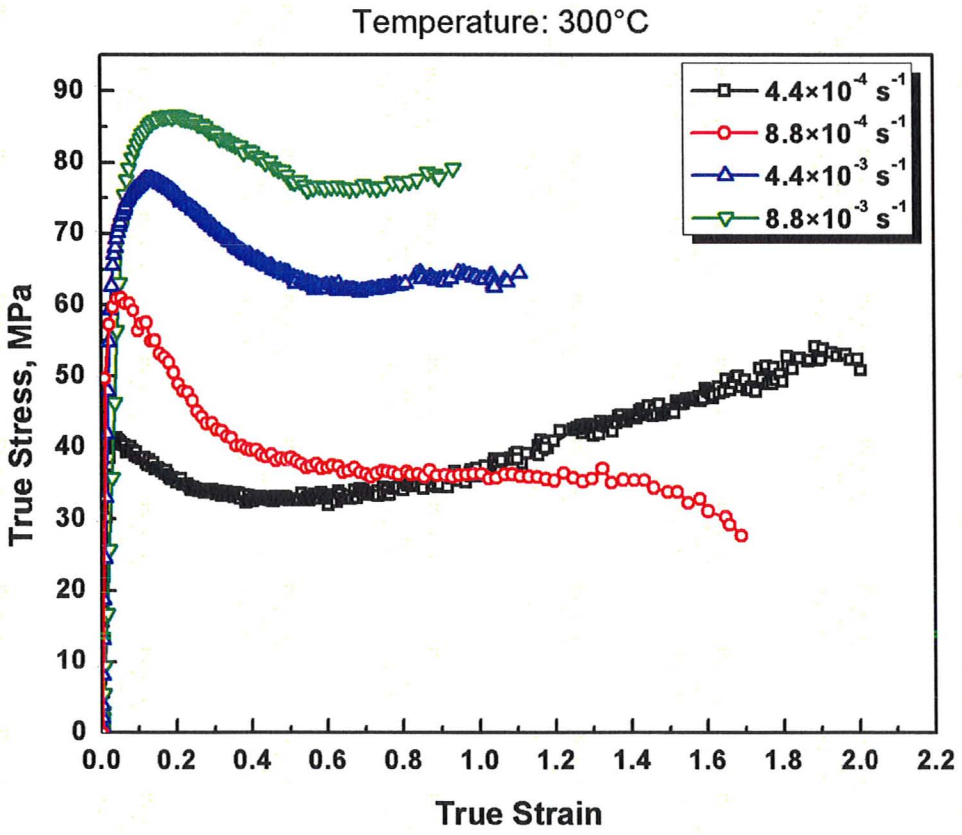
Temperature: 300°C
True Stress, MPa
True Strain
4.4×10-4 s-1
8.8×10-4 s-1
4.4×10-3 s-1
8.8×10-3 s-1
0
10
20
30
40
50
60
70
80
90
0.0
0.2
0.4
0.6
0.8
1.0
1.2
1.4
1.6
1.8
2.0
2.2

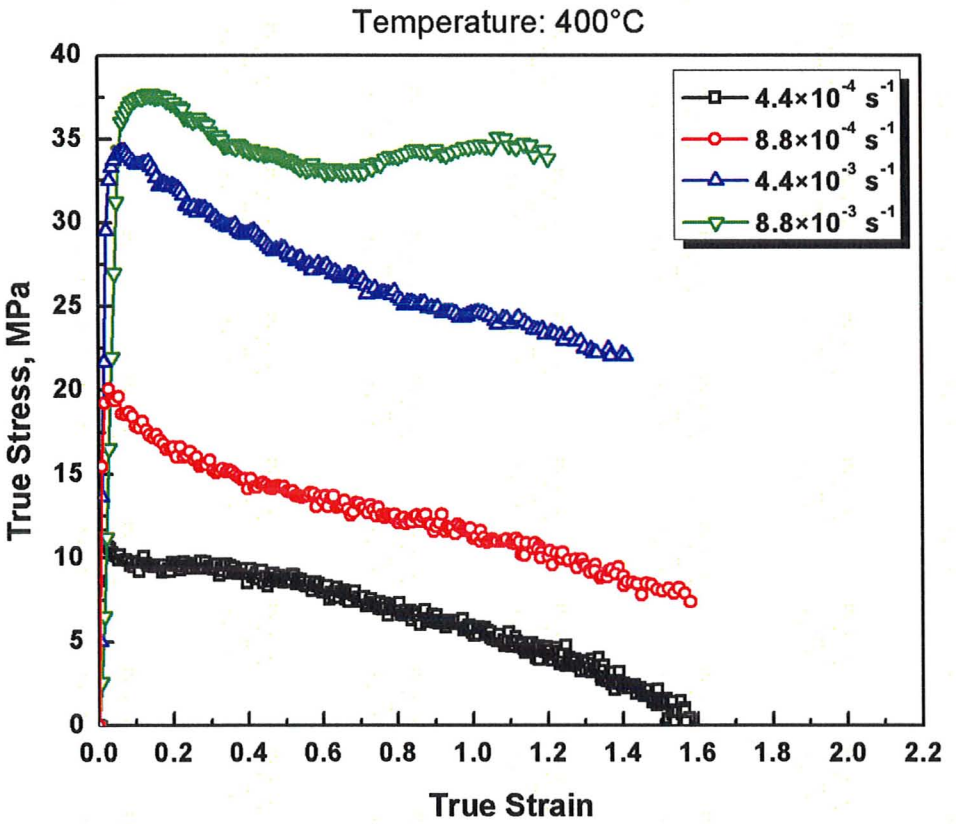

Figure 5.9 Local true stress-strain curves of tensile tests at high temperatures ranging from 200°C to 400°C with strain rates ranging from 4.4×10^{-4} s^{-1} to 8.8×10^{-3} s^{-1}.

5.2.4 Fracture surface observation

Fracture surface was observed after tensile tests under different conditions. At 200°C, no cavities formed along the grain boundary and elongation-to-failure values were relatively low; while at 300°C and 400°C, similar microstructure near fracture tip was observed under low strain rate of 4.4×10^{-4} s^{-1}, greater elongation-to-failure and strain-rate-sensitivity value were also obtained.

Figure 5.10 shows the SEM micrographs of fracture surface after tensile tests at 300°C with constant strain rate of 4.4×10^{-4} s^{-1}. Elongation-to-failure of 226% and

strain-rate-sensitivity of 0.57 was obtained here. The fracture surface area showed regions of refined (recrystallized) grains exhibiting grain boundary failure along with regions of ductile tearing around cleavage zones, as pointed out by 'a' and 'b' character respectively in (a). Figure 5.10 (d) depicted different cracking modes on fracture surface corresponding to area 'a' and 'b' respectively. The intergranular cracking was occurred along those integrated fine grain boundaries, accompanied by the transgranular cracking within grain boundaries as specified in (d).

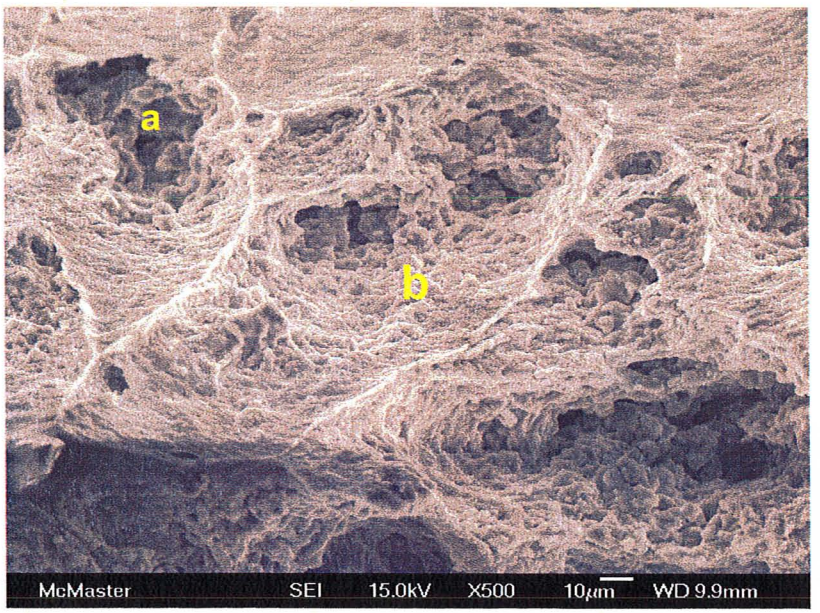

(a) Fracture surface with full of area 'a' and area 'b'

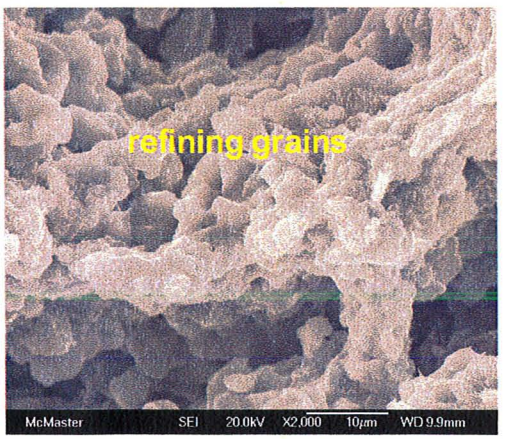

(b) Integrated grains in 'a'

(c) Tearing edges in 'b'

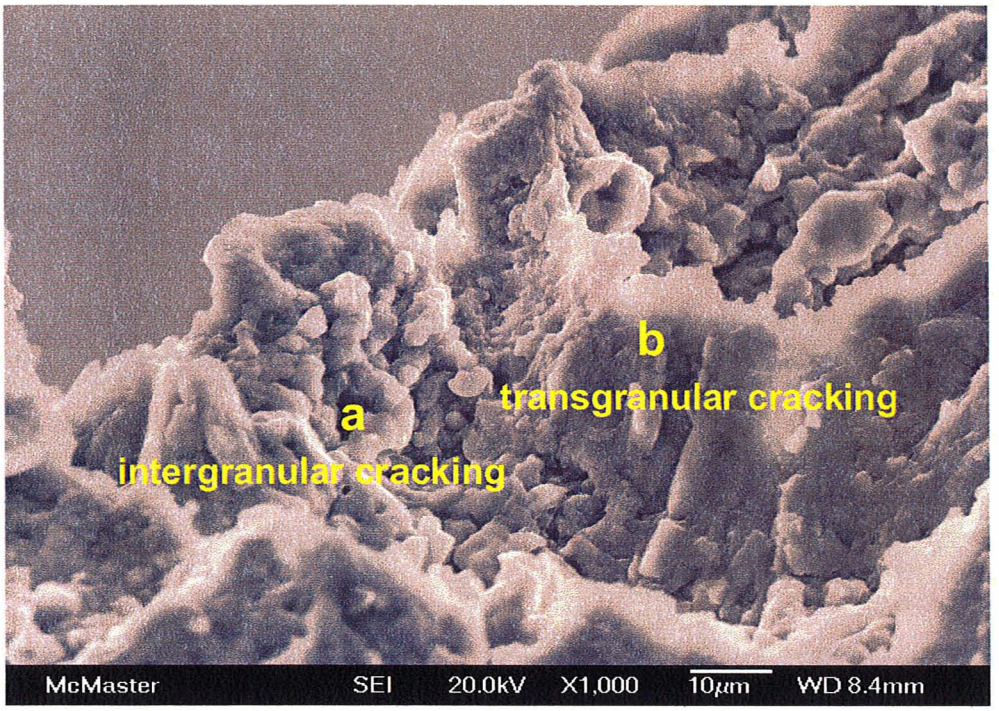

(d) Different cracking modes on the fracture surface

Figure 5.10 SEM micrographs of fracture surface after superplastic deformation at 300°C with constant strain rate of 4.4×10-4 s^{-1}.

Surface microstructure of the same sample deformed at such condition was also observed after etching, as displayed in Figure 5.11. Variety of cavitations formed along the grain boundaries near fracture tip as shown in (a). Wedge cracking was observed at triple grain boundary in (b).

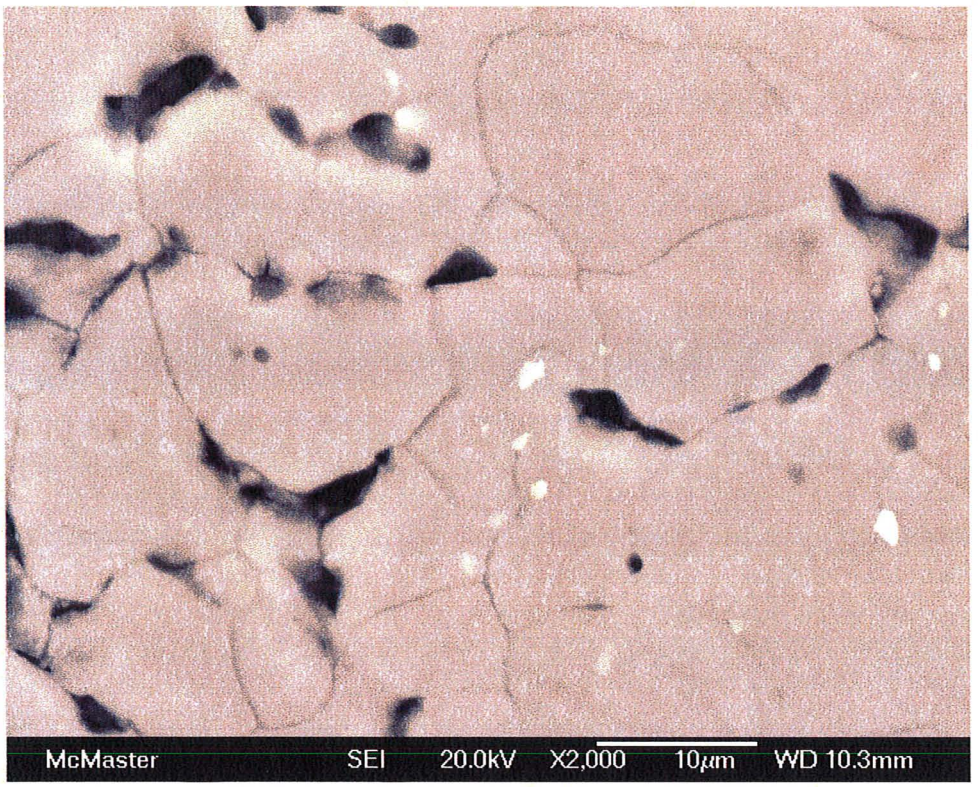

(a) Cavities formed along grain boundaries

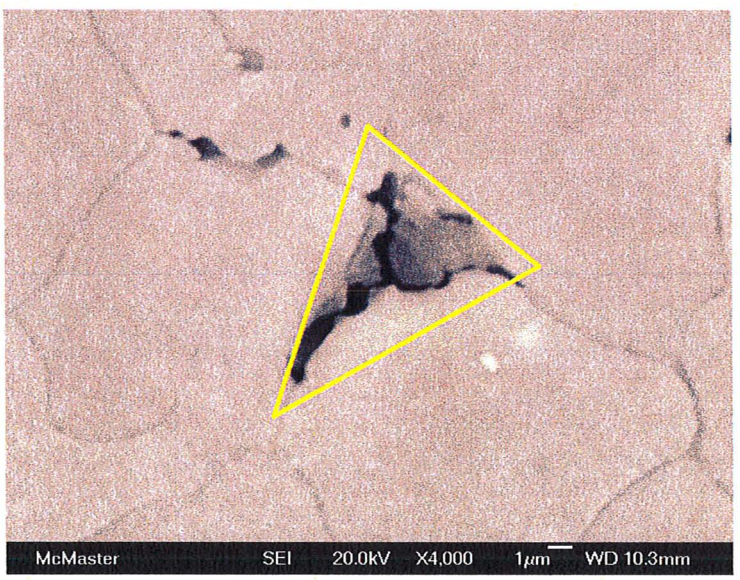

(a) Wedge cracking at triple grain boundary

Figure 5.11 SEM micrographs of etched surface microstructure after superplastic deformation at 300°C with constant strain rate of 4.4×10-4 s^{-1}.

5.2.5 DRX and grain growth mechanism

Optical microstructures near the fracture tip and grain size distribution after tensile tests at 200°C and 300°C with constant strain rate ranging from 4.4×10^{-4} s^{-1} to 8.8×10^{-3} s^{-1} are presented in figure 5.12. The tensile axis was the parallel direction for optical microstructure. It is important to measure the volume fraction of fine grains due to the inhomogeneous grain size distribution resulting from incomplete DRX. In this study, grains with less than 10 μm average grain size were defined as fine grains. Volume fraction of fine grains V_f near the fracture tip was measured using the following expression:

$$V_f = \frac{\sum A_f}{\sum A_t} \tag{5.1}$$

where A_f is the total area of fine grains, A_t is the total area on the microstructure image. At least 5000 grains were selected for the measurement to improve reliability.

Compared with the as-extruded AZ31, for which V_f was 22%, the volume fraction of fine grains increased after tensile tests at 200°C and 300°C, which proved the occurrence of DRX mechanism during high temperature deformation.

At 200°C, an inhomogeneous microstructure was observed. Some elongated grains were observed near fracture tip at high strain rate of 4.4×10^{-3} s^{-1} and 8.8×10^{-3} s^{-1}. Recrystallized fine grains first formed along the grain boundaries. Those newly formed fine grains covered more and more area of the surface as the strain rate decreased, starting to consume the original microstructure. The volume fraction of fine grains near the fracture tip decreased from 69% to 32% as the strain rate increased from 4.4×10^{-4} s^{-1} to 8.8×10^{-3} s^{-1}.

At 300°C, no elongated grains were observed near the fracture tip. Much more area was consumed by newly formed recrystallized fine grains at higher strain rate values. The microstructure became quite homogeneous at low strain of 4.4×10^{-3} s^{-1}. The volume fraction of fine grains were calculated to increase from 31% to 38% as the strain rate increased from 4.4×10^{-4} s^{-1} to 8.8×10^{-3} s^{-1}.

(a)

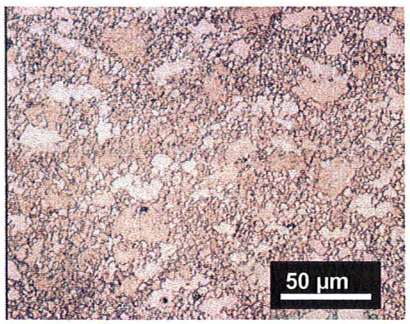

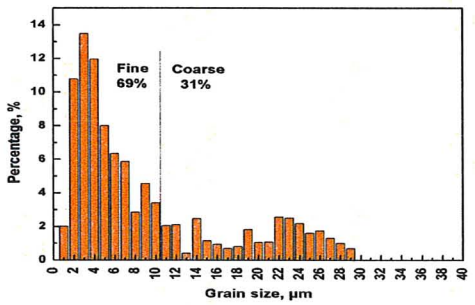

(b)

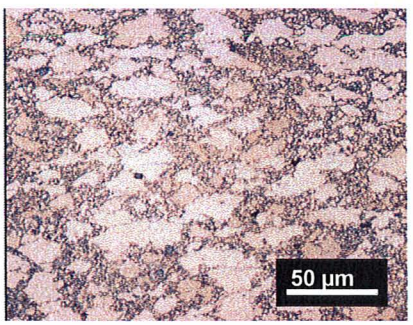

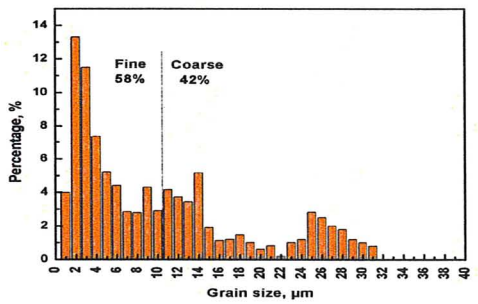

(c)

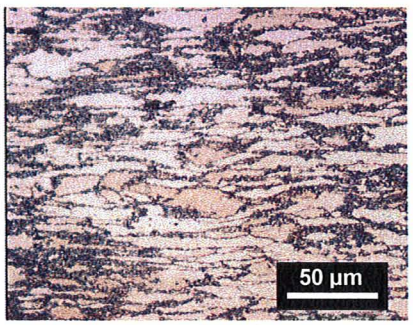

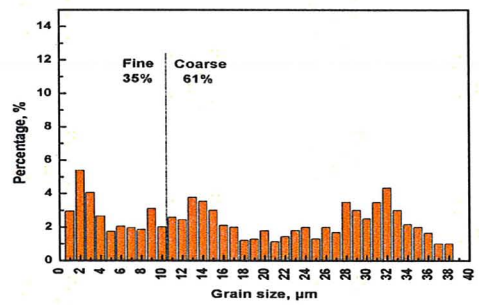

(d)

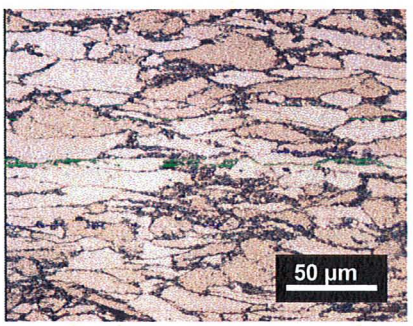

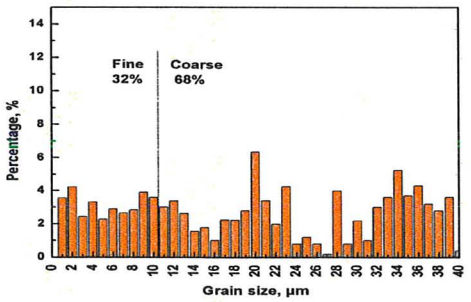

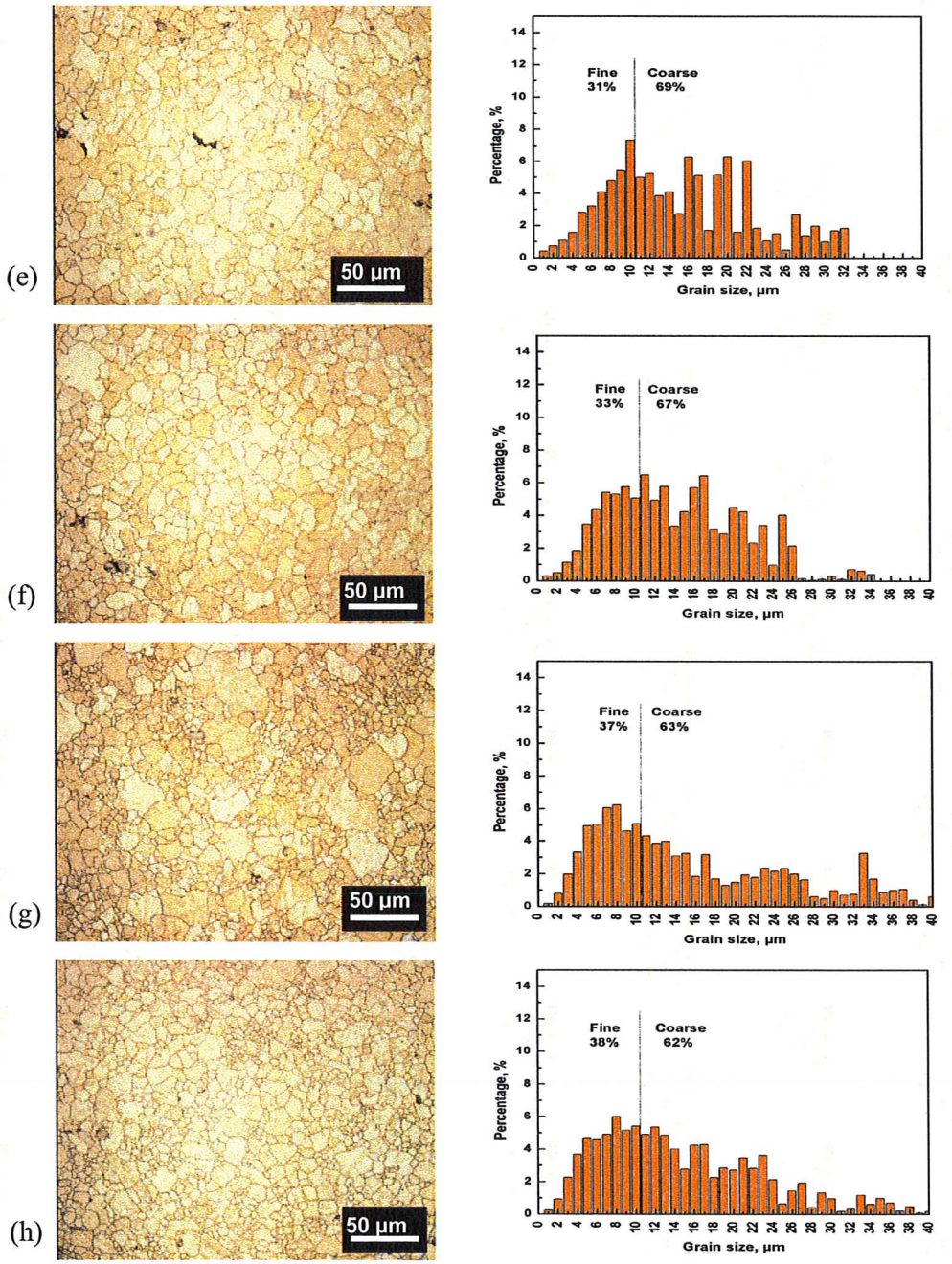

Figure 5.12 Optical microstructure near fracture tip and the corresponding grain size distribution at 200°C with different constant strain rate (a) 4.4×10^{-4} s^{-1} (b) 8.8×10^{-4} s^{-1} (c) 4.4×10^{-3} s^{-1} (d) 8.8×10^{-3} s^{-1} and 300°C with different constant strain rate (e) 4.4×10^{-4} s^{-1} (f) 8.8×10^{-4} s^{-1} (g) 4.4×10^{-3} s^{-1} (h) 8.8×10^{-3} s^{-1}. The tensile axis was in the horizontal direction.

Average grain size was also measured near the fracture tip at both temperatures with the same strain rate range, as displayed in figure 5.13. At 200°C, average grain size increased as the strain rate increased, while at 300°C, average grain size decreased as the strain rate increased. Compared with the average grain size of as-received AZ31, 11.4 μm, the average grain size of AZ31 near fracture tip decreased after tensile tests at both temperatures, which also proved the existence of DRX during the deformation.

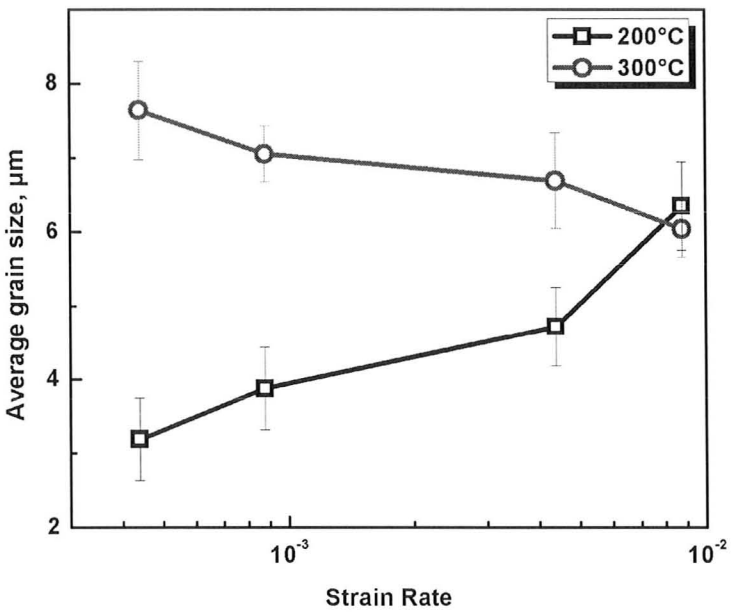

Figure 5.13 Average grain size near fracture tip as a function of strain rate.

5.3 Warm rolling testing of AZ31

Different rolling schedules were used to achieve total reduction of around 40% at 200°C and 300°C, as listed in table 5.1.

Table 5.1 Different rolling schedules of AZ31

Schedule No.	Rolling temperature	Rolling type	Total passes	Reduction per pass
1	200°C	Symmetric	8	6%
2	200°C	Asymmetric	8	6%
3	300°C	Symmetric	4	12%
4	300°C	Asymmetric	3	15%

Sample surfaces after rolling are all presented in figure 5.14. At 200°C rolling temperature, slight edge cracking was observed, especially for asymmetric rolling. However, sample surfaces turned out to be pretty smooth after 300°C for both symmetric and asymmetric rolling, with no edge cracking was observed.

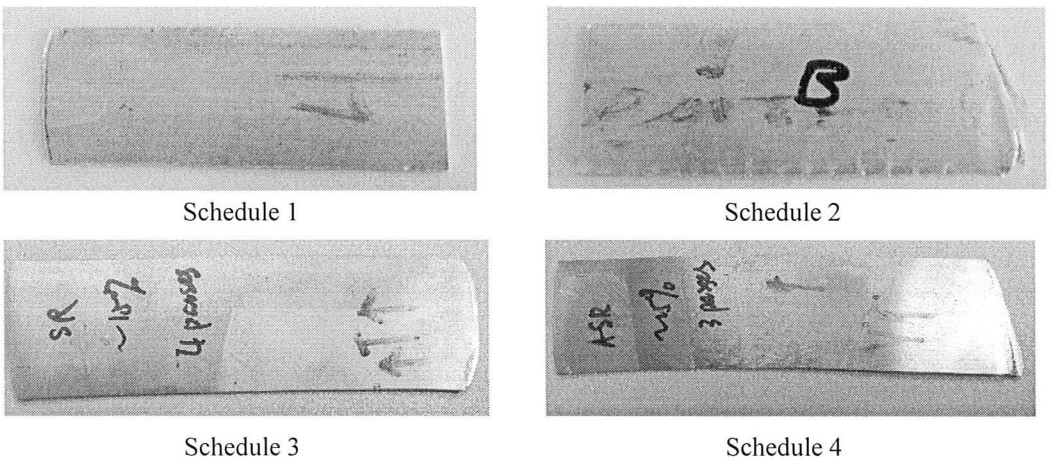

Schedule 1 Schedule 2

Schedule 3 Schedule 4

Figure 5.14 Sample surfaces after different rolling schedules

5.3.1 Optical Microstructure

Optical microstructure was observed after different rolling procedures and after

annealing at 200°C for 1 hour. Figure 5.15 shows the microstructures after 200°C rolling and 200°C annealing, while figure 5.16 shows the microstructures after 300°C rolling and 200°C annealing. The vertical direction is the rolling direction and horizontal direction is the transverse direction.

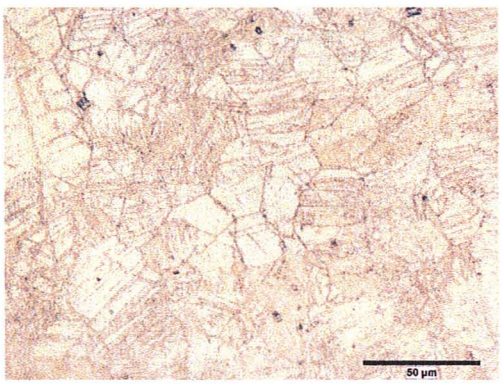

(a) Symmetric rolling

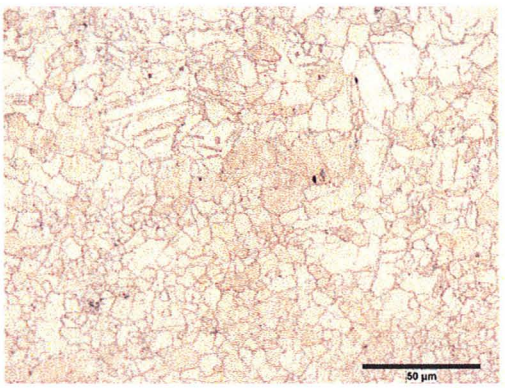

(b) Symmetric rolling + annealing

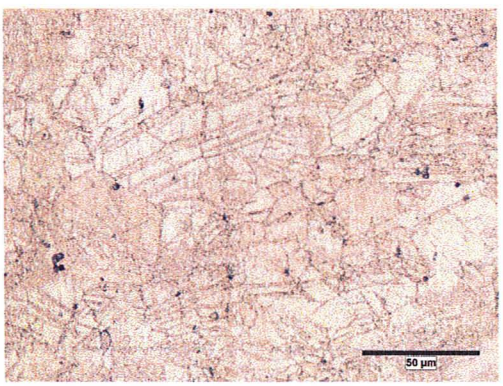

(c) Asymmetric rolling

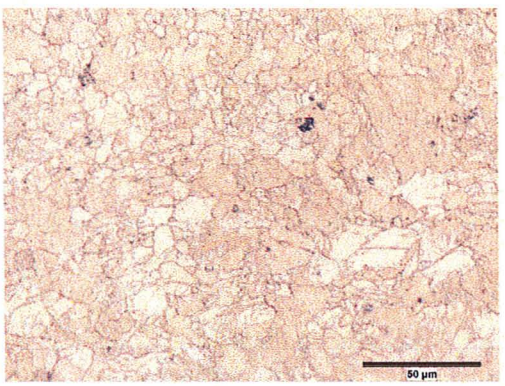

(d) Asymmetric rolling + annealing

Figure 5.15 Optical microstructures after warm rolling at 200°C and corresponding heat treatment.

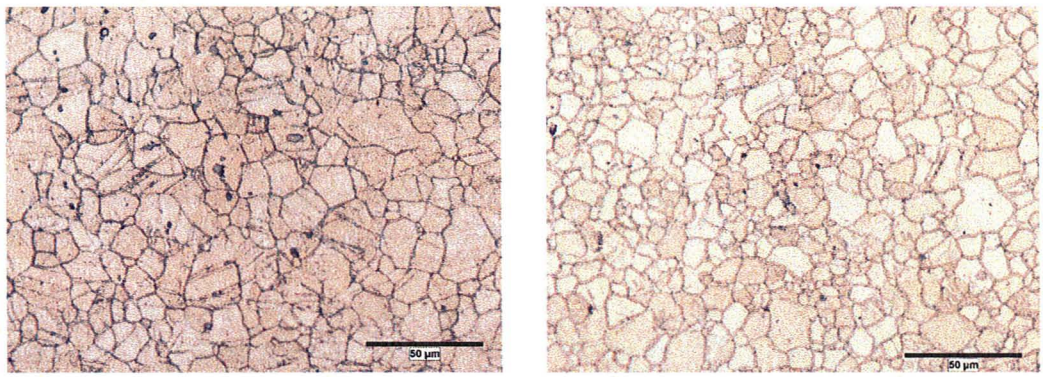

(a) Symmetric rolling (b) Symmetric rolling + annealing

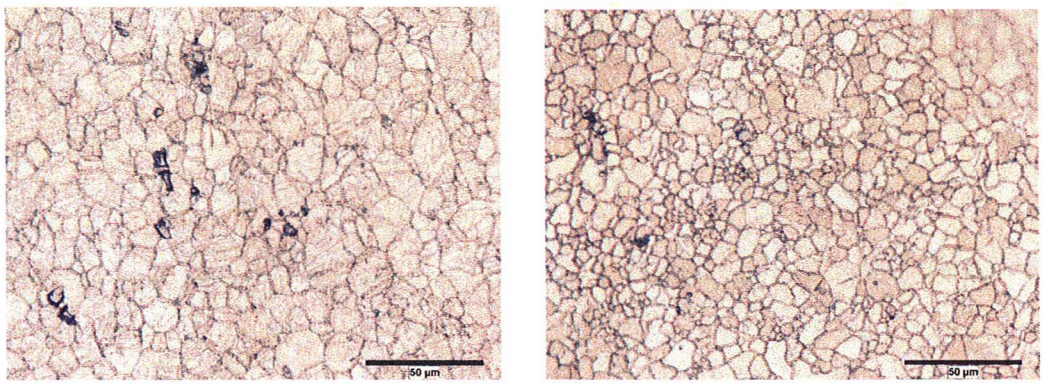

(c) Asymmetric rolling (d) Asymmetric rolling + annealing

Figure 5.16 Optical microstructures of AZ31 after warm rolling at 300°C and corresponding heat treatment.

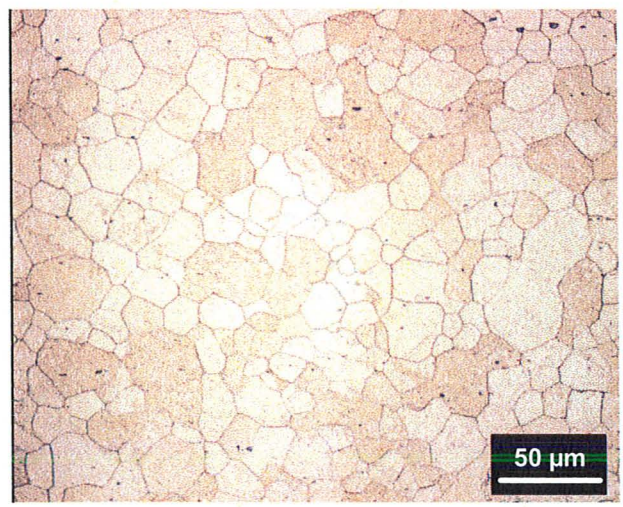

Figure 5.17 Optical microstructure of as-received AZ31 for warm rolling tests.

For 200°C, microstructure was seriously deformed after both symmetric and asymmetric rolling. Some twinning was observed accompanied by a few newly formed fine grains due to DRX during the deformation. The microstructure was quite inhomogeneous. Much more fine grains formed after annealing to cover the original microstructure due to the static recrystallization during the annealing. For 300°C, the microstructure was still seriously deformed after both symmetric and asymmetric rolling covered with twinning. However, many more newly formed fine grains consumed the original microstructure due to DRX during the deformation as compared with the 200°C case. After heat treatment, the deformed microstructure was almost replaced by fine grains due to static recrystallization during annealing. The microstructure turned out to be quite homogeneous for both symmetric and asymmetric cases. Compared with the microstructure of as-received AZ31 for rolling tests as shown in figure 5.17, warm rolling was effective for grain refinement.

5.3.2 Texture analysis

Pole figures for the basal plane (0002) were plotted to analyze texture after rolling and following annealing procedures, which are presented in figure 5.18. The vertical direction on the pole figure is the rolling direction, and the horizontal direction is the transverse direction.

However, compare to the pole figure for as-received material, as shown in figure 5.19, the (0002) intensity for as-received AZ31 was 8, the texture became stronger after rolling procedures and it didn't improve much after annealing.

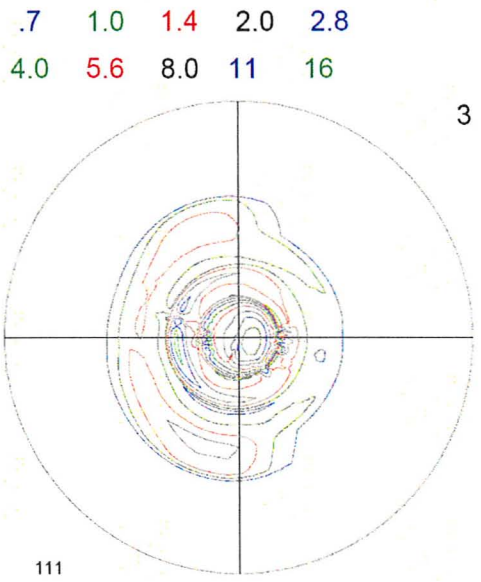

(a) 200°C asymmetric rolling

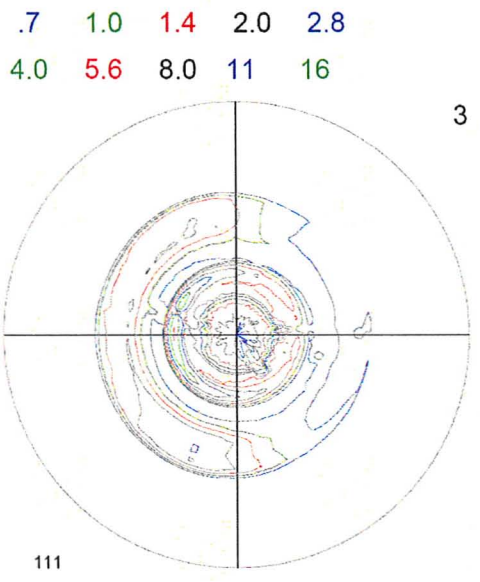

(b) 200°C asymmetric rolling + annealing

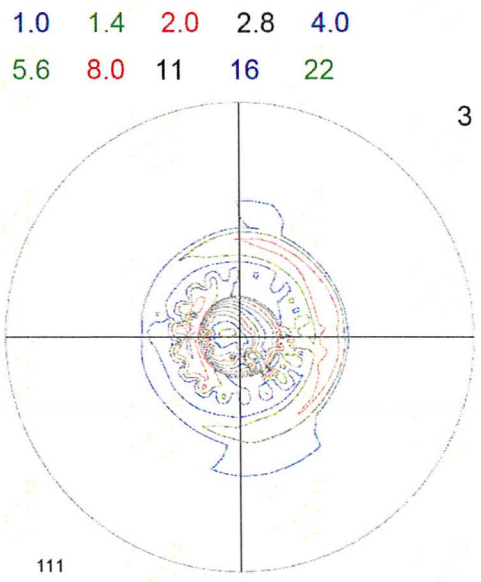

(c) 200°C symmetric rolling

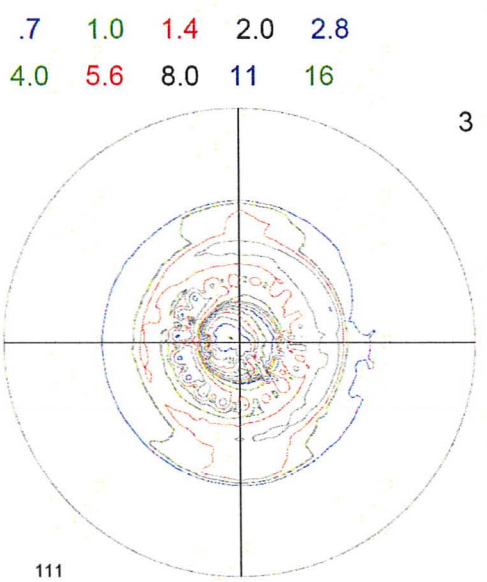

(d) 200°C symmetric rolling + annealing

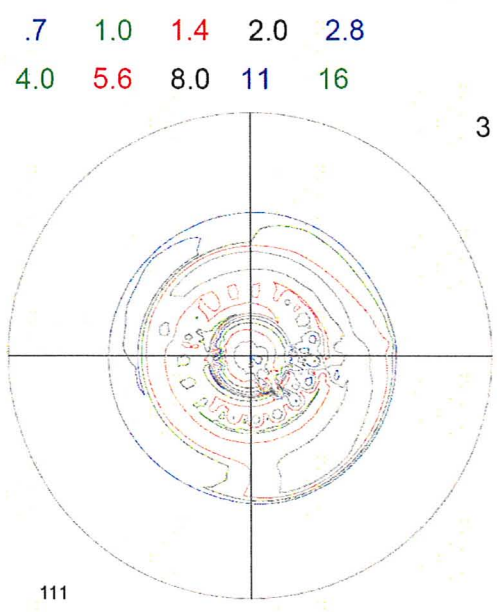

(e) 300°C asymmetric rolling

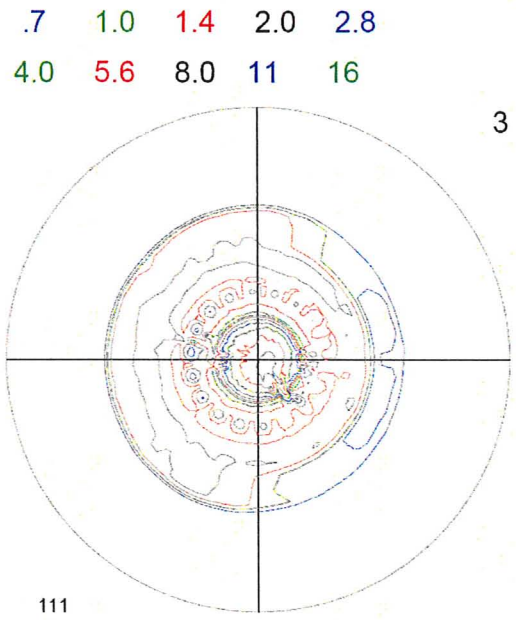

(f) 300°C asymmetric rolling + annealing

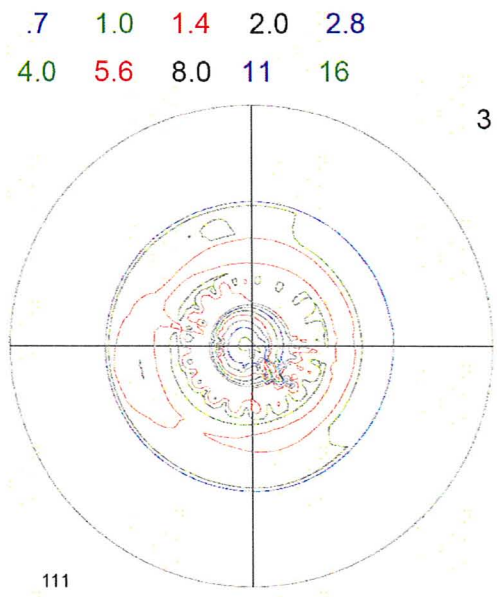

(g) 300°C symmetric rolling

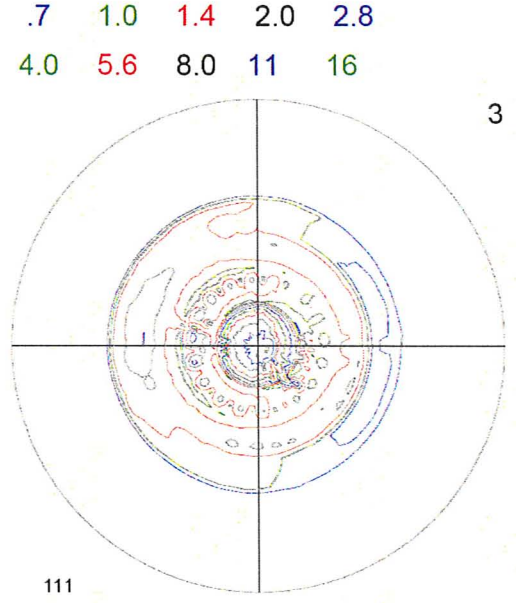

(h) 300°C symmetric rolling + annealing

Figure 5.18 Pole figures of AZ31 after different rolling schedules plus annealing.

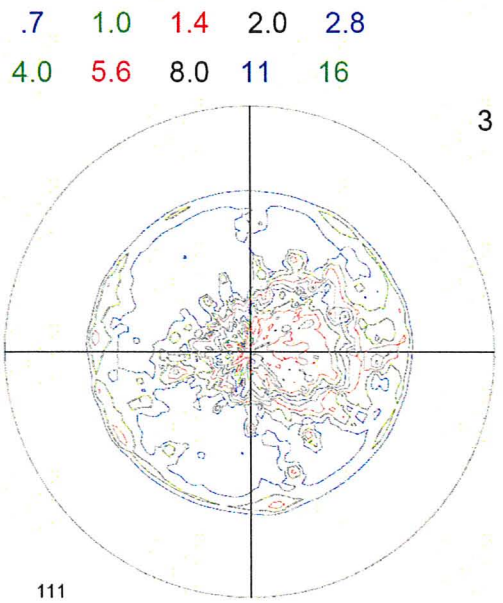

Figure 5.19 Pole figure of as-received AZ31 for warm rolling tests.

5.3.3 Mechanical testing

Homogeneous fine structure was obtained after 300°C rolling followed by 200°C annealing as discussed in Chapter 5.3.1. Mechanical testing was carried out under this condition for both symmetric and asymmetric rolling specimens. Tensile tests were performed at 200°C with a low strain rate value of 4.4×10^{-4} s^{-1} and a high strain rate value of 8.8×10^{-3} s^{-1}. All the tests were performed with the tensile axis parallel to the rolling direction. True stress-strain curves for low strain rate and high strain rate were displayed in figure 5.20 and figure 5.21 respectively. Symmetric specimen was specified by black symbols, while asymmetric specimen was the red one.

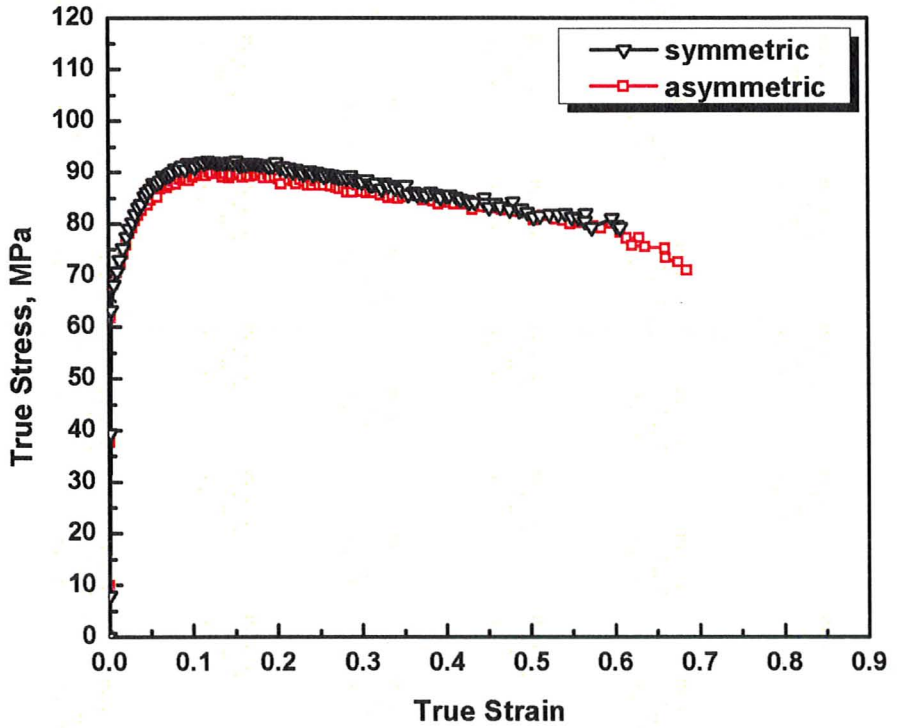

Figure 5.20 True stress-strain curve for tensile test at 200°C with low strain rate value of 4.4×10^{-4} s^{-1}.

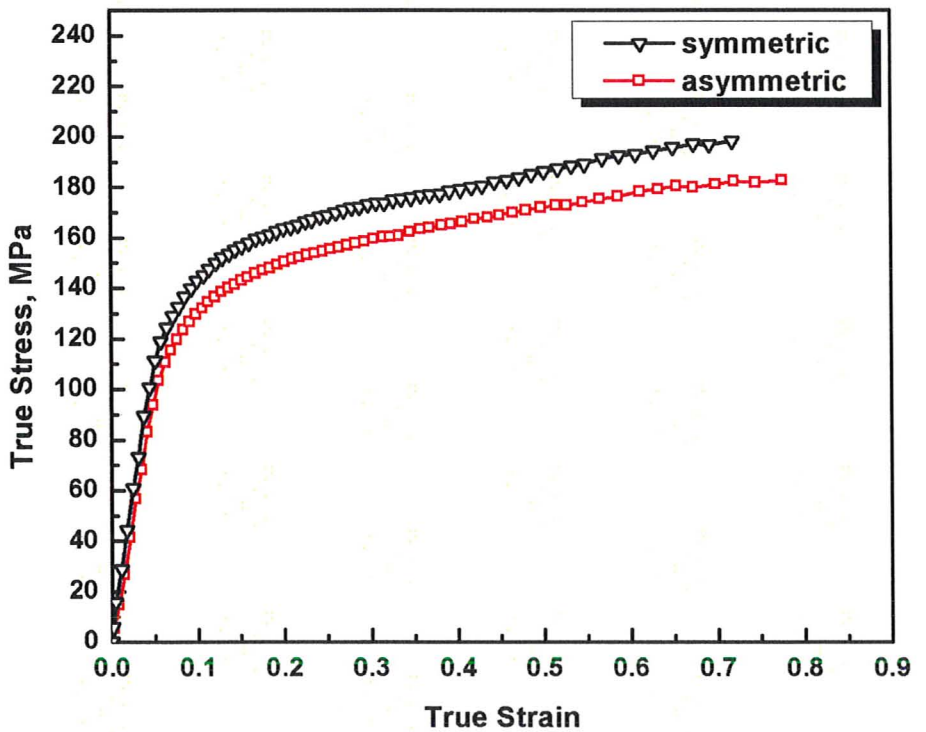

Figure 5.21 True stress-strain curve for tensile test at 200°C with high strain rate value of 8.8×10^{-3} s^{-1}.

Along with yield strength (YS), ultimate tensile strength (UTS), elongation-to-failure (%El) and true strain at fracture ε_f are also important parameters to evaluate the mechanical properties. The latter is defined as:

$$\varepsilon_f = \ln\left(\frac{A_0}{A_f}\right) \tag{5.2}$$

where A_0 is the original cross-sectional area of tensile specimens, A_f is the cross-sectional area at the point of fracture. The initial thickness for all tensile specimens was 0.86 mm with 6 mm width in gauge section. Mechanical properties after tensile tests are listed in table 5.2. For both strain rates, asymmetric samples had slightly higher ductility and fracture strain ε_f values, while symmetric samples had slightly higher UTS and YS values.

Table 5.2 Mechanical properties of AZ31 after 200°C tensile tests.

No.	Strain rate (s^{-1})	Rolling Type	UTS (MPa)	YS (MPa)	%El	ε_f
1	4.4×10^{-4}	Asymmetric	84	68	60.49	1.18
2	4.4×10^{-4}	Symmetric	86	70	56.54	1.06
3	8.8×10^{-3}	Asymmetric	127	96	60.47	1.24
4	8.8×10^{-3}	Symmetric	139	104	60.36	1.09

6. Discussion

This chapter contains three sections of analysis and summary from the experimental data in chapter 5. Chapter 6.1 will discuss microstructure characterization of AZ31 after different heat treatment results from chapter 5.1. Chapter 6.2 will present a summary of superplastic behavior and corresponding microstructure evolution from high temperature tensile tests results described in chapter 5.2. Chapter 6.3 will reveal the further grain refinement of rolling and its effect on mechanical properties achieved from chapter 5.3.

6.1 Microstructure characterization of AZ31

Microstructure characterized in chapter 5.1 after different heat treatment revealed that stable microstructure was obtained after annealing up to 400°C, abnormal grain growth took place after annealing at 450°C and rapid grain growth was observed after annealing at 500°C. Average grain size of AZ31 after different heat treatment was measured by linear intercept method as listed in Table 6.1. Even though the average grain size was still small after annealing at 450°C for 1 hour (14.18 μm), abnormal grain growth was observed here. While after annealing at 500°C for 1 hour, the average grain size increased to ~ 3mm.

Table 6.1 Average grain size after different heat treatment.

Sample No.	Heat treatment temperature	Average Grain Size
1	RT (as-received)	11.40 μm
2	300°C	11.62 μm
3	350°C	11.89 μm
4	400°C	12.58 μm
5	450°C	14.18 μm
6	500°C	2891 μm
7	550°C	2993 μm

Quantification of the volume fraction of different phases is presented in figure 6.1. The volume fraction of $Al_{11}Mn_4$ phase decreased at 500°C compared with the amount at 400°C, while the volume fraction of Al_8Mn_5 phase increased at 500°C. Thus, the new phase Al_8Mn_5 formed while the other phase $Al_{11}Mn_4$ dissolved after annealing at 500°C for 1 hour. This also matched well with the equilibrium phase diagram for Mg+3.03%Al+0.97%Zn+0.31%Mn as shown in figure 6.2. The equilibrium structure at 400°C is ($Mg+Al_{11}Mn_4+Al_8Mn_5$) which had the same results from X-Ray Diffraction analysis. At 500°C, the equilibrium structure is ($Mg+Al_8Mn_5$). However, there was still some $Al_{11}Mn_4$ phase from XRD results, which was due to the possibility of less annealing time or the effect of impurities in AZ31. From SEM images of second phase particles obtained in chapter 5.1.3, particles were observed both along the grain boundary after annealing at 400°C which showed the possibility

of pinning effect, while this phenomenon disappeared when annealing temperature increased to 500°C.

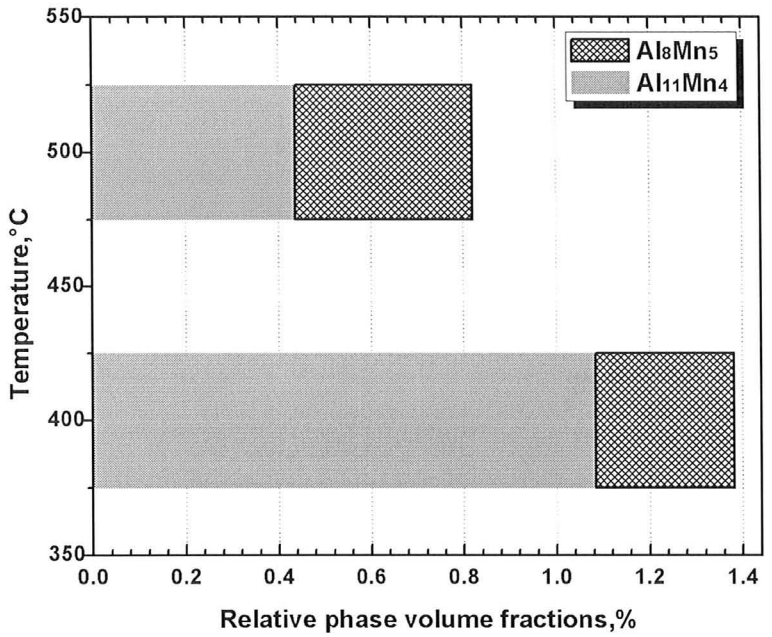

Figure 6.1 Volume fractions of different phases after annealing at 400°C and 500°C.

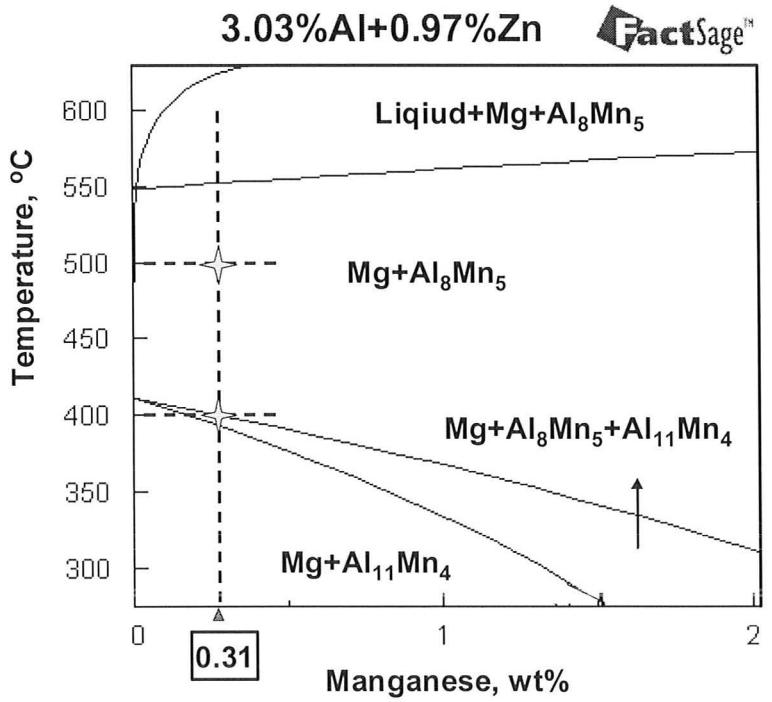

Figure 6.2 Equilibrium phase diagram of (Mg+3.03%Al+0.97%Zn) varied with Mn.

In conclusion, fine grain microstructure was obtained after annealing at 400°C, two phases ($Al_{11}Mn_4$ and Al_8Mn_5) existed, and the pinning effect of second phase particles was observed using SEM. Abnormal grain growth took place after annealing at 450°C while rapid grain growth was observed after annealing at 500°C, $Al_{11}Mn_4$ dissolved and Al_8Mn_5 phase formed, while those particles along the grain boundaries disappeared. It is therefore concluded that the abnormal grain growth was due to the dissolution of second phase particles $Al_{11}Mn_4$, which also obeyed grain growth rate equation (2.14) discussed in chapter 2.7.3:

$$\frac{dR}{dt} = M(P - P_Z) = M\left(\frac{\alpha\gamma}{R} - \frac{3F_V\gamma}{2r}\right)$$

6.2 Superplastic behavior characterization of AZ31

6.2.1 Superplasticity

Two important parameters to measure superplasticity of AZ31 were elongation-to-failure and strain-rate-sensitivity m value, which were obtained from Chapter 5.2.1 and 5.2.2 respectively. The strain rate regions exhibiting high m value were in good agreement with the regions where large elongation values were attained. Peak values for both ductility and m value were achieved under the optimum strain rate value of 4.4×10^{-4} s^{-1}.

Poor ductility was obtained at 200°C due to relatively low temperature. Even though m value was calculated as 0.36 (>0.33) under the optimum strain rate value of 4.4×10^{-4} s^{-1}, the elongation was only 75%, which didn't satisfy the requirement for the

superplastic materials.

The ductility of AZ31 was greatly improved at 300°C and 400°C, this is due to the activation of non-basal slip systems. Superplastic behavior was observed at 300°C under the optimum strain rate of 4.4×10^{-4} s^{-1}, m value of 0.57 and elongation value of 226% was obtained; at 400°C under strain rate of 4.4×10^{-4} s^{-1}, with m value of 0.87 and elongation value of 339%, and 8.8×10^{-4} s^{-1}, also m value of 0.39 and elongation value of 254% was obtained.

6.2.2 Deformation mechanism

Fracture surface after superplastic deformation was specified in chapter 5.2.4. The integrated grains in 'a' area observed on the fracture surface were newly formed DRX fine grains. The intergranular cracking occurred along those newly recrystallized fine grains probably resulted from grain boundary sliding, while the transgranular cracking that resulted in those tearing edges in area 'b', was due to the dislocation creep.

Therefore, it was concluded that grain boundary sliding (GBS) was the dominant deformation mechanism accommodated by dislocation creep after superplastic deformation of AZ31. At 300°C with strain rate of 4.4×10^{-4} s^{-1}, m value measured as 0.57 ($n\approx2$) also consisted with GBS as the dominant deformation mechanism. Similar fracture surface was also observed at 400°C after superplastic deformation.

6.2.3 Dynamic recrystallization mechanism

DRX was observed during deformation as described in chapter 5.2.5. Temperature and strain rate of tensile test do affect the DRX mechanism during deformation. The statistical data showed the opposite tendency of volume fraction of fine grains with the variation of strain rate at 200°C and 300°C, as displayed in figure 6.3. The volume fraction of fine grains near fracture tip decreased as the strain rate increased at 200°C while it increased as the strain rate increased at 300°C. This matched well with the opposite tendency of average grain size with the variation of strain rate at 200°C and 300°C as discussed in Chapter 5.2.5. When the volume fraction of fine grains increased, the average grain size decreased.

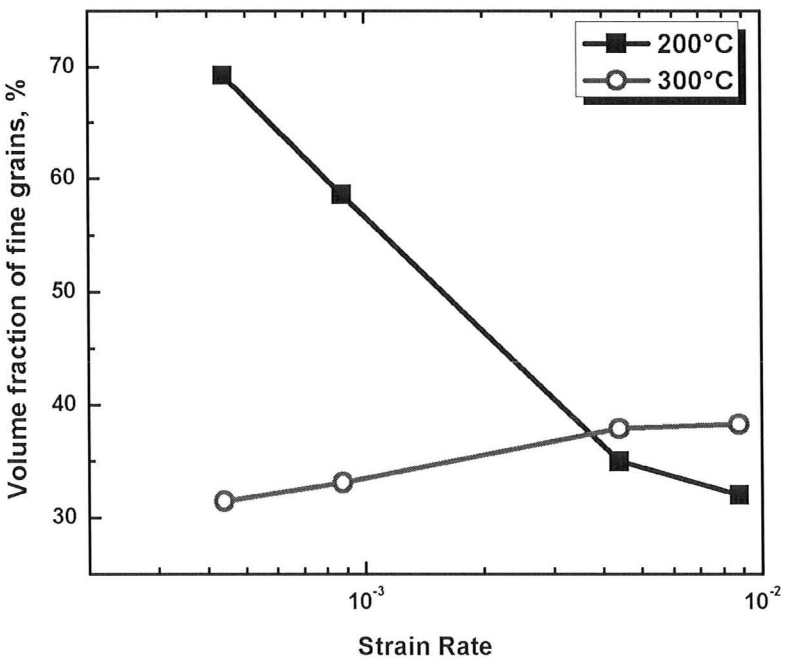

Figure 6.3 Volume fractions of fine grains as a function of strain rate.

This Opposite behavior of volume fraction of fine grains at 200°C and 300°C can be explained by the competition between DRX and dynamic grain growth. At 200°C,

inhomogeneous microstructure resulted from incomplete DRX interrupted before fracture due to relatively low temperature. DRX was the dominant mechanism and was improved as the strain rate decreased. At 300°C, homogeneous microstructure was obtained at relatively lower strain rate of 4.4×10^{-4} s^{-1} as displayed in figure 5.12. However, the lowest volume fraction of fine grains 31% was obtained at this temperature. This can be explained as full completion of DRX followed by grain growth occurred under such low strain rate level. Thus, DRX was not the dominant mechanism at 300°C. Dynamic grain growth was rapidly improved at higher temperature and offset the effect of DRX.

Microstructure evolution after tensile tests at 200°C and 300°C explained the different mechanical responses as described in Chapter 6.2.1. At 200°C, the microstructure was still inhomogeneous and no superplastic behavior was observed. Those large grains are not suitable for GBS because only grains with average grain size of below 10 μm and possessing high misorientation can deform by GBS [18]. However at 300°C, under low strain rate of 4.4×10^{-4} s^{-1}, a homogeneous uniform microstructure was observed which greatly improved the grain boundary sliding mechanism for deformation, thus leading to superplastic behavior.

DRX mechanism also explained different behavior of true stress-strain curve as presented in Chapter 5.2.3. At 200°C, DRX was the dominant mechanism and was improved as strain rate decreased, thus true flow stress increased at higher strain rate while it decreased at lower strain rate. DRX mechanism led to strain softening behavior of true flow stress under lower strain rate. At 300°C, DRX was greatly

improved and true flow stress showed softening behavior under all of the strain rates. A steady state flow was attained after a gradual decrease following the peak stress at higher strain rates. However, the flow stress underwent strain hardening again after strain softening behavior under low strain rate of 4.4×10^{-4} s^{-1}, which revealed that dynamic grain growth was dominant mechanism following the completion of DRX.

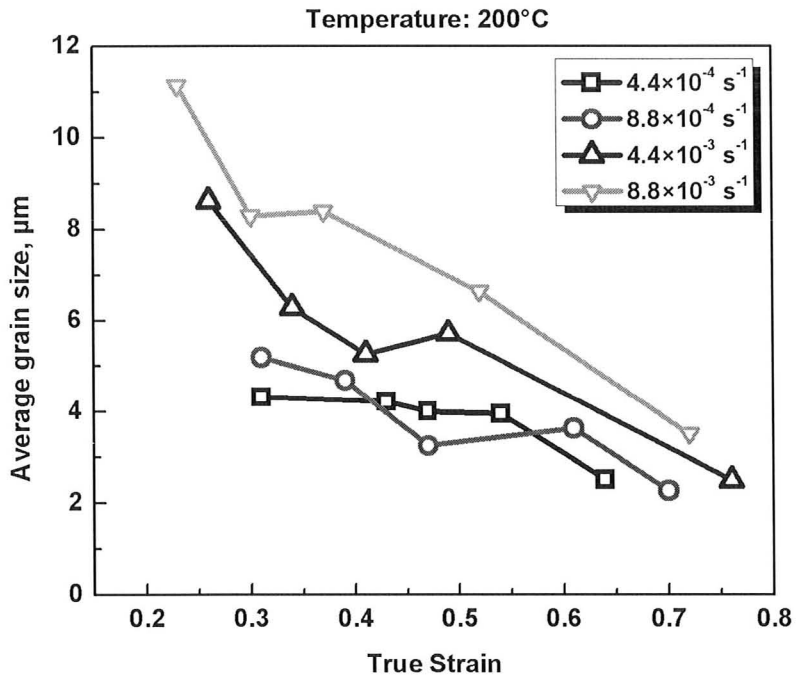

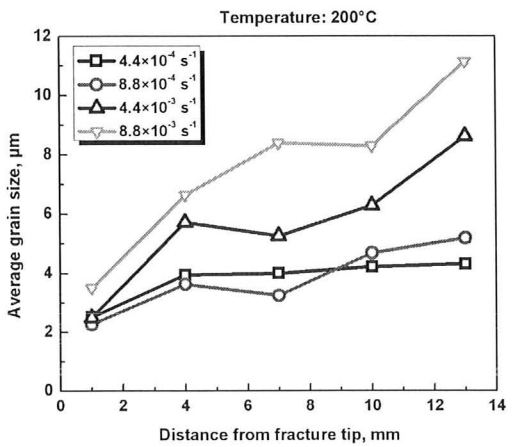

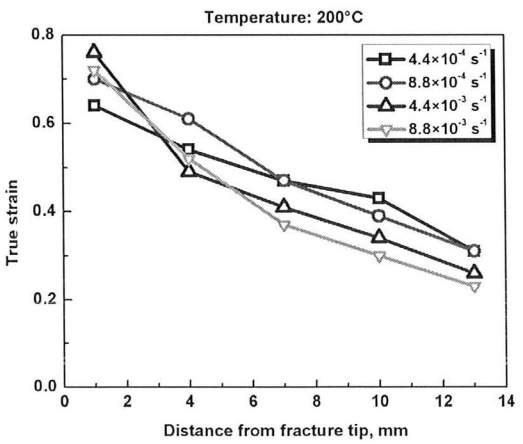

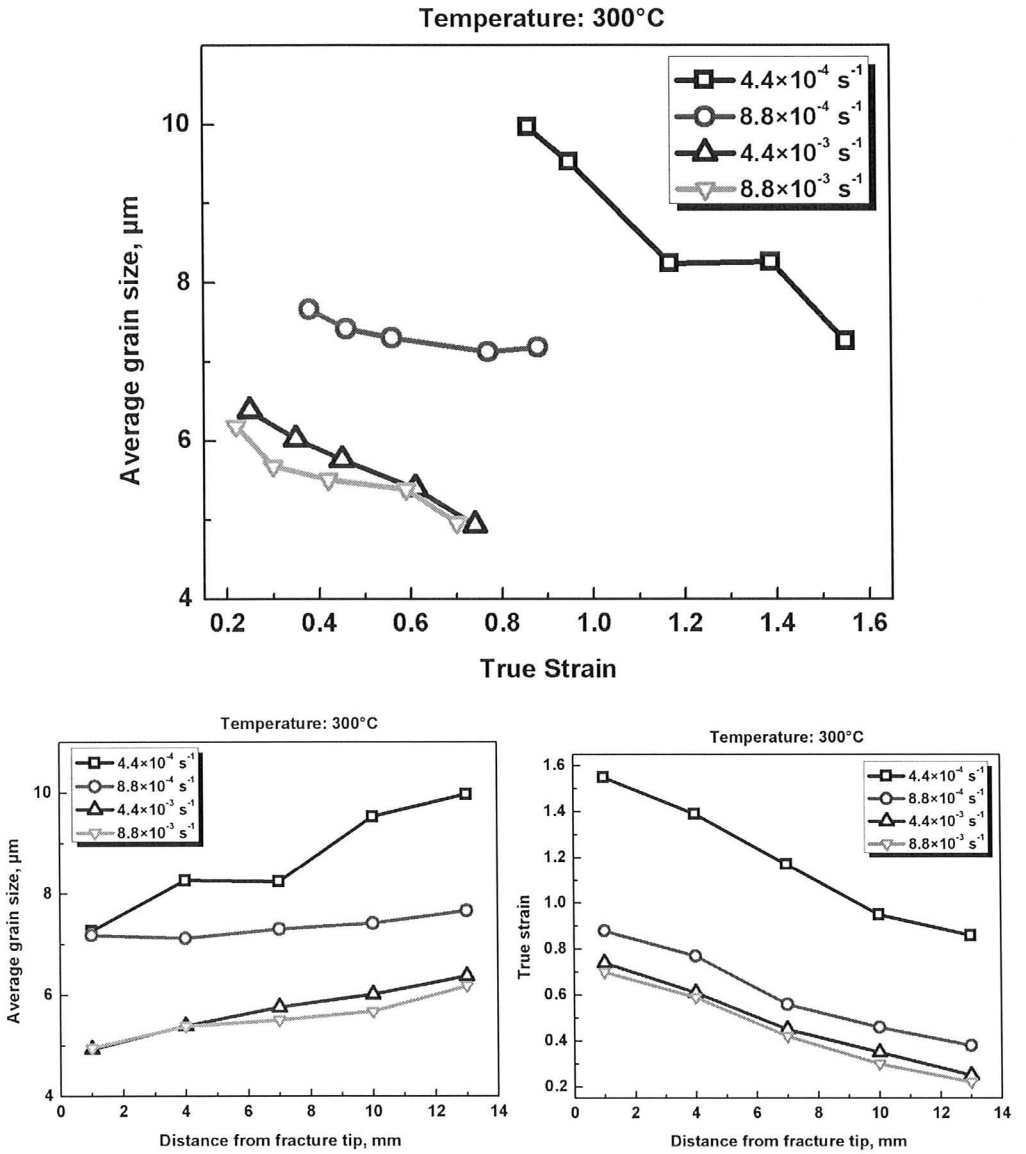

Figure 6.4 Effect of deformation on DRX.

DRX mechanism was also affected by deformation. True strain and average grain size was measured as a function of distance from the fracture tip as shown in figure 6.4. First three images were the plotted after 200°C tensile tests, next three were for 300°C. At both temperatures, when the distance from the fracture tip increased, the average grain size increased while the true strain decreased. The average grain size was inversely proportional to the true strain. Thus, as the deformation increased, the

DRX mechanism was improved. The variation of average grain size and true strain as a function of strain rate also matched well with competition between DRX mechanism and grain growth at both temperatures, thus leading to different mechanical responses. Strain-rate-sensitivity m at 300°C showed greater values than 200°C at lower strain rates ranging from 2.7×10^{-4} s^{-1} to 4.4×10^{-3} s^{-1} as presented in figure 5.7. This explained the average grain size as a function of true strain showed in figure 6.4 was more strain rate sensitive at 300°C than at 200°C especially at lower strain rates.

6.3 Grain refinement by warm rolling of AZ31

6.3.1 Shear Strain measurement in asymmetric rolling

Kang et al [127] has given out a method to evaluate shear strain induced by asymmetric rolling approximately, which can be used in this study. The shear distance S, as the contact arc length between the roll and sheet surface, can be expressed as:

$$S = R\theta = R\cos^{-1}\left(\frac{R-\Delta D/2}{R}\right) \tag{6.1}$$

where R=152 mm is the roll radius, θ is the angle turned by the roll between the shear distance S, $\Delta D=D_2-D_1$ is the change in sheet thickness, here $D_1=1.43$ mm is the initial thickness of AZ31 sheet, $D_2=0.86$ mm is the final thickness of the sheet after rolling.

The angle of shear γ is defined as:

$$\gamma = \frac{1}{<D>}\left[V_R R\cos^{-1}\left(\frac{V_R R-\Delta D/2}{V_R R}\right) - R\cos^{-1}\left(\frac{R-\Delta D/2}{R}\right)\right] \tag{6.2}$$

where $<D>=0.5\times(D_1+D_2)$ is the average sheet thickness, $V_R=1.5$ is the speed ratio

between upper roll and bottom roll. Substitute all the parameters into the equation, the angle of shear γ is calculated as 1.83.

The true strain corresponding to this calculation is:

$$\varepsilon_S = \gamma / 2 = 1.83 / 2 = 0.91 \tag{6.3}$$

Thus, shear strain of 0.91 was induced by asymmetric rolling.

6.3.2 Microstructure evolution

Optical microstructure after different rolling schedules and following heat treatment was displayed in chapter 5.3.1. The average grain size for as-received AZ31 for rolling tests was around 15 μm. Compared with the as-received AZ31, the average grain size of specimens after rolling and annealing was shown in figure 6.5.

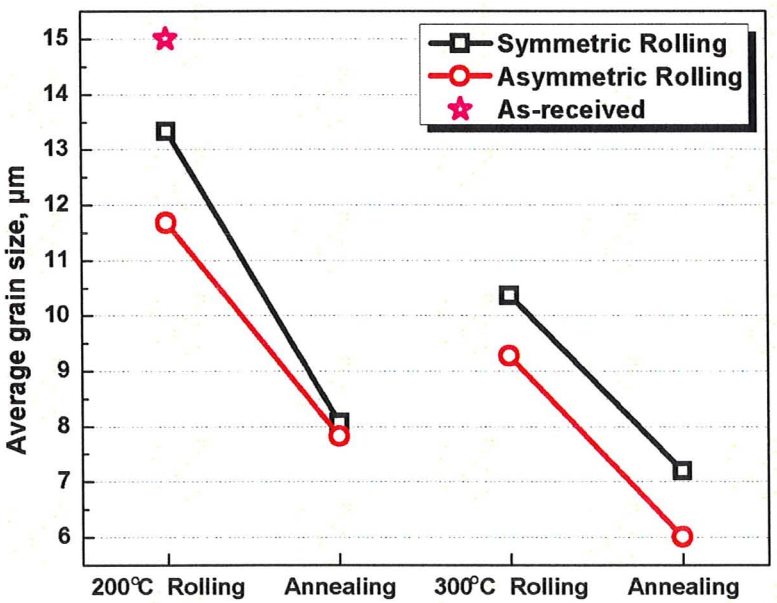

Figure 6.5 Average grain size (unit: μm) after different rolling schedules followed by annealing.

Comparing 200°C rolling and 300°C rolling, the average grain size after 300°C rolling was smaller than 200°C. This can be explained as DRX was greatly improved when rolling temperature increased from 200°C to 300°C. At both rolling temperatures, the average grain size further decreased after the following heat treatment, annealing at 200°C for 1 hour. This is due to the effect of static recrystallization during the heat treatment. Many more newly formed recrystallized fine grains consumed the original deformed microstructure. The microstructure turned out to be quite homogeneous after 300°C rolling followed by 200°C annealing, as shown in figure 5.17. Also comparing between symmetric and asymmetric rolling, the asymmetric rolling was somewhat more effective at grain refinement than symmetric rolling. The average grain size after asymmetric rolling was smaller than symmetric rolling. This can be explained by the shear strain induced in asymmetric rolling as discussed in previous section.

This matched well with texture analysis presented in chapter 5.3.2. Putting together all the intensity values of basal plane (0002) after different rolling schedules and the following annealing procedures, is shown in figure 6.6. The intensity value decreased after annealing for all the rolling procedures. Also when the rolling temperature increased from 200°C to 300°C, the texture became weaker. Intensity value for symmetric rolling was greater than asymmetric rolling. Symmetric rolling had a stronger texture than asymmetric rolling.

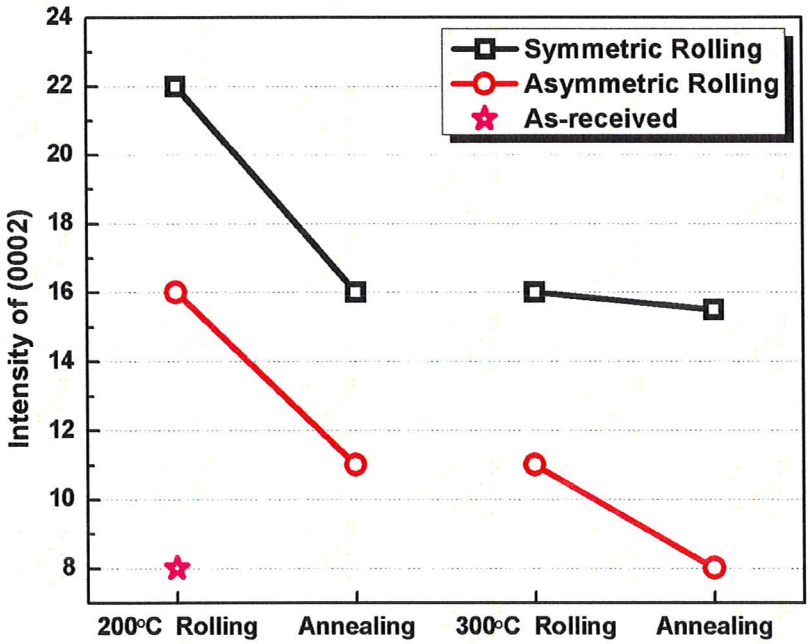

Figure 6.6 Intensity of (0002) after different rolling schedules and the following annealing.

Comparing asymmetric rolling with symmetric rolling, asymmetric rolling was more effective on grain refinement due to the shear deformation introduced by asymmetric rolling as estimated in chapter 6.3.1. Texture was more random after asymmetric rolling than symmetric rolling, while smaller average grain size was also obtained. However, texture did not improve much after rolling plus annealing procedure compared with as-received AZ31.

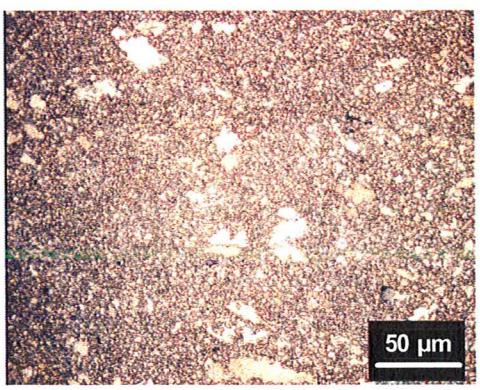

(a) Asymmetric + annealing, 4.4×10^{-4} s^{-1}

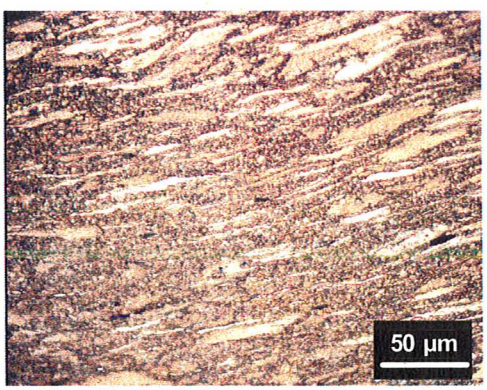

(b) Asymmetric + annealing, 8.8×10^{-3} s^{-1}

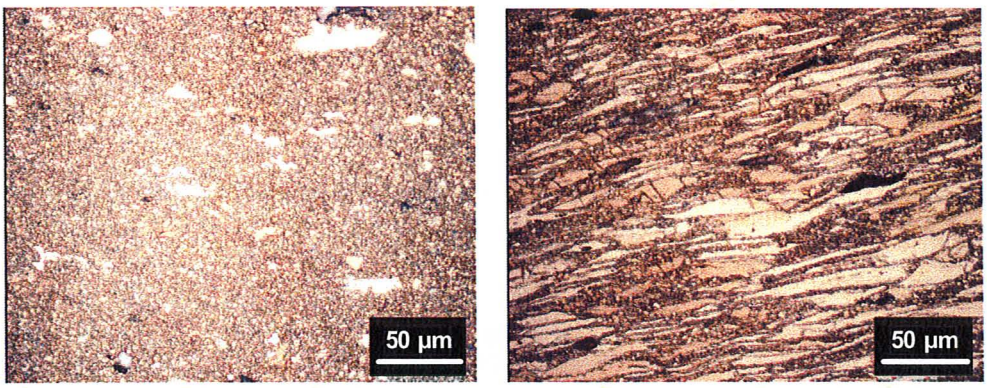

(a) Symmetric + annealing, 4.4×10^{-4} s^{-1} (b) Symmetric + annealing, 8.8×10^{-3} s^{-1}

Figure 6.7 Optical microstructures near fracture tip after tensile tests of AZ31.

Optical microstructure near fracture tip after tensile tests was displayed in figure 6.7. Compared with micrographs from the previous tests of as-received AZ31 under the same condition as presented in chapter 5.2.5, volume fraction of fine grains V_f increased after rolling plus annealing procedures. V_f of 92% and 96% were obtained under low strain rate of 4.4×10^{-4} s^{-1} for (a) symmetric rolling and (b) asymmetric rolling, while V_f of 68% and 62% were obtained under high strain rate of 8.8×10^{-3} s^{-1} for (a) symmetric rolling and (b) asymmetric rolling respectively. However, the microstructure was still inhomogeneous due to the incompletion of DRX. At low strain rate 4.4×10^{-4} s^{-1}, most area was covered with newly formed recrystallized fine grains, DRX showed great effect on microstructure which also explained the decreasing of true flow stress in figure 5.21.

6.3.3 Mechanical properties characterization

As discussed from previous section, asymmetric rolling was more effective on

microstructure modification, more random texture and smaller grain size obtained. Texture played a significant role in mechanical properties.

Asymmetrically rolled specimens, which showed more random texture, gave better ductility than symmetric one after tensile tests. This is due to more basal planes can be activated for slip as the intensity of (0002) decreased for asymmetrically rolled than symmetrically rolled specimens, thus increasing the ductility of AZ31.

Also, the YS and UTS values for asymmetric specimen were smaller than symmetric one. Even though the average grain size for asymmetrically rolled specimens was smaller than symmetrically rolled ones, the strength did not increase with decreasing grain size. This is mainly because the effect of texture. Magnesium alloys can be strengthened by introducing the basal plane (0002) parallel to the tensile direction [128]. Thus, the decreasing intensity of (0002) for asymmetrically rolled specimens would decrease the contribution of strengthening, which offset the effect of decreasing grain size and smaller strength was obtained for asymmetrically rolled specimen.

7. Summary and Conclusions

The following conclusions were obtained through experiment results:

1. Fine grain structure was stable after annealing at 400°C for 1 hour. Once the annealing temperature exceeded 450°C, second phase particles $Al_{11}Mn_4$ dissolved leading to abnormal grain growth.
2. Superplastic behavior of AZ31 was observed in high temperature tensile tests based on fine grain structure, at 300°C with constant strain rate of 4.4×10^{-4} s^{-1}, 400°C with constant strain rate of both 4.4×10^{-4} s^{-1} and 8.8×10^{-4} s^{-1}. Elongation-to-failure exceeded 200% and strain-rate-sensitivity m values was greater than 0.33 in both cases.
3. The dominant deformation mechanism of AZ31 during superplastic deformation was grain boundary sliding accommodated by the dislocation creep.
4. Competition between DRX and grain growth was observed at 200°C and 300°C, which leads to different mechanical responses.
5. Homogeneous microstructure with less than 10 μm average grain size was obtained after 300°C warm rolling followed by 200°C annealing for 1 hour.
6. Asymmetric rolling was more effective than symmetric rolling for grain refinement and more random texture was obtained after asymmetric rolling schedules.
7. Asymmetric rolling specimens had better mechanical properties with greater value of ductility and lower strength.

Bibliography

[1] G. S. Cole, *Materials science forum*, Vol. 419-422, pp. 43-50, 2003.

[2] S. Schumann and H. Friedrich, *Magnesium Alloys 2003, Pts 1 and 2,* vol. 419-4, pp. 51-56, 2003.

[3] T. Kaneko and M. Suzuki, *Materials Science Forum Vols,* vol. 419-422, pp. 67-72, 2003.

[4] M. K. Kulekci,. *International journal of advanced manufacturing technology,* vol. 39(9), pp. 851-865, 2008.

[5] C.S. Roberts, *Magnesium and its Alloys.* United States of American: John Wiley & Sons, Inc, 1960.

[6] E. F. Emley, *Principles of Magnesium Technology.* Oxford: Pergamon Press, 1966.

[7] W. D. Callister, *Materials Science and Engineering : An Introduction.*, 6th Edition, New York, NY: John Wiley & Sons, 2003.

[8] P. G. Partridge and R. W. Gardiner, *Scripta Metallurgica,* vol. 1, pp. 139-142, 1967.

[9] A. Bussiba, A. Ben Artzy, A. Shtechman, S. Ifergan, M. Kupiec, *Materials Science and Engineering A,* vol. 302, pp. 56-62, 2001.

[10] E.Hsu, J.A.Szpunar, R.Verma, *2005 SAE International,* vol. 01, pp. 0258, 2006.

[11] A. Galiyev, R. Kaibyshev, G. Gottstein, *Acta Materialia,* vol. 49, pp. 1199-1207, 2001.

[12] A. Jäger, P. Lukác, V. Gärtnerová, J. Bohlen, K. U. Kainer, *J. Alloys Compounds,* vol. 378, pp. 184-187, 2004.

[13] W. J. Kim, S. W. Chung, C. S. Chung, D. Kum, *Acta Materialia,* vol. 49, pp. 3337-3345. 2001.

[14] T. G. Langdon, *Materials science engineering. A, Structural materials,* 166(1), pp. 71-79, 1993.

[15] M. Marya, L. G. Hector, R. Verma, W. Tong, *Materials Science and Engineering: A,* vol. 418, pp. 341-356, 2006.

[16] T. Mohri, M. Mabuchi, M. Nakamura, T. Asahina, H. Iwasaki, T. Aizawa, K. Higashi, *Materials Science and Engineering A,* vol. 290, pp. 139-144, 2000.

[17] H. Somekawa,. *Materials science engineering. A, Structural materials,* vol. 407(1), pp. 53, 2005.

[18] J. C. Tan and M. J. Tan, *Materials Science and Engineering A,* vol. 339, pp. 124-132, 2003.

[19] J. C. Tan and M. J. Tan, *Materials Science and Engineering A,* vol. 339, pp. 81-89, 2003.

[20] H. Watanabe, T. Mukai, M. Mabuchi and K. Higashi, *Acta Materialia,* vol. 49, pp. 2027-2037, 2001.

[21] H. Watanabe, T. Mukai, M. Kohzu, S. Tanabe, K. Higashi, *Acta Materialia,* vol. 47, pp. 3753-3758, 1999.

[22] H. Watanabe, H. Tsutsui, T. Mukai, M. Kohzu, S. Tanabe, K. Higashi, *Int. J. Plast.,* vol. 17, pp. 387-397, 2001.

[23] Y. H. Wei, Q. D. Wang, Y. P. Zhu, H. T. Zhou, W. J. Ding, Y. Chino, M. Mabuchi, *Materials Science and Engineering A,* vol. 360, pp. 107-115,. 2003.

[24] D. L. Yin, K. F. Zhang, G. F. Wang, W. B. Han, *Mater Let,* vol. 59, pp. 1714-1718, 2005.

[25] B. Bhattacharya, *Plastic deformation behavior of pure magnesium in the temperature range 4.2K-300K,* Ph.D thesis, Mcmaster University, 2006.

[26] K. S. Dunnett, *Microstructural Effects on the Formability of Rolled and Extruded Magnesium Sheet*, M.A.Sc. thesis, Mcmaster University, 2009.

[27] H.Yoshinaga, and R.Horiuchi, *Transactions of the Japan Institute of Metals,* vol. 5, pp. 14-21, 1963.

[28] G. E. Dieter, *Mechanical Metallurgy,* 3rd Ed., 1986.

[29] M. R. Barnett, *Materials Science and Engineering: A,* vol. 464, pp. 1-7, 2007.

[30] M. R. Barnett, *Materials Science and Engineering: A,* vol. 464, pp. 8-16, 2007.

[31] T. Al-Samman and G. Gottstein, *Scr. Mater.,* vol. 59, pp. 760-763, 2008.

[32] E. Schmid and W. Boas, *Plasticity of Crystals with Special Reference to Metals.* London: Chapman & Hall, pp. 353, 1968.

[33] T. G. Nieh, J. Wadsworth, O. D. Sherby, *Superplasticity in Metals and Ceramics.* Cambridge England; New York, NY, USA: Cambridge University Press, 1997.

[34] A.K.Mukherjee, Bird, J.E., & Dorn, J.E., *Transactions of the ASM,* vol. 62, pp. 155-179, 1969.

[35] O. D. Sherby and J. Wadsworth, *Progress in Materials Science,* vol. 33, pp. 169-210, 1989.

[36] T. G. Langdon, *Materials Science and Engineering: A,* vol. 166, pp. 67-70, 1993.

[37] T. G. Langdon, *Acta Metallurgica Et Materialia,* vol. 42, pp. 2437-2443, 1994.

[38] J.Saeki, M.Otsuka, *Proceedings of IMSP,* pp. 69, 1997.

[39] M. Mabuchi, K. Ameyama, H. Iwasaki, K. Higashi, *Acta Materialia,* vol. 47, pp. 2047-2057, 1999.

[40] H. Watanabe, T. Mukai, M. Kohzu, S. Tanabe, K. Higashi, *Acta Materialia,* vol. 47, pp. 3753-3758, 1999.

[41] J. A. del Valle and O. A. Ruano, *Acta Materialia,* vol. 55, pp. 455-466, 2007.

[42] Y. Takigawa, J. V. Aguirre, E. M. Taleff, K. Higashi, *Materials Science and Engineering: A,* vol. 497, pp. 139-146, 2008.

[43] Sean R. Agnew, Özgür Duygulu, *International Journal of Plasticity*, vol. 21, pp. 1161-1193, 2005.

[44] R. Panicker, A. H. Chokshi, R. K. Mishra, R. Verma, P. E. Krajewski, *Acta Materialia,* vol. 57, pp. 3683-3690, 2009.

[45] M. H. Yoo, S. R. Agnew, J. R. Morris, K. M. Ho, *Materials Science and Engineering A*, vol. 319-321, pp. 87-92, 2001.

[46] H. Fukuyo, H.C. Tsai, T.Oyama, O.D.Sherby, *ISIJ International,* vol. 31, pp. 76-85, 1991.

[47] T.G. Langdon, *Metall. Trans.,* vol. 3, pp. 797, 1972.

[48] R.L. Bell, C. Graeme-Barber, T.G. Langdon, *Trans. AIME,* vol. 239, pp. 1821, 1967.

[49] O. A. K. R.Z. Valiev, *Acta Metall.,* vol. 31, pp. 2121, 1983.

[50] K. Matsuki, N. Hariyama, M. Tokizawa, Y. Murakami, *Met. Sci.,* vol. 17, pp. 503, 1983.

[51] T.G. Langdon, *J. Mater. Sci.,* vol. 16, pp. 2613, 1981.

[52] R. C. Gifkins, *Mater. Forum,* vol. 15, pp. 82, 1991.

[53] P. M. B. O.D. Sherby, *Progress in Materials Science,* vol. 13, pp. 325-390, 1967.

[54] J. Weertman, *J. Appl. Phys.,* vol. 28, pp. 1185-1191, 1957.

[55] J. Weertman, *Transactions of the ASM,* vol. 61, pp. 681-694, 1968.

[56] F.R.N. Nabarro, *Philosophical Magazine. A, Physics of Condensed Matter, Defects and Mechanical Properties,* vol. 16, pp. 231-237, 1967.

[57] O. D. Sherby and J. Wadsworth, *Progress in Materials Science,* vol. 33, pp. 211-221, 1989.

[58] S. S. Vagarali and T. G. Langdon, *Acta Metallurgica,* vol. 29, pp. 1969-1982, 1981.

[59] S. S. Vagarali and T. G. Langdon, *Acta Metallurgica,* vol. 30, pp. 1157-1170, 1982.

[60] M. H. F.J. Humphreys, *Recrystallization and related annealing phenomena*, Second Edition, Elsevier, 2004.

[61] M. M. Myshlyaev, H. J. McQueen, A. Mwembela, E. Konopleva, *Materials Science and Engineering A,* vol. 337, pp. 121-133, 2002.

[62] J. Koike, T. Kobayashi, T. Mukai, H. Watanabe, M. Suzuki, K. Maruyama and K. Higashi, *Acta Materialia,* vol. 51, pp. 2055-2065, 2003.

[63] S. M. Fatemi-Varzaneh, A. Zarei-Hanzaki, H. Beladi, *Materials Science and Engineering: A,* vol. 456, pp. 52-57, 2007.

[64] T. Al-Samman and G. Gottstein, *Materials Science and Engineering: A,* vol. 490,

pp. 411-420, 2008.

[65] J. A. del Valle and O. A. Ruano, *Mater Lett,* vol. 62, pp. 3391-3394, 2008.

[66] R. Panicker, A. H. Chokshi, R. K. Mishra, R. Verma, P. E. Krajewski, *Acta Materialia,* vol. 57, pp. 3691-3693, 2009.

[67] X. Yang, Z. Ji, H. Miura, T. Sakai, *Transactions of Nonferrous Metals Society of China,* vol. 19, pp. 55-60, 2009.

[68] O. A. Kaibyshev, *J. Mater. Process. Technol.,* vol. 117, pp. 300-306, 2001.

[69] A. Staroselsky, L. Anand, *International Journal of Plasticity*, vol. 19, pp 1843-1864, 2003.

[70] S. M. Fatemi-Varzaneh, A. Zarei-Hanzaki, H. Beladi, *Materials Science and Engineering: A,* vol. 456, pp. 52-57, 2007.

[71] J.E. Burker, D. Turnbull, *Prog. Metal Phys.,* vol. 3, pp. 220, 1952.

[72] S. C.Zener, *Trans.Am.Inst.Min.Engrs,* vol. 175, pp. 47, 1948.

[73] M.Hillert, *Acta Metallurgica,* vol. 13, pp. 227-238, 1965.

[74] T. Gladman, *Proc. Roy. Soc. London,* vol. 294A, pp. 298-309, 1966.

[75] N. A. Haroun and D. W. Budworth, *Journal of Materials Science,* vol. 3, pp. 326-328, 1968.

[76] Per Hellman and Mats Hillert, *Scandinavian Journal of Metallurgy,* vol. 4, pp. 211-219, 1975.

[77] T. Gladman, *Risø International Symposium on Metallurgy and Materials,* pp. 183-191, 1980.

[78] N. Louat,. *Acta metallurgica,* vol. 30(7), pp. 1291, 1982.

[79] N. Louat,. *Philosophical magazine. A, Physics of condensed matter, defects and mechanical properties,* vol. 47(6), pp. 903, 1983.

[80] C. J. Tweed,. *Metallurgical transactions. A, Physical metallurgy and materials science,* vol. 14(11), pp. 2235, 1983.

[81] M. Hillert,. *Scripta metallurgica,* vol. 18(12), pp. 1431, 1984.

[82] C. J. Tweed., *Acta metallurgica,* vol. 32(9), pp. 1407, 1984.

[83] C. H. Woerner,. *Scripta metallurgica,* vol. 18(6), pp. 565, 1984.

[84] C. H. Worner, *Scripta metallurgica,* vol. 20(6), pp. 829, 1986.

[85] P. R. Rios, *Acta Metallurgica,* vol. 35, pp. 2805-2814, 1987.

[86] C. H. Worner, *Acta metallurgica,* vol. 35(11), pp. 2801, 1987.

[87] P. M. Hazzledine, *Czechoslovak Journal of Physics,* vol. 38(4), pp. 431, 1988.

[88] A. Yamamoto, *Materials science forum,* vol. 449(1), pp. 669, 2004.

[89] M. Fujita, N. Sakate, S. Hirahara, Y. Yamamoto, *JSAE Rev.,* vol. 16, pp. 299-301, 1995.

[90] J. E.Gruzleski, A. Aliravci, US Patent US005143564A, 1992.

[91] Q. Wang, W. Chen, X. Zeng, Y. Lu, W. Ding, Y. Zhu, X. Xu, *Journal of Materials Science,* vol. 36, pp. 3035-3040, 2001.

[92] Z. Zhang, R. Tremblay, D. Dube, *Mater. Sci. Tech.,* vol. 18, pp. 433, 2002.

[93] M.O. Pekguleryuz, E. Baril, *Metallurgical Transactions,* vol. 42, pp. 1258, 2001.

[94] A. Luo, M.P. Balogh, B.F. Powell, *Metall. Trans.,* vol. 33, pp. 567, 2002.

[95] T. Chang, J. Wang, C. O, S. Lee, *J. Mater. Process. Technol.,* vol. 140, pp. 588-591, 2003.

[96] P. Cao, M. Qian, D. H. StJohn, *Scr. Mater.*, vol. 56, pp. 633-636, 2007.

[97] S. X. Ding, W. T. Lee, C. P. Chang, L. W. Chang, P. W. Kao, *Scr. Mater.*, vol. 59, pp. 1006-1009, 2008.

[98] R. B. Figueiredo and T. G. Langdon, *Materials Science and Engineering: A,* vol. 501, pp. 105-114, 2009.

[99] J. Jiang, Y. Wang, S. Luo, *Mater Charact,* vol. 58, pp. 190-196, 2007.

[100] S. H. Kang, Y. S. Lee, J. H. Lee, *J. Mater. Process. Technol.*, vol. 201, pp. 436-440, 2008.

[101] M. Mabuchi, H. Iwasaki, K. Yanase, K. Higashi, *Scr. Mater.*, vol. 36, pp. 681-686, 1997.

[102] H. Somekawa and T. Mukai, *Scr. Mater.*, vol. 53, pp. 1059-1064, 2005.

[103] S. Suwas, G. Gottstein, R. Kumar, *Materials Science and Engineering: A,* vol. 471, pp. 1-14, 2007.

[104] Y. Uematsu, K. Tokaji, M. Kamakura, K. Uchida, H. Shibata, N. Bekku, *Materials Science and Engineering: A,* vol. 434, pp. 131-140, 2006.

[105] R. Roumina, C.W. Sinclair, *Metallurgical and Materials Transactions A,* vol. 36A, pp. 2495-2503, 2008.

[106] X. Huang, K. Suzuki, N. Saito, *Materials Science and Engineering: A,* vol. 508, pp. 226-233, 2009.

[107] W. J. Kim,. *Materials science engineering. A, Structural materials,* vol. 454, pp. 570, 2007.

[108] H. Xinsheng,. *Journal of materials research*, 23(11), pp. 3029, 2008.

[109] S. Kim, B. You, C. Dong Yim, Y. Seo, *Mater Lett,* vol. 59, pp. 3876-3880, 2005.

[110] W. J. Kim, J. B. Lee, W. Y. Kim, H. T. Jeong, H. G. Jeong, *Scr. Mater.,* vol. 56, pp. 309-312, 2007.

[111] W. J. Kim, J. D. Park, W. Y. Kim, *J. Alloys Compounds,* vol. 460, pp. 289-293, 2008.

[112] N. Stanford and M. R. Barnett, *J. Alloys Compounds,* vol. 466, pp. 182-188, 2008.

[113] G. Vespa, L. W. F. Mackenzie, R. Verma, F. Zarandi, E. Essadiqi, S. Yue, *Materials Science and Engineering: A,* vol. 487, pp. 243-250, 2008.

[114] H. Watanabe, T. Mukai, K. Ishikawa, *Journal of materials science*, vol. 39(4), pp. 1477-1480, 2004.

[115] ASM handbook, *Heat treating*, vol. 4, Anonymous United States of America: ASM International Handbook committee, pp. 899-906, 1991.

[116] Annual Book of ASTM Standards, Section 3: 03.01, *E2448-08*, Anonymous Philadelphia, PA: American Society of Testing and Materials, pp. 1404-1410, 2007.

[117] J. Kang, Y. Ososkov, J. D. Embury, D. S. Wilkinson, *Scr. Mater.,* vol. 56, pp. 999-1002, 2007.

[118] J.W. Tong, *Mech. Phys. Solids,* vol. 46, pp. 2087-2102, 1998.

[119] J. Kang, D. S. Wilkinson, J. D. Embury, M. Jain, A. J. Beaudoin, *Scr. Mater.,* vol. 53, pp. 499-503, 2005.

[120] J. Kang, D. S. Wilkinson, M. Jain, J. D. Embury, A. J. Beaudoin, S. Kim, R.

Mishira, A. K. Sachdev, *Acta Materialia,* vol. 54, pp. 209-218, 2006.

[121] Aramis, *Deformation measurement using the grating method*, Users manual, Anonymous Germany: GOM mbH, Braunschweig, 2001,

[122] Z. Marciniak, J.L. Duncan, S.J. Hu, *Mechanics of Sheet Metal Forming.* Linacre House, Hordan Hill, Oxford OX2 8DP: Butterworth-Heinemann, 2002.

[123] General Area Detector Diffraction System (GADDS), version 4.0, Users manual, *Burker Advanced X-Ray Solutions.* U.S.A.: Burker AXS Inc., Madison, Wisconsin, 1999.

[124] Diffrac Multex Area, Version 2, Users Manual, *Burker Advanced X-Ray Solutions.* Germany: Burker AXS Inc., Madison, Wisconsin, 2006,

[125] Annual Book of ASTM Standards, Section 3: 03.01, *E112-96*, Anonymous Philadelphia, PA: American Society of Testing and Materials, pp. 313-338, 2007.

[126] Clemex intelligent microscopy, *User Guide, Version 5.0*, 800 Guimond, Longueuil (Quebec), Canada: Clemex Technologies, Inc., 2007.

[127] S. Kang, B. Min, H. Kim, D. S. Wilkinson, J. Kang, *Metallurgical and Materials Transactions A*, vol. 36A, pp. 3141-3149, 2005.

[128] H. Watanabe, T. Mukai, K. Ishikawa, *Journal of Materials Processing Technology*, vol. 182, pp. 644-647, 2007.